UNIVERZA V LJUBLJANI
NARAVOSLOVNOTEHNIŠKA FAKULTETA

DOKTORSKA DISERTACIJA

MATJAŽ BERČIČ

LJUBLJANA 2019

UNIVERZA V LJUBLJANI
NARAVOSLOVNOTEHNIŠKA FAKULTETA
ODDELEK ZA MATERIALE IN METALURGIJO

ENOTNA OBRAVNAVA PREHODA MED SKALAMI PRI SIMULACIJAH RAZVOJA MIKROSTRUKTURE Z METODO FAZNEGA POLJA KRISTALA

DOKTORSKA DISERTACIJA

MATJAŽ BERČIČ

LJUBLJANA, april 2019

UNIVERSITY OF LJUBLJANA
FACULTY OF NATURAL SCIENCES AND ENGINEERING
DEPARTMENT OF MATERIALS AND METALLURGY

UNIFIED APPROACH TO SCALE TRANSITION IN SIMULATIONS OF MICROSTRUCTURE EVOLUTION USING PHASE-FIELD CRYSTAL MODEL

Ph. D. THESIS

MATJAŽ BERČIČ

LJUBLJANA, April 2019

PODATKI O DISERTACIJI

Število listov: 84

Število strani: 144

Število slik: 62

Število preglednic: 1

Število literaturnih virov: 71

Število prilog: 0

Študijski program: doktorski študijski program 3. stopnje
Znanost in inženirstvo materialov
Smer: materiali

Komisija za zagovor

Predsednik:

Mentor: prof. dr. Goran Kugler

Član: prof. dr. Tomaž Rodič

Član: prof. dr. Ing. Heinz Palkowski

IZVLEČEK V SLOVENSKEM JEZIKU

Model faznega polja kristala (PFC) lahko opiše material z atomistično resolucijo preko difizuijskih časov s pomočjo polja atomske gostote. Razširitev modela z razvojem po amplitudah (APFC) spremeni model v obliko, primerno za uporabo s tehnikami adaptivnega zgoščevanja računske mreže (AMR). Teza predstavi izboljšave v modelu APFC, ki omogočijo učinkovito uporabo tehnik adaptivnega zgoščevanja mreže računskih točk. Vpeljano je pomožno polje, ki opisuje lokalno rotacijo zrna in omogoči redčenje mreže računskih točk v vseh zrnih, ne glede na njihovo orientacijo. Uporabljena je le kartezična oblika amplitudnih enačb. Vpeljan algoritem izračuna polje lokalne rotacije in izkoristi rotacijsko kovariantnost dinamičnih enačb za evolucijo amplitudnih enačb, da doseže učinkovito uporabo računalniške moči. Pomožno polje je uporabljeno, da v modelu APFC odstrani nefizikalno mejo med zrni, ki so rotirana za simetrijsko rotacijo kristala. Nefizikalna meja je odstranjena s pomočjo pravilnega ujemanja kompleksnih amplitud, ki opisujejo najbolj ujemajoče se gostotne valove. Izboljšava popravi energije mej med polovico naključno rotiranimi zrni in omogoči APFC simulacije procesov, v katerih zrna rotirajo. Simulacije zrna, ki rotira v matriki, narejene z modeloma PFC in APFC, dajo kvalitativno ujemajoče se rezultate, kar potrjuje odstranitev nefizikalne meje med zrni tudi v pogojih, pri katerih zrna dinamično rotirajo. Skupaj izboljšave omogočijo simulacije mikrostrukture z atomistično resolucijo modela APFC na adaptivni mreži računskih točk, ki učinkovito razporeja računalniško moč tudi v simulacijah procesov, kjer zrna rotirajo.

Ključne besede: fazno polje kristala, amplitudni razvoj, rast zrn, modeliranje mikrostrukture

ABSTRACT

The Phase-Field Crystal model (PFC) is a model that is able to describe material on the atomic level across diffusive time scales using a continuous atomic density field. Its amplitude expansion (APFC) reformulates the model in a form suitable for the application of adaptive mesh refinement techniques. This thesis presents improvements to the APFC model that lead to effective use of adaptive mesh refinement techniques. An auxiliary field describing local grain rotation is introduced and used to enable the adaptive mesh to coarsen in all grains, regardless of their orientation. Only a Cartesian representation of the amplitude equations is employed. The introduced algorithm extracts the local grain rotation and exploits the rotational covariance of the amplitude equations to achieve efficient use of computational resources. The auxiliary local rotation field is used to remove an unphysical grain boundary present in the APFC model between grains, which are rotated by the crystal's symmetry rotation. The unphysical grain boundary is removed by correctly matching the complex amplitudes describing the best aligned density waves. This corrects the grain boundary energies in half of the grain boundaries formed between the randomly rotated grains and enables APFC simulations of processes where grain rotation occurs. Simulations of a single rotating grain using the PFC and APFC models show qualitatively matching results, confirming the effective removal of the unphysical grain boundary under conditions where grains rotate dynamically. Together, the improvements enable microstructure simulations with the APFC model on an adaptive computational mesh, which efficiently distributes computational resources even in simulations of processes where grains rotate.

Key words: phase-field crystal, amplitude expansion, grain growth, microstructure modelling

IZJAVA

Podpisani Matjaž Berčič, izjavljam, da je doktorska disertacija z naslovom “Enotna obravnava prehoda med skalami pri simulacijah razvoja mikrostrukture z metodo faznega polja kristala” rezultat mojega raziskovalnega dela.

Acknowledgements

I wish to express my thanks and gratitude to my supervisor and teacher, Prof. Dr. Goran Kugler, whose guidance in this project was invaluable. He offered me his knowledge, advice, help and support throughout the project. This was coupled with his generous patience, and without him this project would have been impossible.

My sincere thanks go to my colleagues Dr. Peter Fajfar, Dr. David Bombač, Dr. Alenka Šalej, Andrej Penko and Matevž Pintar who sparked my curiosity in what was initially a new field of work for me, and helped me understand the relevant phenomena.

Because this work is built on knowledge my past teachers helped me acquire, I wish to thank Marko Špolad, Dr. Tine Porenta and Prof. Dr. Miha Ravnik for their guidance and support.

Finally, I wish to express my gratitude to my family, my parents Simona and Gorazd, my sister Kristina and my grandparents for their support and love.

I acknowledge financial support received from the Slovenian Research Agency (ARRS).

Contents

List of figures

List of tables

Nomenclature, Acronyms and Abbreviations

Acronyms and Abbreviations

AMR	Adaptive Mesh Refinement
APFC	Amplitude Expansion of the Phase-Field Crystal model
ICME	Integrated Computational Materials Engineering
PDE	Partial Differential Equation
PF	Phase Field Method / Models
PFC	Phase-Field Crystal model
XPFC	Structural PFC model

Symbols

ψ	Atomic density function	[Dimensionless units]
ρ	Atomic density function	[Number of atoms per volume]
A_j	Complex amplitudes in APFC model	
CC	Complex conjugate of the preceding expression, frequently used in APFC models	
k_B	Boltzmann's constant	$[8.617 \times 10^{-}5eV/K]$

Chapter 1

Introduction

1.1 Definition of the research problem

Modern material science is based on the discovery that a material's properties are largely influenced by its microstructure, and do not only depend on its chemical composition. The influence of the microstructure is especially evident in the mechanical properties of the material because some aspects of it (i.e. average grain size) directly correlate with many of the material's properties. Microstructure can be described on multiple different scales [1, 2]. On the lowest level the quantum mechanical phenomena are most important. Moving up scales on the atomic level the microstructure is described by atomic positions, lattices of the crystals, and defects in such lattices. Mezoscopic scale describes the material on the level of the grains and defines how different phases are distributed in the material. On the macroscopic scale all micro phenomena are averaged out and the material is described as a continuum with specific physical properties (atomic density and lattice parameters) that change continuously with noticeable changes only over larger lengths. The interconnection between different scales at which we can study or understand the material becomes apparent when we wish to answer a common question, such as "why did a certain mechanical part break (i.e. shaft of a petrol engine)?". While the failure mechanical part's failure is observable on the macroscopic scale, the origin of the cracks leading to it is on the atomic scale. Therefore, to truly understand many phenomena we must be able to connect conclusions on different scales or even better, unify our understanding of the phenomena across different length scales. As well as length scales, the time scales of different phenomena relevant for understanding the processes that determine the final physical properties of a material vary greatly. Time scales of vibrations of the atomic lattice are connected with the speed at which certain phase transformations spread in the material and the speed at which mechanical deformations spread through the material. Experiments that would give us insights into the microstructure's evolution are sometimes difficult to conduct, expensive or even impossible. It is hard to imagine successfully tracking the atomic positions in the middle of a sample of an observable size experimentally, during a process where the sample is deformed and heat treated to emulate an industrial production process. As the interactions of different processes influencing the microstructure's evolution are complex, computer models with high predictive power that can emulate industrial processes are ever more important in the design of modern materials. While useful, the computer simulations have their limits mainly based on the computational power obtainable today with reasonable resources. The "ab initio" methods that are not based on experimentally obtained data and can be used to track quantum mechanical phenomena are currently limited to very small spatial scales due to the computational power they need. The difficulties of modelling the materials across a large span of temporal and spatial scales can be partially overcome by using an ensemble of models instead of one model alone. Such an approach is called Integrated Computational Materials Engineering (ICME) [3] and the key to its success lies in using the most appropriate model on each of the scales in sequence, and then connecting the models together by exchanging some parameters between the models. While highly valuable, this approach can also lead to observations of unphysical phenomena in the models due to the discontinuous transition between models at different scales. The success of the phase-field method (PF) [4] in modelling phenomena that occur on largely different time and length scales indicates that a model able to describe the material on many time and length scales in a unified way is highly desirable. Combined with adaptive mesh refinement techniques, the PF method can model the dendritic growth in samples of macroscopic sizes. The applicability of AMR techniques allows the PF method to span many spatial scales. As the PF method operates with a so-called phase field variable (order parameter) that is a continuous function of space, it does not reach the space scales at which the arrangement of atoms is described at the lower end of scales it can describe, because the atomic arrangements are averaged out in and only the information about the material's phase is preserved in the model. This makes it unsuitable for modelling phenomena operating on the level of atomic arrangements, such as interactions between grains, growth and transformation of grains during thermo-mechanical processing and phase transformations due to micro conditions at the grain boundaries.

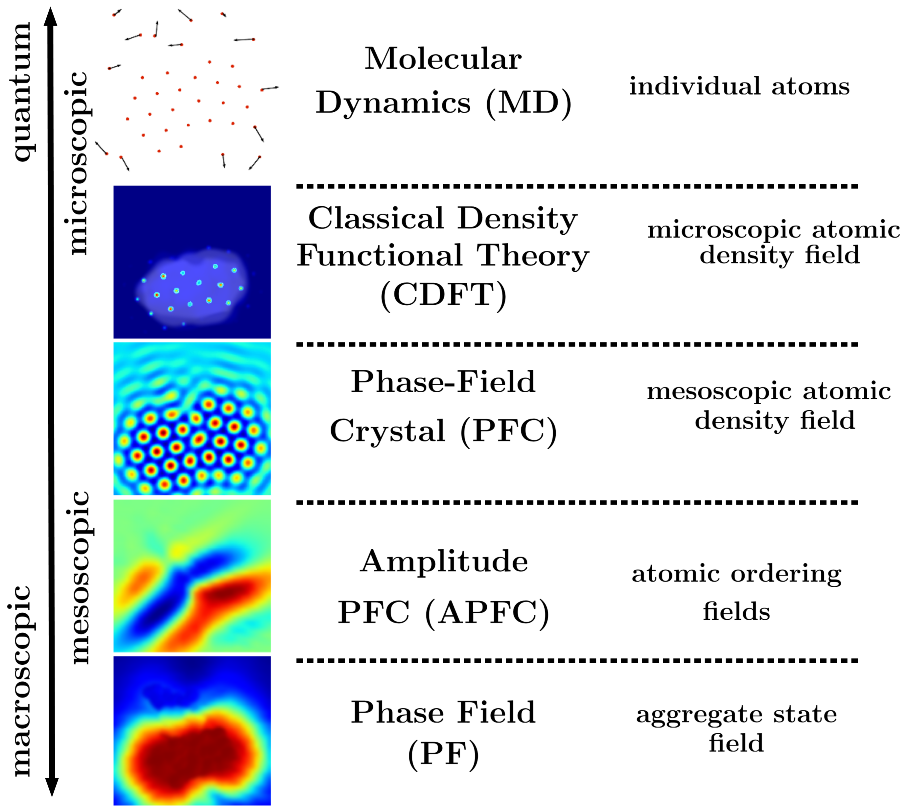

Figure 1.1: Methods used in material modelling at different scales. The PFC and APFC methods bridge the scales between the *ab initio* methods on the smallest scales and phenomenologically derived methods on the mesoscopic scales.

The method's ability to describe many length scales in a unified way is considerably more important in the field of metallurgy. New materials are designed by manipulating processes occurring on atomistic scales while the produced metallic ingots are measured in tons. While the industrial processes manipulate the material in large samples, the transformation they produce in the material itself can only be understood on the atomistic level. A method able to preserve the atomistic resolution on length scales approaching measurable samples would therefore be ideally suited for modelling metallurgically important phenomena. Figure 1.1 illustrates the modelling methods most frequently used at different scales together with a description of the material associated with each method.

The phase field crystal method (PFC) is similar in nature to the PF method by describing the material through field rather than modelling it using an ensemble of atoms or molecules. Yet, unlike the PF method, the field in the PFC method describes the local atomic density, thus rendering the method suitable for modelling phenomena, where atomic arrangements are vital for understanding [5, 6]. Describing the material using a field gives the PFC method the ability to span larger volume and time scales than other methods that can describe the material on atomic level, such as the molecular dynamics methods and classical density functional theory based models. These properties make the PFC model the ideal model for describing the evolution of the material's microstructure across the time and volume scales needed to model interesting phenomena based on the interaction between grain boundaries. As the atomic density function on which the PFC model operates rapidly varies in space with peaks around the expected atomic positions, it can not be used in combination with AMR techniques. In order to enable the AMR techniques to be used together with the PFC model, the so-called Amplitude Expansion of the PFC model was developed (APFC) by Goldenfeld *et al.* [7, 8]. The extension is based on renormalization group theory and expresses the atomic density function in terms of complex amplitudes which represent the amplitudes of density waves, aligned with the corresponding base vectors. The introduced complex amplitudes vary much slower in space, bringing the benefit of requiring a coarser computational mesh. The amplitudes also do not resolve the quick variations in atomic density, and are therefore more suitable for use with AMR techniques. While expressing the atomic density function with a set of complex amplitudes, the grain's rotation is expressed through the so-called beats in the complex amplitudes, preventing efficient use of AMR techniques in rotated grains. Athreya *et al.* [9] developed a novel approach to express the complex amplitudes in terms of phase and amplitude, which are more suitable for AMR techniques, and achieved mesh refinement in all grains. As the process included converting the complex amplitude equations into separate equations for phase and amplitude and splitting the simulation domain into two regions, one where the phase and amplitude equations were evolved and the other where normal complex amplitude equations were evolved, this approach was not widely used, and most APFC models today still use a fixed grid. Conversion of the PFC model into the APFC formulation also introduces a new error in the simulation, whereby an unphysical grain boundary occurs between grains, rotated by a crystal's symmetry rotation as reported by Spatschek and Karma [10]. This problem is not easy to solve and limits use of APFC models to cases where grain rotation does not occur and the set of grain rotations can be feasibly limited to rotations below half the crystal's symmetry rotation. As grain rotation frequently occurs during industrial processing of material (i.e. rolling, forging), this prevents any wider applicability of the APFC models for studying the microstructure's transformation during industrial processing.

1.2 Scope, aim and outline of the thesis

Models able to study the evolution of microstructure on an atomic level on diffusive timescales are rare. In this thesis, the APFC model was improved to enable mesh refinement in a Cartesian representation of the complex amplitudes using an auxiliary local rotation field variable. The idea of using an auxiliary field, that is not directly used in the calculation in this context, constitutes a new contribution of this thesis. The auxiliary local rotation field is derived from the complex amplitudes and, in step one, used to enable the mesh refinement in the APFC model in all grains regardless of their orientation using only the Cartesian representation of the complex amplitudes. The algorithm we developed exploits the rotational covariance in the APFC equations in a novel way to achieve this. In the second step, we eliminated the unphysical grain boundary from the APFC model using the information we gained from the local rotation field to correctly connect the complex amplitudes in the neighboring computational nodes. The additional improvement in the algorithm needed to achieve this includes a lookup table and an amplitude-matching algorithm. In the last step, we verified that the new algorithm can be applied to model processes where grain rotation occurs by modelling a simple example where a single circular grain is forced to rotate within a solidified matrix. We compared the results with those obtained using the basic PFC model and found good agreement in the observed phenomena.

The contributions of this thesis enable processes to be simulated where grain rotation occurs on adaptive meshes. This increases the applicability of APFC models to modelling industrially important processes in a way that facilitates the study of phenomena that are fundamentally atomistic in nature (e.g. interaction between defects in crystal lattices, interaction between grain boundaries).

The thesis is organized as follows. A theoretical description of the PFC, APFC and related models is given in Chapters 2 and 3. Numerical methods frequently used with the PFC and APFC models are described in Chapter 4. The next chapters focusing on the contribution made by the thesis can be read as complete, standalone works. Each thesis contribution in Chapters 5, 6 and 7 includes a short introduction, and an overview of the theory and methods. To be able to compare our results with existing works, we used slightly different models in these sections, as the works with which we compared our models also used slightly different PFC/APFC models. These models are described in detail in the theoretical parts of these chapters, which cover the topics of the thesis. Our approach to enabling adaptive mesh refinement in APFC models using only the Cartesian representation of the complex amplitudes is described in Chapter 5. The way to remove the effects of the unphysical grain boundary from the APFC model is described in Chapter 6, and our final application of the model to an example process where grain rotation is present is described in Chapter 7. Chapter 8 summarizes the contribution brought by the thesis, discusses the limitations of our approach, and directions for future research. The last part of the thesis consists of an extended summary in the Slovenian language.

Chapter 2

Phase-Field Crystal Model

2.1 Introduction

Phase-field crystal model (PFC) is a pattern formation model that can be used for modelling crystalline materials over diffusive timescales [5, 6]. It is based on minimization of a free energy functional which is constructed in such way that the solution to the problem is a periodic function of space. As such, it naturally incorporates many features of crystalline systems, such as elasticity in crystalline phase, formation of topological defects, energy of grain boundaries, grain growth, solid-liquid phase transformation and solid state phase transformations. Figure 2.1 presents examples of PFC model simulations.

The PFC model can be placed between classical density functional theory based models (CDFT) on one side and phase-field (PF) models on the other side, and has been connected to the CDFT under some necessary assumptions [11]. Like CDFT models it operates on an atomic density function, but in contrast to the CDFT approach, the atomic density function is smoothed and the sharp peaks in density that represent the locations of the atoms in CDFT models are spread over larger area. This allows for a coarser computational mesh, and allows the models to reach larger volumes and diffusive times. At the cost of some loss of accuracy in the description of the material, the PFC model can reach diffusive times in samples large enough to enable the study of interactions of defects in crystal latices and grain boundaries. The connection to the PF models comes through expanding the atomic density function in terms of plane waves aligned with the set of basis vectors, weighted by the respective complex amplitudes in

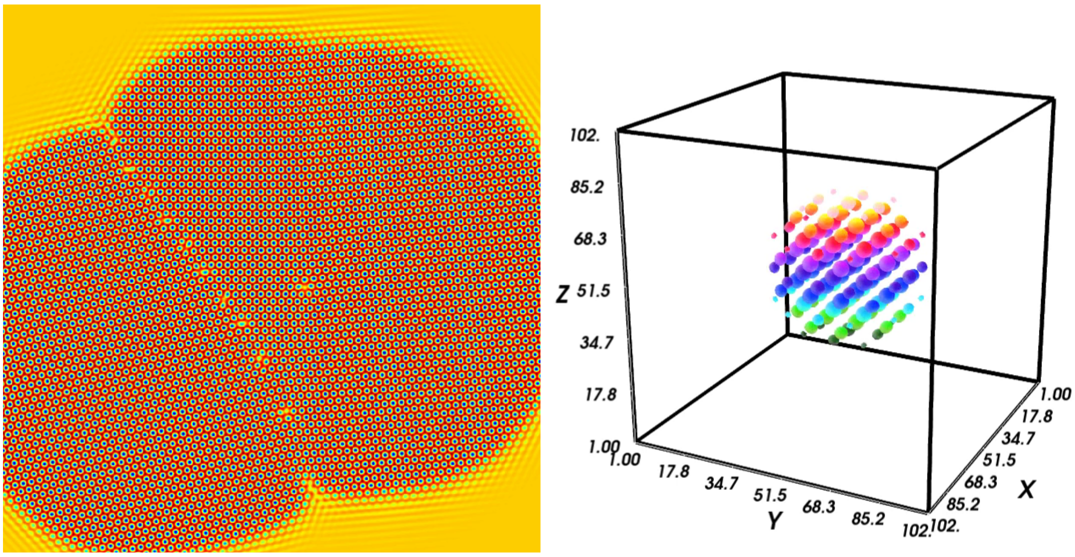

Figure 2.1: Examples of PFC simulations. The left image presents an excerpt of a larger 2D PFC simulation of three grains growing in undercooled melt. Density of the dislocations on the grain boundaries indicates the misalignment between the grains. The right image presents a simulation of a growing grain in undercooled melt in 3D, the colouring of the isosurfaces represents the z coordinate.

the complex amplitudes expansion of the PFC model (APFC).

In the initial formulation of the PFC model, only one crystalline phase was stable, even though it could demonstrate structural phase transformations and stabilize a striped phase under different conditions [5]. The shape of the free energy functional favoured structures where only one peak of the two-point correlation function was sufficient. By adding additional modes in the two point correlation function, additional phases can be stabilized [12, 13]. A completely new approach termed structural PFC model (XPFC) [14, 15] was developed to enable more straightforward modelling of systems with complex phase diagrams. The XPFC model constructs the two particle correlation function from a sum of Gaussian peaks corresponding to more modes of the underlying phase. Further improving the ability of the PFC model to capture complex phase diagrams, the work of [16, 17] demonstrates the use of a three particle correlation functions in order to stabilize complex phases in the context of PFC models. The initial work of [5] introduced a simple binary alloy model, and the works of [18, 19] extended the PFC model to ternary systems.

The PFC model was also extended to describe additional phenomena in combination with the ability to evolve the microstructure of the material. The elastic phenomena were more correctly described in the work of [20]. Improvements in the work of [21] enable modelling of materials with spatial anisotropy and the work of [22, 23] extends the PFC model to liquid crystals. Coupling to ferromagnetic and ferroelectric phenomena was introduced in the works of [24] and [25]. For a more complete overview of the development and applications of the PFC model the reader is referred to a comprehensive overview of different PFC models in work of [26], book on phase field and phase field crystal modelling [4] or more detailed explanations and derivations of specific models in the theses of [27–31].

2.2 Landau theory of phase transitions

Landau's theory of phase transitions is an analytical theory of phase transitions formulated on the basis of a phenomenological free energy functional [32]. The free energy functional is written as a Taylor series expansion of the free energy in terms of the order parameter Ω, around a critical point at which the phase transition occurs. Its main assumption is that for $T \to T_c$ the order parameter becomes arbitrarily small, where T_c is the temperature of phase transition. Phase transitions can be classified based on the discontinuities in the thermodynamic variables at the point of the phase transition into two kinds. Second order phase transitions describe processes where the changes in thermodynamic variables and their derivatives through the phase transition are continuous, while in the first order phase transitions at least one derivative of thermodynamic variables changes discontinuously at transition point. Consequently, the latent heat is only present in phase transitions of the first order. In a first order phase transition the two phases are in coexistence at transition point, while in a second order phase transition the material changes phase continuously and at each point there is only one phase. Examples of phase transitions of the first order are the changes in aggregate state of material (solidification, melting, evaporation), while change in magnetisation in a feromagnetic system when temperature drops below Curie temperature is second order phase transition.

Phase-field models are based on a Landau free energy functional and the PFC method also partially shares this form of the free energy functional.

The free energy of the system is expanded around the transition point in a power series of the order parameter Ω as

$$f(\Omega, T) = a_0 + a_1\Omega + a_2\Omega^2 + a_3\Omega^3 + a_4\Omega^4 + \dots \tag{2.1}$$

where the coefficients are functions of temperature T. Depending on the properties of the system it is possible that higher powers of the order parameters would be required, while for a simple system the first four powers are sufficient. The symmetry of the system also affects the possible values the coefficients a_j might take. For a system in which the free energy does not depend on the sign of the order parameter, the free energy functional has to preserve this symmetry and all odd powers of the order parameter are prohibited.

In a continuous or second order phase transition (i.e. magnetisation) the symmetry prohibits odd powers of the order parameter. The leading term a_0 determines the offset of the free energy and can be set to zero if the free energy is measured from this value. The first non-zero term a_2 must change sign at the phase transition, and therefore in its simplest form must depend on temperature T as $a_2 = \frac{T-T_c}{T_c}\tilde{a}_2$ where $\tilde{a}_2$ is a positive constant. The fourth power coefficient a_4 must be positive, otherwise the free energy would be unbound from below ($f \to -\infty$ for $\Omega \to \pm\infty$). We find minima of the free energy

$$f(\Omega, T) = \frac{T - T_c}{T_c}\tilde{a}_2\Omega^2 + a_4\Omega^4 \tag{2.2}$$

for Ω by derivation $\partial f / \partial\Omega = 0$ and obtain $\Omega = 0, \pm\sqrt{\frac{-\{(T-T_c)/T_c\}\tilde{a}_2}{2a_4}}$. We find that for $T > T_c$ the system has only one minimum, the disordered state at $\Omega = 0$, while at temperatures below T_c, $T < T_c$ two symmetric minima exist at $\Omega = \pm\sqrt{\frac{-\{(T-T_c)/T_c\}\tilde{a}_2}{2a_4}}$. The free energy of this system is presented in Fig. 2.2.

In order to represent a first order phase transition within Landau theory, a cubic term is added to the free energy functional

$$f(\Omega, T) = a_2\Omega^2 + a_3\Omega^3 + a_4\Omega^4 \tag{2.3}$$

This form has minimums at $\Omega = 0, \frac{-3a_3 \pm \sqrt{9a_3^2 - 32a_2a_4}}{8a_4}$. The non-zero minimums become real for $T < T^* = \frac{9a_3^2 T_c}{32a_4\tilde{a}_2} + T_c$ and the non-zero minimum becomes the global minimum for $T < T_1$. At T_1 the optimal value for Ω changes discontinuously from $\Omega = 0$ to a non-zero value, marking a first order phase transition with non zero latent heat. Figure 2.2

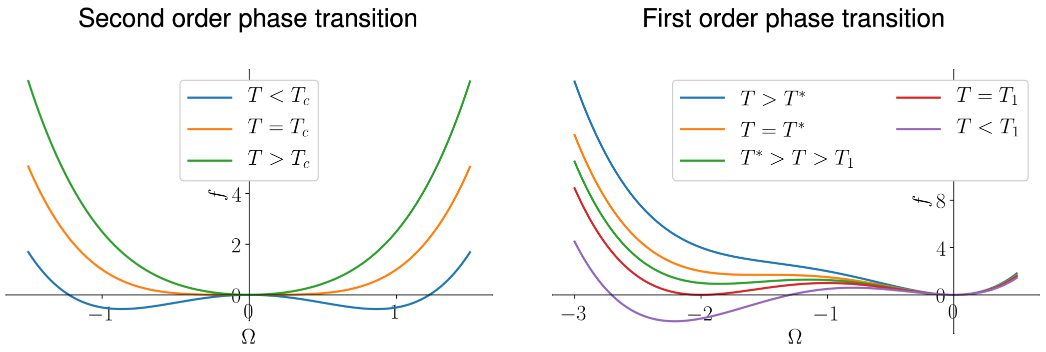

Figure 2.2: Free energies in Landau theory. In a continuous or second order phase transition the value of order parameter Ω changes continuously when the temperature transitions through the phase transition temperature T_c, moving from $\Omega = 0$ to a non-zero value. In a first order phase transition the value of the order parameter changes discontinuously at a phase transition temperature T_1, indicating a phase change with non-zero latent heat.

shows the shape of the free energy functions for different values of T.

2.3 Phase-field crystal model of a pure material

The free energy of a pure material is given by

$$\Delta\mathcal{F} = \Delta\mathcal{F}_{id} + \Delta\mathcal{F}_{ex} + \Delta\mathcal{F}_{ext} \tag{2.4}$$

where $\Delta\mathcal{F}$ is the total free energy of the system, $\Delta\mathcal{F}_{id}$ is the ideal free energy of the system arising from entropy considerations, $\Delta\mathcal{F}_{ex}$ is the free energy due to the interactions between particles and $\Delta\mathcal{F}_{ext}$ is the free energy due to external factors, such as external magnetic or electric fields acting on the system. Expressing the free energy of the system in terms of the atomic density function we obtain

$$\Delta\mathcal{F}_{id}/k_BT = \int d\mathbf{r}\,[\rho\ln(\rho/\rho_0) - \delta\rho] \tag{2.5}$$

where k_B is Boltzmann's constant, T is temperature, $\rho = \rho(\mathbf{r})$, $\delta\rho = \rho - \rho_0$ and ρ_0 is the liquid density at coexistence [11, 33]. The excess free energy of the system according to the CDFT theory is

$$\Delta\mathcal{F}_{ex}/k_BT = \int d\mathbf{r}\left[-\sum_{n=2}^{\infty}\frac{1}{n!}\int\prod_{i=1}^{n} d\mathbf{r}_i\delta\rho(\mathbf{r}_i)C_n(\mathbf{r}_1,\mathbf{r}_2,\dots,\mathbf{r}_n)\right] \tag{2.6}$$

where C_n are the n-particle direct correlation functions of an isotropic fluid [11]. The external free energy contribution is

$$\Delta\mathcal{F}_{ext} = \int d\mathbf{r}M(\mathbf{r})\frac{\delta F}{\delta M} \tag{2.7}$$

where M is the field acting on the material (i.e. magnetic, electric field) [4]. In this thesis we do not model the influence of external fields, therefore this term is always set to 0.

We introduce dimensionless density as $\psi = (\rho - \rho_0)/\rho_0$. To derive the PFC model we expand the ideal free energy term up to ψ^4

$$\Delta\mathcal{F}_{id}/k_BT\rho_0 = \int d\mathbf{r}\left[\frac{\Delta B}{2}\psi^2 - \frac{t}{3}\psi^3 + \frac{v}{4}\psi^4\right] \tag{2.8}$$

where $\Delta B = 1$, $t = 1/2$ and $v = 1/3$ are the parameters obtained through derivation from CDFT, but can be used as free parameters to fit the phase diagram of the material we wish to model.

The excess free energy term that in CDFT theory describes higher order inter particle correlation functions is in PFC model truncated at two particles. Higher order correlation functions are kept in some improvements to the PFC model, notably in [16, 17]. We observe that the two particle correlation function depends only on the distance between the particles $C_2(\mathbf{r},\mathbf{r}') = C_2(|\mathbf{r},\mathbf{r}'|)$, and we can then evaluate the convolution in Fourier space. The Fourier transform of the two particle correlation function is approximated by a polynomial $\hat{C}_2(k) = \hat{C}_{20} + \hat{C}_{22}k^2 + \hat{C}_{24}k^4$ (odd powers are prohibited by symmetry) which we use to fit the first peak of the correlation function. These approximations considerably speed up the calculations at the cost of the peaks in the atomic density function that represent the positions of the atoms becoming more widely spread. The excess free energy term thus becomes

$$\Delta\mathcal{F}_{ex}/k_BT\rho_0 = \int d\mathbf{r}\left[B_X\frac{\psi}{2}(1 + 2\nabla^2 + \nabla^4)\psi\right] \tag{2.9}$$

where the constants $\hat{C}_{20}$,$\hat{C}_{22}$ and $\hat{C}_{24}$ are chosen so that only one constant remains.

The final form of the free energy functional in the PFC model is therefore

$$\Delta\mathcal{F}/k_BT\rho_0 = F = \int d\mathbf{r}\left[\frac{B_L}{2}\psi^2 - \frac{t}{3}\psi^3 + \frac{v}{4}\psi^4 + B_X\frac{\psi}{2}(2\nabla^2+\nabla^4)\psi\right] \tag{2.10}$$

$$= \int d\mathbf{r}\left[\frac{\Delta B}{2}\psi^2 - \frac{t}{3}\psi^3 + \frac{v}{4}\psi^4 + B_X\frac{\psi}{2}(1+\nabla^2)^2\psi\right] \tag{2.11}$$

where $B_L = \Delta B + B_X$. B_L and B_X are isothermal compressibilities of the liquid and solid phase. The initial PFC model [5, 6] was drawn from similarities to other pattern formation models, such as the Swift-Hohenberg model, and did not include the cubic term in the functional. This term can be obtained from the CDFT derivation and is in practice used to adjust the equilibrium density.

2.4 Dynamic equations

The dynamic equations in PF and PFC models are derived from the free energy functional. Depending on the conservation laws for the evolving quantities, Hohenberg and Halperin [34] classified the derivation of dynamic equations in three main model types. Model A is used to evolve a non-conserved order parameter field α,

$$\frac{\partial\alpha}{\partial t} = -M\left(\frac{\delta F}{\delta\alpha}\right) + \theta \tag{2.12}$$

model B describes the dynamics of a conserved order parameter β

$$\frac{\partial\beta}{\partial t} = M\nabla^2\left(\frac{\delta F}{\delta\beta}\right) + \theta \tag{2.13}$$

and model C describes the dynamics in a system of co-evolving conserved and non-conserved order parameters

$$\begin{aligned}\frac{\partial\alpha}{\partial t} &= -M_\alpha\left(\frac{\delta F}{\delta\alpha}\right) + \theta_\alpha\\ \frac{\partial\beta}{\partial t} &= M_\beta\nabla^2\left(\frac{\delta F}{\delta\beta}\right) + \theta_\beta\end{aligned} \tag{2.14}$$

where the constants M describe mobility and θ describe thermal fluctuations.

The PFC model is evolved using dissipative dynamics of model B [4, 26]

$$\frac{\partial\psi}{\partial t} = \Gamma\nabla^2\left(\frac{\delta F}{\delta\psi}\right) + \eta = \Gamma\nabla^2\left(B_L\psi - t\psi^2 + v\psi^3 + B_X(2\nabla^2 + \nabla^4)\psi\right) + \eta \tag{2.15}$$

where Γ is a constant normally set to 1 and η is stochastic noise with zero mean and correlations $\langle\eta(\boldsymbol{r},t)\eta(\boldsymbol{r'},t')\rangle = -\Gamma k_B T\nabla^2\delta(\boldsymbol{r}-\boldsymbol{r'})\delta(t-t')$, set to 0 in this thesis.

2.5 Phase diagram

The PFC equation 2.11 has no analytical solutions, therefore in order to derive quantitative conclusions about the phases that can be formed in the model, some approximations must be made. Due to the scaling of the computational power required for simulations, all simulations in this thesis were performed in 2D as this suffices to verify the developed improvements. Therefore we are interested in a phase diagram of 2D PFC model. To be able to analytically describe the dependence of the free energy on parameters, we take a one-mode approximation of the atomic density function. In 2D the crystalline phase has triangular symmetry, and therefore the one mode approximation to the solution is

$$\psi(\mathbf{r}) = A\sum_{j=1}^{3}\left(e^{i\mathbf{k_j}\cdot\mathbf{r}} + e^{-i\mathbf{k_j}\cdot\mathbf{r}}\right) + \overline{\psi} \tag{2.16}$$

$$= 2A\sum_{j=1}^{3}\cos(\mathbf{k}_j\cdot\mathbf{r}) + \overline{\psi} \tag{2.17}$$

where $\overline{\psi}$ is the average density and

$$\mathbf{k}_1 = k_0(-\boldsymbol{i}\sqrt{3}/2 - \boldsymbol{j}/2), \qquad \mathbf{k}_2 = k_0\boldsymbol{j}, \qquad \mathbf{k}_3 = k_0(\boldsymbol{i}\sqrt{3}/2 - \boldsymbol{j}/2) \tag{2.18}$$

are the basis vectors of the 2D crystalline phase with triangular symmetry. Substituting the ansatz (2.17) into equation (2.11) and noting that all terms apart from constant terms vanish in the integration over the entire domain, we obtain [27]

$$\begin{aligned} f = F/V = \quad & B_L\left(\frac{\overline{\psi}^2}{2} + 3A^2\right) - t\left(\frac{\overline{\psi}^3}{3} + 2\overline{\psi}A^2 + 4A^3\right) \\ + \quad & v\left(\frac{\overline{\psi}^4}{4} + 9\overline{\psi}^2A^2 + 12\overline{\psi}A^3 + \frac{45}{2}A^4\right) + 3B_X(-2k_0^2 + k_0^4)A^2 \end{aligned} \tag{2.19}$$

In calculation it is necessary to take into account that for some combinations of wave vectors their sum is zero, and therefore the result is a non-vanishing constant term (i.e. $\mathbf{k}_1 + \mathbf{k}_2 + \mathbf{k}_3 = 0$). We derive the free energy optimal wave vector [27]

$$\frac{\partial f}{\partial k_0} = 12 B_X A^2 (-k_0 + k_0^3) = 0 \tag{2.20}$$

with solutions $k_0 = 0, \pm 1$. $k_0 = 0$ corresponds to the liquid state where the atomic density function is constant in space, $\psi(\mathbf{r}) = \overline{\psi}$. The free energy of the liquid state is therefore

$$f_{liquid} = \frac{B_L}{2} \overline{\psi}^2 - \frac{t}{3} \overline{\psi}^3 + \frac{v}{4} \overline{\psi}^4 \tag{2.21}$$

To derive the free energy of the solid state, we insert $k_0 = 1$ into equation (2.19) and take a derivative [27]

$$\frac{\partial f}{\partial A} = 6 B_L A - t(4\overline{\psi} A + 12 A^2) + v(18 \overline{\psi}^2 A + 36 \overline{\psi} A^2 + 90 A^3) - 6 B_X A = 0 \tag{2.22}$$

with solutions $A_0 = 0$ and

$$A_{1,2} = \frac{t - 3 v n_0 \pm \sqrt{t^2 + 24 t v \overline{\psi} - 36 v^2 \overline{\psi}^2 - 15 v \Delta B}}{15 v} \tag{2.23}$$

The optimal phase for given parameters is therefore determined by comparison of the free energies given by inserting the parameters (A, k_0) that describe the given phase into the free energy equation (2.19). We derive the coexistence regions using a common tangent construction and solve the equations numerically. The phase diagram of the original PFC model [6] is presented in Fig. 2.3. We note that in 2D PFC model a striped/planar phase can also be stabilized, therefore in order to derive the complete phase diagram, we would have to repeat the procedure of deriving the free energy of the selected phase for the striped phase as well, using a striped phase ansatz instead of the ansatz for the crystalline phase in eq. (2.17). Since this thesis is mainly concerned with simulations in the crystalline phase, we will not perform this derivation.

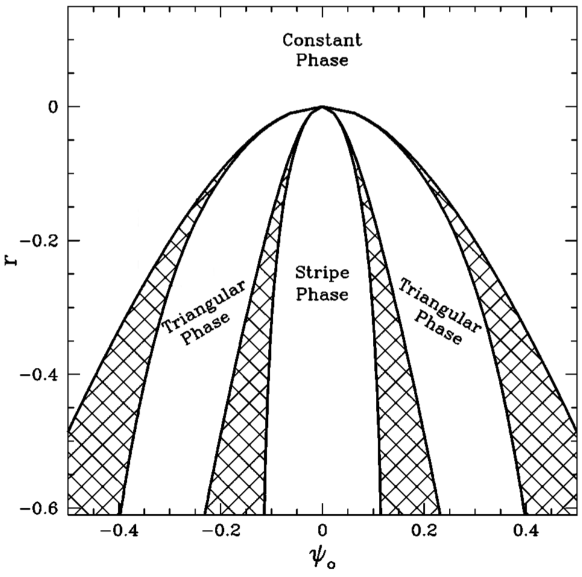

Figure 2.3: Phase diagram of the original PFC model [6]. Reprinted figure with permission from Elder and Grant, Physical Review E 70, 051605 (2004). Copyright (2019) by the © *American Physical Society.* DOI: http://doi.org/10.1103/PhysRevE.70.051605.

2.6 Elasto-plasticity in the PFC model

The PFC model is based on minimization of the free energy given by a functional that is designed to favour periodic solutions. The periodicity of solutions already guarantees that the elasticity will be properly included in the model. If we expand the free energy of the whole system around the equilibrium lattice constant a_{eq}, the dependency on lattice constant a

$$F(a) = F(a_{eq}) + \underbrace{\frac{\partial F}{\partial a}|_{a_{eq}}}_{=0}(a - a_{eq}) + \frac{1}{2}\frac{\partial^2 F}{\partial a}|_{a_{eq}}(a - a_{eq})^2 + \cdots \tag{2.24}$$

forms a Hooke's law [4]

$$\Delta F = \frac{1}{2}\frac{\partial^2 F}{\partial a}|_{a_{eq}}(\Delta a)^2 \tag{2.25}$$

since F is minimal for $a = a_{eq}$ and therefore the first derivative is zero ($\Delta a = a - a_{eq}$, $\Delta F = F(a) - F(a_{eq})$).

The initial PFC model could already demonstrate the familiar stress-strain relationship and transition from elastic to plastic deformations [6]. However, since the PFC model is based on diffusive processes, the correct treatment of the plastic deformations requires an additional improvement to the model in the form of a second time derivative [35]. The stress-strain curve of the PFC model shows the initial elastic region followed by the region of plastic deformations. Figure 2.4 presents this relationship for systems with different average grain sizes.

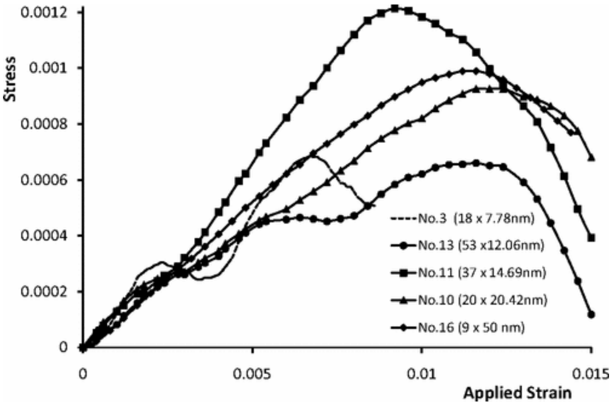

Figure 2.4: Stress-strain plots for a modified PFC model developed by Stefanovic *et al.* [35]. Reprinted figure with permission from Stefanovic, Haataja and Provatas, Physical Review E 80, 046107 (2009). Copyright (2019) by the © *American Physical Society.* DOI: http://doi.org/10.1103/PhysRevE.80.046107.

Elastic constants in the PFC model can be calculated from the free energies of deformed samples. The type of the deformation determines the transformation of the crystal lattice. Three different deformations representing bulk, shear and deviatoric deformation are given by the following transformations (in 2D) [6]:

$$\psi_{blk}(\mathbf{r}) = \psi(x/(1+\xi), y/(1+\xi)) \tag{2.26}$$

$$\psi_{shr}(\mathbf{r}) = \psi(x+\xi y, y) \tag{2.27}$$

$$\psi_{dev}(\mathbf{r}) = \psi(x/(1+\xi), y/(1-\xi)) \tag{2.28}$$

where ξ is the dimensionless deformation parameters. In order to derive an analytical expression for the free energies and derive the elastic constants, we use the approximation of the atomic density function in eq. (2.17) and the note that for a 2D system, the free energy of deformed lattices under specified deformations is [36, 37]

$$F_{blk} = F_{min} + [C_{11} + C_{12}]\xi^2 + \dots \tag{2.29}$$

$$F_{shr} = F_{min} + [C_{44}/2]\xi^2 + \dots \tag{2.30}$$

$$F_{dev} = F_{min} + [C_{11} - C_{12}]\xi^2 + \dots \tag{2.31}$$

The resulting elastic constants for the case of a simple 1-mode PFC model are [6]

$$C_{11}/3 = C_{12} = C_{44} = \alpha/4 \tag{2.32}$$

where $\alpha = A^2/4$. The simplest form of the PFC model therefore has all the expected elastic constants with correct symmetry (for triangular system we expect $C_{11} = C_{12} + 2C_{44}$). On the downside, only one elastic constant can be chosen to match the parameters of a given material.

Chapter 3

Amplitude Expansion of the Phase-Field Crystal Model

3.1 Introduction

The amplitude expansion of the phase field crystal model (APFC) is an extension of the PFC model that expresses the atomic density function in terms of complex amplitudes, describing amplitudes of waves aligned with a chosen set of basis vectors. In Fig. 3.1 the relationship between the complex amplitudes and the atomic density is illustrated. The extension was initially developed by Goldenfeld *et al.* [7, 8] and was derived from the PFC model using a renormalization group based approach. Figure 3.2 presents an example of APFC model simulations.

The APFC model has already been used for investigation of grain boundaries and grain boundary motion in 2D and 3D [7, 8, 38–43], heteroepitaxial ordering of thin films [44–47] and structural phase transitions [48]. It has been improved to describe binary systems [10, 49, 50] and different crystal structures (honeycomb, square in 2D, fcc and bcc in 3D) [46, 48, 49, 51, 52]. Developed APFC model improvements also include the ability to achieve instantaneous mechanical equilibrium [53], coupling of the microstructure evolution to an external field [54] and tuning the energies of defects [55].

The slow variance of the complex amplitudes used in the model allow AMR techniques to be used in the APFC model [9], and the sum of squares of the amplitudes indicates the aggregate state of the matter, connecting the APFC models to the PF models [43].

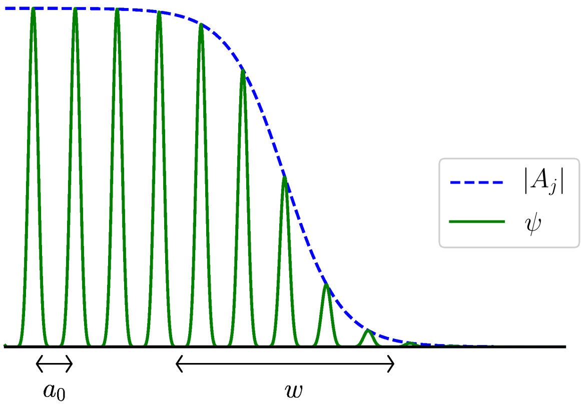

Figure 3.1: Idea of the complex amplitudes: express the fast varying atomic density field ψ with slowly varying complex amplitudes A_j. The atomic density field ψ changes rapidly on a length scale of the atomic lattice a_0, while the complex amplitudes A_j change more slowly over length scales comparable with the interface width w.

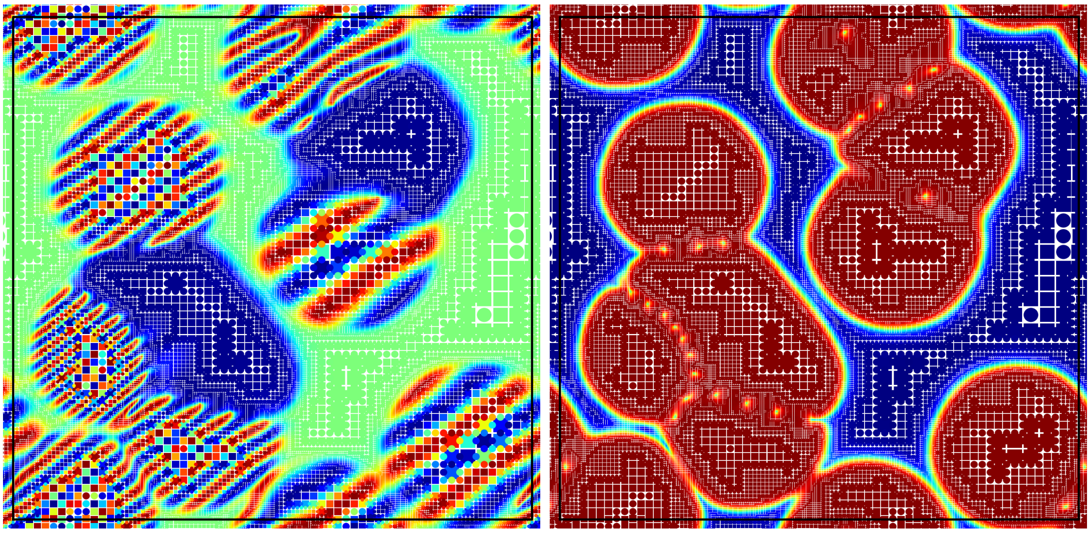

Figure 3.2: Example of APFC simulations. Left image presents $\Re(A_1)$. The pattern of periodic oscillations in the complex amplitudes is called "beats" and is an expression of the rotation of the grains. Faster beating indicates grains that are rotated by a larger angle with regard to the initial choice of the base vectors $\mathbf{k}_j$. Right image presents $\sum_j |A_j|/3$. The values of the complex amplitudes drop in dislocation cores and in the liquid regions.

3.2 APFC model

The APFC model has been derived from the PFC model in three main ways. The first derivation [7–9, 38] was based on renormalization group approach, the second option is a multiple-scales expansion used in the works of [49, 50, 56, 57] and the third possibility is to use a volume averaging and coarse graining approach [48, 58, 59]. The last mentioned approach has also been used to derive an APFC model capable of modelling structural transformations in solid state with two different crystal symmetries coexisting [48]. The approach presented here is based on volume averaging and coarse graining technique.

In the APFC model, the complex amplitudes A_j represent the amplitudes of density waves, aligned with a set of basis vectors. To model crystals with triangular symmetry, the following ansatz is used

$$\begin{aligned} \psi = \sum_{j=1}^{3} A_j e^{i\mathbf{k_j}\cdot\mathbf{x}} \qquad & + \sum_{j=1}^{3} A_j^* e^{-i\mathbf{k_j}\cdot\mathbf{x}} \qquad & + \overline{\psi} \\ = \sum_{j=1}^{3} A_j e^{i\mathbf{k_j}\cdot\mathbf{x}} \qquad & + CC \qquad & + \overline{\psi} \end{aligned} \tag{3.1}$$

where CC denotes the complex conjugate of the preceding expression, $A_j = A_j(\mathbf{r})$ are the spatially dependant complex amplitudes, $\mathbf{k}_j$ are basis vectors defined in the same way as in eq. (2.18)

$$\mathbf{k}_1 = k_0(-\boldsymbol{i}\sqrt{3}/2 - \boldsymbol{j}/2), \qquad \mathbf{k}_2 = k_0\boldsymbol{j}, \qquad \mathbf{k}_3 = k_0(\boldsymbol{i}\sqrt{3}/2 - \boldsymbol{j}/2) \tag{3.2}$$

with $k_0 = 1$ and $\overline{\psi} = \overline{\psi}(\mathbf{r})$ is the spatially dependant average density. The coarse graining technique convolves the density function with a volume-averaging, smoothing function as [18, 48, 60]

$$\langle f(\mathbf{r})\rangle_V = \int_{-\infty}^{+\infty} d\mathbf{r} f(\mathbf{r}')\xi_V(\mathbf{r}-\mathbf{r}') \tag{3.3}$$

where $f(\mathbf{r}')$ is the function being coarse grained, ξ is the smoothing function and $\langle f(\mathbf{r})\rangle$ is the coarse grained function. The smoothing function is normalized to unity

$$\int_{-\infty}^{+\infty} d\mathbf{r}\xi_V(\mathbf{r}) = 1 \tag{3.4}$$

In our case we choose a normalizing function that is constant inside the unit cell of the crystal and zero elsewhere

$$\xi_V(\mathbf{r}) = \begin{cases} 1/V_0 & \text{inside unit cell} \\ 0 & \text{otherwise} \end{cases} \tag{3.5}$$

In order to derive the coarse grained free energy functional we insert the ansatz (3.1) into the PFC model's free energy (2.11), change the order of integration and derive the free energy functional in terms of the complex amplitudes [48, 52]

$$\begin{aligned} F = \quad & \int d\mathbf{r} \left[\frac{\overline{\psi}^2}{2} - t\frac{\overline{\psi}^3}{6} + v\frac{\overline{\psi}^4}{12} + (1 - t\overline{\psi} + v\overline{\psi}^2) \left(\sum_{j=1}^{3} |A_j|^2 \right) \right. \\ & \quad -(t - 2v\overline{\psi})[A_1 A_2 A_3 + A_1^* A_2^* A_3^*] + \frac{v}{2} \left[\sum_{j=1}^{3} |A_j|^4 \right] \\ & \left. +2v \left[\sum_{j=1}^{3} \sum_{m>j}^{3} |A_j|^2 |A_m|^2 \right] + B_X \sum_{j=1}^{3} |(\nabla^2 + 2i\mathbf{k}_j \nabla) A_j| \right] \end{aligned} \tag{3.6}$$

where we have truncated the series expansion of $\hat{C}_2$ in Fourier space at k^4 like before. To derive more accurate results it is possible to keep the full form of the $\hat{C}_2$ and perform the numerical integrations in Fourier space [48], or extend the series to higher powers of k [61]. The dynamic equations for the amplitudes can be derived using model C dynamics [49] described in eq. (2.14)

$$\frac{\partial \overline{\psi}}{\partial t} = \nabla^2 \frac{\delta F}{\delta \overline{\psi}} \tag{3.7}$$

$$\frac{\partial A_j}{\partial t} = -\frac{\delta F}{\delta A_j^*} \tag{3.8}$$

It is also possible to derive an amplitude representation of the equations for binary alloy [49] or include fast relaxation of elastic deformations into the equations [53].

3.2.1 Comparison of APFC and PFC models

In comparison to the PFC models, the APFC model has several advantages. First, as the amplitudes change more slowly with space the spacing between the computational points can be larger. This increases the size of the domain that we can model and the time span through which we can track the evolution of the microstructure on similar hardware as with the PFC model. Second, as the complex amplitudes effectively track the amplitudes of the atomic density function and do not describe the fluctuations in atomic density on the scale of the atomic lattice, the amplitude equations have properties that can enable the use of AMR techniques and thus increase the reach of the simulations even further.

As a tradeoff, the APFC formulation also introduces some new problems. First, if the grains are not aligned with the initial choice of base vectors, the rotation of the grains is expressed through the so called beats in the amplitudes, which reduces the applicability of the AMR techniques. This problem has been solved either by converting the complex amplitudes into their polar representation [9] or by the introduction of an auxiliary local rotation field [62] as described in Chapter 5. Second, since the amplitudes do not track the association between rotation of the grains and the basis vectors, an unphysical grain boundary appears between grains misaligned for a multiple of the crystal's symmetry rotation. This limits the application of the APFC models merely to cases where misalignment between grains is small (less than half of a crystal's symmetry rotation). Chapters 6 and 7 propose and test a solution to this problem.

3.2.2 Grain rotation in APFC models

Since the ansatz for the PFC model presented in eq. (3.1) describes the atomic density function of the PFC model in terms of amplitudes of the waves aligned with the initial choice of base vectors in equation (3.2), one might expect that the APFC model is limited to modelling only grains, aligned with the initial choice of base vectors. This is not correct, as in the APFC model, the rotation of the grains can be expressed through the so called beats in the complex amplitudes A_j. We can derive the beats by expressing the atomic density function of a grain, rotated by angle ϑ with regard to the base vectors in eq. (3.2).

$$\begin{aligned}
\psi(\vartheta) = & \sum_{j=1}^{3} A_j^{\vartheta} e^{i\mathbf{k}_j(\vartheta)\cdot\mathbf{x}} & +CC & & +\overline{\psi} & \qquad (3.9)\\
= & \sum_{j=1}^{3} A_j^{\vartheta} e^{i\delta\mathbf{k_j}(\vartheta)} e^{i\mathbf{k}_j\cdot\mathbf{x}} & +CC & & +\overline{\psi} & \qquad (3.10)\\
= & \sum_{j=1}^{3} A_j e^{i\mathbf{k}_j\cdot\mathbf{x}} & +CC & & +\overline{\psi} & \qquad (3.11)
\end{aligned}$$

where $\mathbf{k}_j(\vartheta) = \mathbf{k}_j + \delta\mathbf{k}_j(\vartheta)$ are rotated basis vectors and A_j^ϑ are the rotated complex amplitudes (the amplitudes we would have, had we chosen a rotated set of the initial basis vectors). By comparing the terms with matching exponential functions, we derive the following relationship between rotated and non-rotated complex amplitudes:

$$A_j = A_j^\vartheta e^{i\delta\mathbf{k}_j(\vartheta)\cdot\mathbf{x}} \tag{3.12}$$

meaning that a grain that is rotated by an angle of ϑ will exhibit so called beats, that are periodic oscillations in phase in a direction parallel to $\delta\mathbf{k}_j(\vartheta)$, with increasing frequency of the beats as the rotation increases. Figure 3.3 illustrates this phenomena, showing beats in three grains rotated by 0°, 5° and 25° in combination with the rotated and non-rotated base vectors $\mathbf{k}_j$.

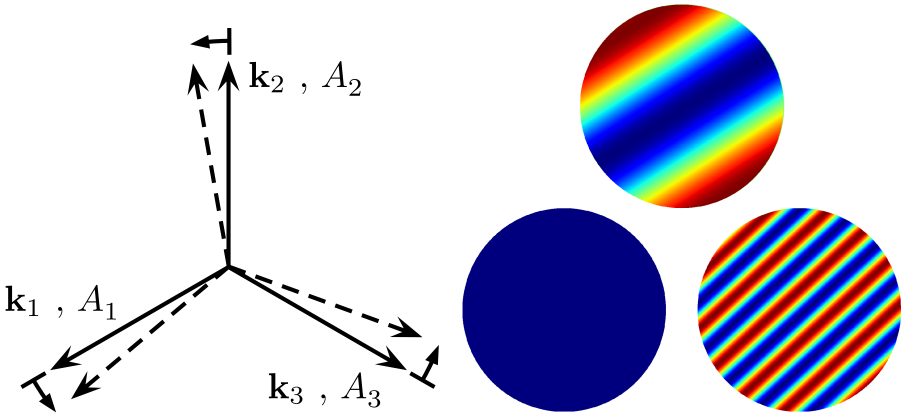

Figure 3.3: Base vectors for the complex amplitudes A_j and their rotation. Grain rotation is expressed through the so-called beats in the complex amplitudes of rotated grains in the APFC model. Right image shows the beats in $\Re(A_1)$, in three grains, rotated for (clockwise from bottom left) $\theta = 0°$, $5°$ and $25°$.

The invariance of the model to the rotation of the chosen base vectors is also expressed through the rotational covariance of the operator $\mathcal{L}_j = \nabla^2 + 2i\mathbf{k}_j\nabla$ which is applied on the complex amplitudes A_j. In derivation of the free energy and dynamic equations for the complex amplitudes the operator ∇^2 is substituted for its covariant form $\nabla^2 \rightarrow \nabla^2 + 2i\mathbf{k}_j\nabla - |\mathbf{k}_j|^2$ [48].

3.2.3 Unphysical grain boundary in APFC models

One of the shortcomings of the amplitude representation is the occurrence of an unphysical grain boundary between grains rotated for a crystal's symmetry rotation [10]. The origin of this phenomena can be attributed to the inability of the APFC model to correlate the rotation expressed through the beats in the complex amplitudes with the rotations of the base vectors that represent the beating amplitudes. If, for example, a grain boundary is formed between grains rotated by 0° and 60°, both grains represent physically the same crystal in systems with triangular symmetry, but the rotation of the second grain is expressed through the beats in amplitudes which are not matched in the first grain. Therefore a grain boundary appears between both grains, even though there should be no grain boundary. Figure 3.4 presents the real part of the first complex amplitude in grains rotated by 0°, 60°, $-30°$ and $+30°$, forming vertical grain boundaries with 60° mismatch. We can observe that the beats in complex amplitudes on both sides of the vertical grain boundary do not align indicating an increase in the free energy there (a grain boundary), even though the vertical grain boundary, representing a 60° mismatch that matches the crystal's symmetry rotation, physically does not exist (a crystal rotated by its symmetry rotation is the same as the original crystal). To even better demonstrate the problem, we simulated a set of 10 circular grains growing in an undercooled melt, with rotations in steps by 6°, from $-27°$ to $+27°$, presented in Fig. 3.5. The mismatch between each pair of grains is the same (6°, taking into account that rotations for $-30°$ and $+30°$ represent the same crystal) and therefore we would expect similar grain boundary structures. This is true for all grain boundaries except for the one between grains rotated by $-27°$ and $+27°$, which reflects the properties of a grain boundary with 54° mismatch. The enlarged excerpts of the image present the structure of the unphysical grain boundary, and the correction to the structure that is achievable with the solution we propose in Chapter 6. The dislocation cores are areas in the images where the free energy raises above the free energy of the crystal, as shown in the excerpts, or areas where the sum of all amplitudes $\sum_j |A_j|/3$ decreases below a certain value, as shown in the image of the entire simulation domain. We can observe that the dislocation density, after application of our proposed correction, is the same on all grain boundaries.

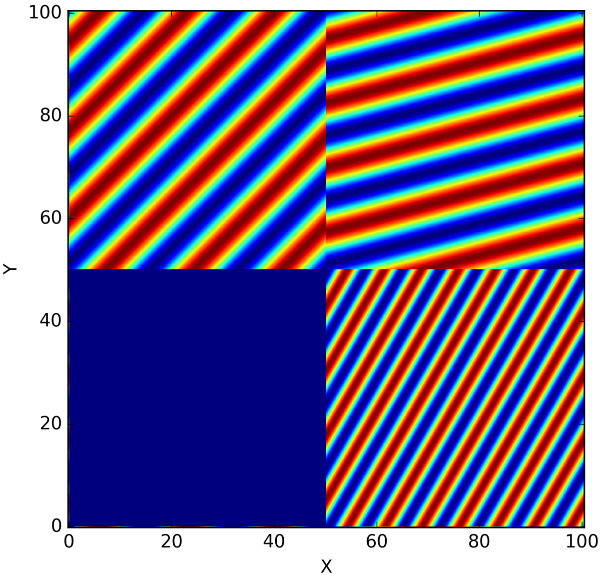

Figure 3.4: Unphysical grain boundary is formed due to the mismatch between beats that represent the rotated grain and the non-rotated grain. The image shows $\Re(A_1)$ in 4 seeds, clockwise from $(0,0)$ rotated by 0°, +30°, −30° and 60°. The unphysical grain boundary is formed on the vertical line separating these grains as the grains on the right are rotated by 60° more than the grains on the left, therefore the complex amplitudes do not match and an unphysical grain boundary is formed, even though the grains represent physically the same crystal.

3.3 Polar representation of complex amplitudes

In order to eliminate the problem of beats in complex amplitudes A_j, Athreya *et al.* [9] derived a polar representation of the complex amplitude equations. The complex amplitude and phase and amplitude equations are listed here for comparison.

$$\frac{\partial A_j}{\partial t} = \tilde{\mathcal{L}}_j A_j - 3A_j|A_j|^2 - 6A_j \sum_{k:k\neq j} |A_k|^2 - 6\overline{\psi} \prod_{k:k\neq j} A_k^* \tag{3.13}$$

$$\begin{aligned}\frac{\partial \Psi_j}{\partial t} =& (r + 3\overline{\psi}^2)[-\Psi_j + \mathcal{C}^{\mathrm{Re}}(\Psi_j, \Phi_j)] - 3\Psi_j \left(\Psi_j^2 + 2\sum_{k\neq j} \Psi_k^2 \right) \\ & - 6\frac{\overline{\psi}}{\Psi_j} \left(\prod_k \Psi_k \right) \cos\left(\sum_k \Phi_k \right) \\ \frac{\partial \Phi_j}{\partial t} =& \frac{(r + 3\overline{\psi}^2)\mathcal{C}^{\mathrm{Im}}(\Psi_j, \Phi_j)}{\Psi_j} + 6\frac{\overline{\psi}}{\Psi_j^2} \left(\prod_k \Psi_k \right) \sin\left(\sum_k \Phi_k \right)\end{aligned} \tag{3.14}$$

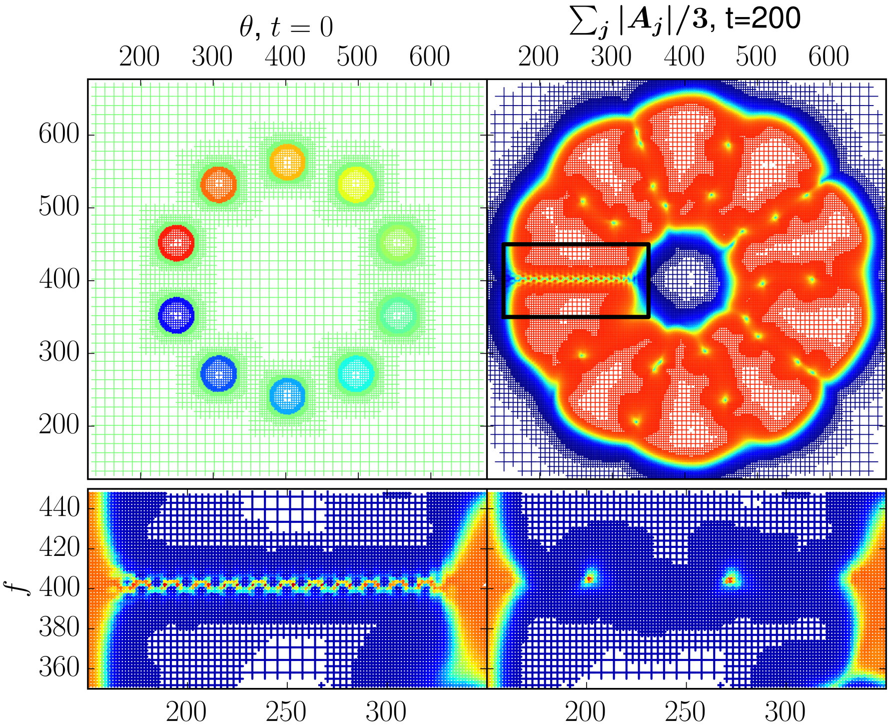

Figure 3.5: Formation of an unphysical grain boundary between grains. First row: 10 seeds with rotations in steps by 6^0, from -27^o to $+27^o$ are placed in a circle and grown so that a grain boundary is formed between each pair of neighbouring seeds. The region with the boundary between seeds with orientations of -27^o and $+27^o$ is enlarged in the second row where the free energy is presented. Left image in the second row shows the free energy formed in an APFC model as presented in this chapter, and the right image shows the free energy formed in an improved model that we present in later chapters of this thesis and can remove this phenomena. The left image effectively represents a grain boundary with 54° mismatch as the APFC model can not connect the rotation of basis vectors with the rotation expressed by the beats of the complex amplitudes, while the right image shows the correct structure of a 6° grain boundary.

where

$$\tilde{\mathcal{L}}_j = (1 - \nabla^2 - 2i\mathbf{k}_j \cdot \nabla)(-r - 3\overline{\psi}^2 - \{\nabla^2 + 2i\mathbf{k}_j \cdot \nabla\}^2) \tag{3.15}$$

is a rotationally covariant operator and the complex amplitudes A_j are split into phase and amplitude as $A_j = A_j = \Psi \exp(i\Phi_j)$ and

$$\begin{aligned} \mathcal{C}^{\mathrm{Re}}(\Psi_j, \Phi_j) &= \mathrm{Re}\left\{\frac{(\nabla^2 + 2i\mathbf{k}_j\nabla)(\Psi_j \exp(i\Phi_j))}{\exp(i\Phi_j)}\right\} \\ \mathcal{C}^{\mathrm{Im}}(\Psi_j, \Phi_j) &= \mathrm{Im}\left\{\frac{(\nabla^2 + 2i\mathbf{k}_j\nabla)(\Psi_j \exp(i\Phi_j))}{\exp(i\Phi_j)}\right\} \end{aligned} \tag{3.16}$$

To derive the dynamic equations for the phase and amplitude (3.14) in presented, simplified form, it is necessary to discard third and higher order derivatives of Ψ_j and Φ_j, assume a "frozen gradient approximation" which presumes that the gradient of phase $\nabla\Phi_j$ is constant within all solidified grains and split the computational domain into two parts, the interior of the solidified grains where the phase and amplitude equations (3.14) are solved and the area where material is not completely solidified (solidification front and area around dislocations and on the boundary between grains) where the complex amplitude equations (3.13) are solved. Furthermore, care must be taken as the phase of the amplitudes Φ_j calculated from the complex amplitudes A_j as $\Phi_j = \arctan(\mathrm{Im}(A_j)/\mathrm{Re}(A_j))$ has discontinuities where it changes for 2π.

Despite the challenges listed, Athreya *et al.* [9] successfully implemented a numerical algorithm that could remove the beats in variables and demonstrated mesh refinement in all grains. This was a significant step towards enabling APFC simulations in larger domains. Unfortunately, the procedure was not widely adopted and presently most APFC simulations still use regular grid. Another possibility to solve this problem is presented in [62] (chapter 5) and is a part of the contribution of this thesis.

3.4 Connection to phase-field models

Phase-Field models have been successfully applied to many phenomena [63]. The success of such models originates in transforming the description of a grain boundary or a solidification front from a set of equations describing the phenomena at the interface to a set of continuous equations expressing the evolution of a continuous phase field that does not require knowing where the interface is at all times. Since the amplitude of the complex amplitudes (or their sum, i.e. $\sum_j |A_j|^2$) also describes the aggregate state of the matter, the PFC model in its amplitude representation can be seen as the connecting link between the first-principles derived CDFT methods and the phenomenologically founded PF methods. Here we briefly give an example of a phase field model that can be derived from APFC models, which in turn can be derived from PFC models and connected to first principles through CDFT. The connection is made by expressing the complex amplitudes in terms of a variable denoting the aggregate state of the material ϕ ($\phi = 0$ in liquid and $\phi \neq 0$ in solid) and a slowly varying deformation vector $\mathbf{u}$ as [49]

$$A_j = \phi \exp(i\mathbf{k}_j \cdot \mathbf{u}) \tag{3.17}$$

The derived phase field free energy functional for a binary alloy is

$$\begin{aligned} F =& d\mathbf{r}\Bigg[\left\{3\Delta B_0\phi^2 - 4t\phi^3 + \frac{45}{2}v\phi^4 + (\omega + 6B_2^l\phi^2)\frac{\psi^2}{2} + \frac{u}{4}\psi^4\right\} \\ &+ \left\{\frac{K}{2}|\nabla\psi|^2 + 6B_0^X|\nabla\phi|^2\right\} + 3B_0^X\left\{\sum_{i=1}^{2}\left(\frac{3}{2}U_{ii}^2\right) + U_{xx}U_{yy} + 2U_{xy}^2\right\}\phi^2 \\ &+ 12\alpha B_0^X\left\{-\phi\nabla^2\phi + \sum_{i=1}^{2}U_{ii}\phi^2\right\}\psi\Bigg] \end{aligned} \tag{3.18}$$

where ψ is a concentration field and $U_{ij} = (\partial u_i/\partial r_j + \partial u_j/\partial r_i)/2$ is the linear strain tensor. The connection is apparent from the degree of similarity between the terms in the curly brackets $\{\dots\}$ and the PF models for eutectic and dendritic solidifications [64, 65], see [49] for derivation.

Chapter 4

Numerical methods

4.1 Introduction

Numerical methods describe our search for usable solutions to mathematical problems where analytical solutions do not exist or we haven't found them yet. The search for approximate solutions to problems we can't solve exactly has been present in human history for a long time. One of the first examples is the use of a numerical algorithm to calculate the square root of 2 used already in Babylon, where the results of the algorithm had to be precise enough to be usable in construction and astronomy (see Fig. 4.1). In modern computational materials science we build material models with emphasis on

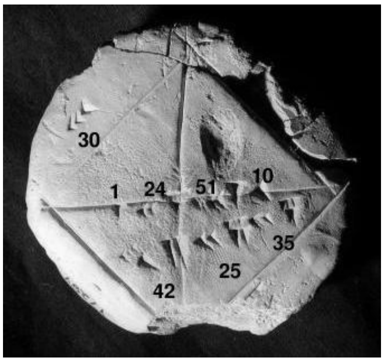

Figure 4.1: Babylonian clay tablet with numeric approximation of $\sqrt{2}$, accurate to about 6 decimal digits. The Babylonian algorithm to calculate the square root of a number N is: 1. make an initial guess x_0, 2. improve the guess by $x_{n+1} = (x_n + N/x_n)/2$, 3. repeat until convergence. Copyright Bill Casselman and Yale Babylonian Collection [66].

the usability of the results. This means that we have to balance the precision of the model against the computational time that the simulation would require, which demands we make efficient use of the computational resources at our disposal. AMR algorithms allow us to use the computational power efficiently, as they effectively reduce the amount of computational power spent on modelling parts of the material where “not much is happening” (i.e. the interior of solidified grains) and focus it on where the important phenomena occurs (i.e. on the solidification front or on the grain boundaries). The success of AMR techniques is based on spatial averaging in the sense that where the fields that represent the material do not change much, the average field values of larger amounts of material can be modelled together in effectively coarser computational mesh.

This approach to reducing the number of computational nodes arises form the ability to average fields over long distances, which cannot be performed on the atomic density field of the PFC model as that filed varies quickly. The APFC model enables the application of the AMR techniques as the complex amplitudes vary on much slower scales and change rapidly only where important phenomena occurs. Improvements that enable APFC modelling on larger scales are therefore an important stepping stone in the development of models that can describe microstructure in larger domains.

4.2 Finite difference method

The finite difference method approximates the function on a discrete computational mesh. In order to be able to do that, the approximated function has to be “properly behaved” (i.e. it has no poles in the range where it is approximated) and can be expanded into a Taylor series. Most functions describing physical properties are such, so this method is widely applied to solving real physical problems. The main problem we want to solve in this thesis is described by the dynamic equations for the complex amplitudes, i.e. the equations described in (3.13) repeated here

$$\frac{\partial A_j}{\partial t} = \tilde{\mathcal{L}}_j A_j - 3A_j|A_j|^2 - 6A_j \sum_{k:k\neq j} |A_k|^2 - 6\overline{\psi} \prod_{k:k\neq j} A_k^* \tag{4.1}$$

for

$$\tilde{\mathcal{L}}_j = (1 - \nabla^2 - 2i\mathbf{k}_j \cdot \nabla)(-r - 3\overline{\psi}^2 - \{\nabla^2 + 2i\mathbf{k}_j \cdot \nabla\}^2) \tag{4.2}$$

which have no known analytical solutions. The system of equations (4.1) presents an *initial value problem* [67] as the initial values of $A_j(\mathbf{r})$ are known and defined by the seeds with which we start the simulation. In order to solve the given system of equations, we need to discretise the space and time domains of our simulation. The continuous function of space is in the simplest form discretised by sampling at regular intervals.

A differential equation is then solved numerically by approximating the derivatives by a chosen differentiation scheme. In the 1D case we derive the differentiation scheme from the Taylor expansion of function f around point x

$$\begin{aligned} f(x+h) &= f(x) + f'(x)h + h^2(\dots) \\ &\Downarrow \text{(up to } h^2\text{)} \\ f'(x) &= \frac{f(x+h) - f(x)}{h} \\ &\Downarrow \text{(discretised on regular grid, } x = nh, f(nh) = f_n\text{)} \\ f'_n &= \frac{f_{n+1} - f_n}{h} \end{aligned} \tag{4.3}$$

where the approximation in (4.3) is accurate only in the first order. To increase the accuracy of the differentiation scheme, we may include terms further away from the point of evaluation (i.e. f_{n+2}). In 2D space is sampled at regular intervals in both dimensions as shown in Fig. 4.2. In the simulations we used the following differential schemes:

$$\begin{aligned} \nabla^2 f_{i,j} &= \begin{bmatrix} 1/4 & 1/2 & 1/4 \\ 1/2 & -3 & 1/2 \\ 1/4 & 1/2 & 1/4 \end{bmatrix} \frac{f_{i,j}}{\Delta x^2} \\ \frac{\partial}{\partial x} f_{i,j} &= \begin{bmatrix} 0 & 0 & 0 \\ -1 & 0 & +1 \\ 0 & 0 & 0 \end{bmatrix} \frac{f_{i,j}}{\Delta x} \\ \frac{\partial}{\partial y} f_{i,j} &= \begin{bmatrix} 0 & +1 & 0 \\ 0 & 0 & 0 \\ 0 & -1 & 0 \end{bmatrix} \frac{f_{i,j}}{\Delta x} \end{aligned} \tag{4.4}$$

where the schemes should be interpreted as multiplication with corresponding relative indexes of $f_{i,j}$

$$\mathbf{M} f_{i,j} = \sum_{\Delta i=-1}^{+1} \sum_{\Delta j=-1}^{+1} M_{2+\Delta i, 2+\Delta j} f_{i+\Delta i, j+\Delta j} \tag{4.5}$$

In the simulations we used first order differential schemes that require only the nearest neighbours for evaluation, as this proved less error prone to implement on an adaptive mesh. We only used the stencils above, therefore to evaluate operator $\mathcal{L}_j A_j$ we had to proceed in three steps and store the intermediate results in auxiliary variables

$$\begin{aligned} \{\nabla^2 + 2i\mathbf{k}_j \cdot \nabla\} A_j &\Rightarrow (-r - 3\overline{\psi}^2 - \{\nabla^2 + 2i\mathbf{k}_j \cdot \nabla\}^2) A_j \\ &\Rightarrow (1 - \nabla^2 - 2i\mathbf{k}_j \cdot \nabla)(-r - 3\overline{\psi}^2 - \{\nabla^2 + 2i\mathbf{k}_j \cdot \nabla\}^2) A_j \\ &= \mathcal{L}_j A_j \end{aligned} \tag{4.6}$$

We then solved the evolution equations for A_j numerically using an explicit iteration scheme

$$A_{j,t+1} = A_{j,t} + \frac{\partial A_{j,t}}{\partial t} \tag{4.7}$$

4.3 Adaptive mesh refinement

The main benefit of the AMR algorithms is their ability to put more computational points into the parts of the simulated domain where interesting things happen, and by doing this effectively dedicate computational power to computing interesting things. The AMR solver we used in the simulation is the work of Greenwood and a detailed description of the implementation is provided in [29]. Here only a brief summary will be given.

In the case of computational materials science on the level where we want to study defects in crystal lattices, what is interesting is the defects in crystal lattices, and therefore we want more computational points around topological defects, on grain boundaries and on the solidification front. This is achieved is by splitting the computational nodes in half (in 4 parts 2D, 8 parts in 3D) until the maximal change of any of the complex

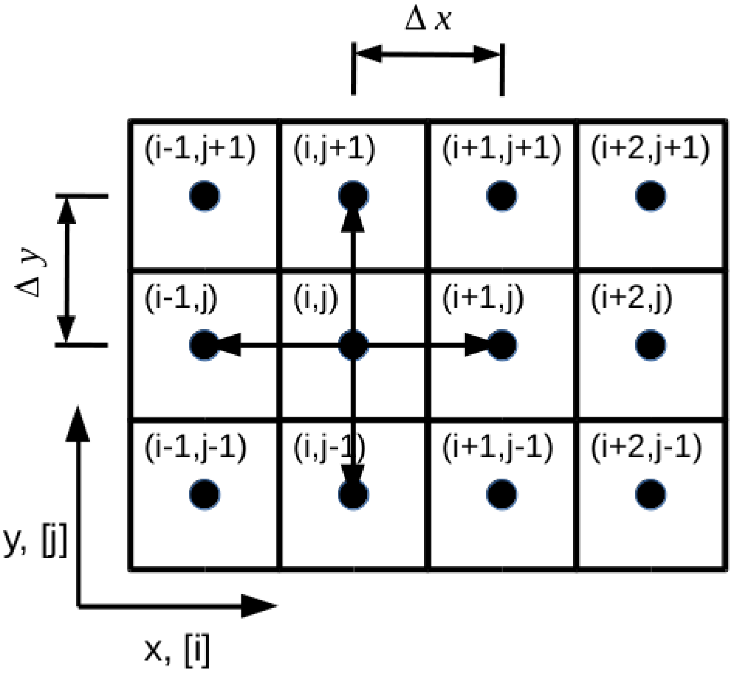

Figure 4.2: Discretisation of space with a regularly spaced grid of points. The continuous function $f(\mathbf{r})$ is represented by the values it takes on a regularly spaced grid of points $\mathbf{r}_{i,j} = \hat{e}_x i + \hat{e}_y j$. The derivatives are calculated using the stencils in eq. (4.4), the arrows at (i, j) connect the computation points that are needed to evaluate $\partial f_{i,j}/\partial x$ and $\partial f_{i,j}/\partial y$.

amplitudes A_j over one node reaches some pre-defined constant value. This effectively refines the mesh in areas where the complex amplitudes A_j change more rapidly. Care must be taken not to choose the refinement criteria too loosely, as the mesh refinement is done only every few steps of the calculation and in case the refinement criteria would be too loose, a moving solidification front or grain boundary could fall out of the area where the mesh is appropriately refined.

In order to be able to solve PDEs on an adaptive mesh, we need to know how to connect computational elements on various levels of refinement. Figure 4.3 presents and example of an adaptive mesh. The dots in the mesh represent computational points, and the squares and circles represent the computational nodes. In order to be able to connect the values on different levels of refinement, we need to add a layer of ghost nodes between the computational nodes. Computational nodes are the nodes in which the evolution of the fields is calculated (i.e. using eq. (4.7)), and the ghost nodes are the nodes in the mesh that connect the computational nodes at different levels of

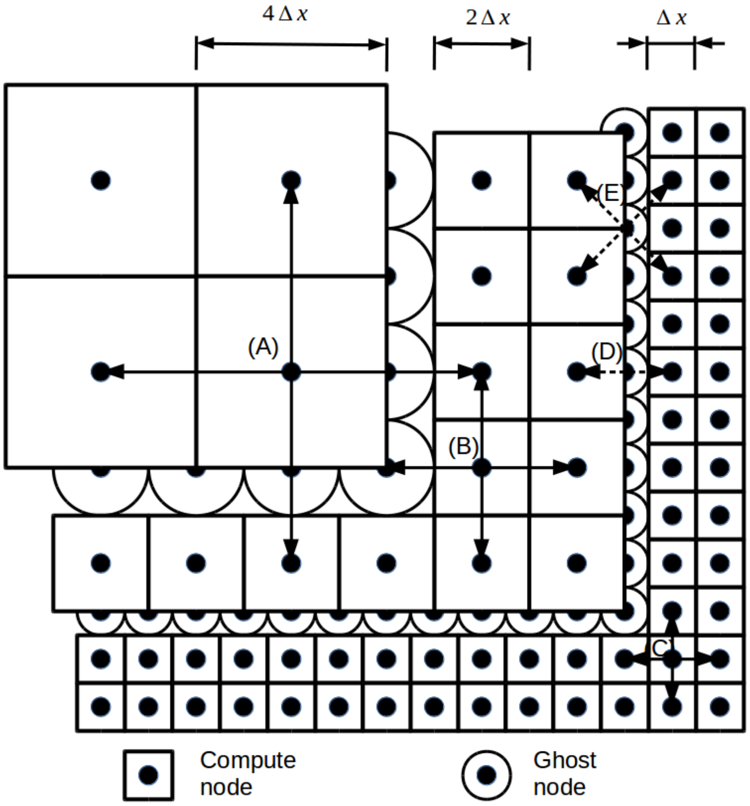

Figure 4.3: Adaptive mesh. The arrows at marked points connect the mesh nodes that are needed to evaluate simple stencils at given points. Marked points represent computation nodes (A) with some neighbours at a lower refinement level, (B) with a ghost neighbour at the same level of refinement, (C) with only computation node neighbours at the same level of refinement and ghost nodes (D) and (E) where the arrows point to the neighbours that are averaged in the ghost nodes.

refinement. While the values of the fields are continuously updated using an iterative scheme in the computational nodes, the values in the ghost nodes are at each step of the calculation derived by averaging the field values in neighbouring computational nodes.

In Fig. 4.3 we can see an adaptive mesh on three different levels of refinement (Δx, $2\Delta x$ and $4\Delta x$). The computation on this mesh in computational nodes is performed using the same stencils as we would use on a regular grid. In points marked as (A), (B) and (C) in Fig. 4.3, the values for derivatives are calculated using the stencils listed in (4.4). There is no difference between values obtained from nodes on different levels of refinement (case (A)), values obtained from ghost nodes (case (B)) and values obtained from computational nodes on the same level of refinement (case (C)). The update of values in ghost nodes is made by averaging the neighbouring computational nodes as shown in points (D) and (E). As we are using stencils that require only immediate neighbours, we need only one layer of ghost nodes in the mesh. In case we would want to use more sophisticated stencils, we would need to add more ghost nodes to the mesh (the number of layers of ghost nodes should be the same or higher than the number of nearest neighbours used in the stencils).

When using the algorithms described in this thesis, special care must be taken in how values from one node are treated in the other node with regard to the changes in local rotation, see description of our improvements in Chapter 5 for details. The main changes from the ordinary PF use of the AMR algorithm are that the values of the complex amplitudes A_j are always converted into a system aligned with the central node before use. When averaging for calculation of values in the ghost nodes, averaging is done while taking into account the changes in local rotation between the nodes.

Chapter 5

Adaptive Mesh Refinement in APFC Model

This chapter introduces improvements to an amplitude expansion of the phase field crystal model (APFC). An auxiliary field describing local grain rotation is introduced and used to enable the adaptive mesh to be coarsened in all grains, regardless of their orientation. Only a Cartesian representation of the amplitude equations is used. Copyright of this chapter is held by © *American Physical Society* [1].

5.1 Introduction

Many industrially important problems relate to the ability to understand and predict the microstructure evolution during thermomechanical processing of polycrystalline materials. In field of metallic materials, these include the processes of solidification, solid state phase transformations, recrystallization, grain growth, nucleation and growth/dissolution of precipitates, etc. Predicting the microstructure's evolution generally requires accurate models to describe processes simultaneously occurring at various spatial and temporal scales, ranging from atomistic to mesoscopic and macroscopic and from atomic vibrations to diffusive times. Despite modern computational resources, even today these large variations in time and length scales in material modeling represent a huge research challenge. In past decades, several approaches were developed to study microstructure's

---

[1] Reprinted with permission from Berčič and Kugler, Physical Review E 98, 033303 (2018). Copyright (2019) by the © *American Physical Society.* DOI: http://dx.doi.org/10.1103/PhysRevE.98.033303.

evolution at various length scales, i.e. molecular dynamics and kinetic Monte Carlo on the atomistic scale, the cellular automata, Potts-Monte-Carlo and phase field (PF) methods on the mesoscopic scale, and continuum-based methods on the macroscopic scale [68]. To establish a way to bridge these models addressing phenomena at various scales, a range of approaches has been proposed [2, 69]. In recent years, the materials engineering field has seen the increasingly popular concept of integrated computational materials engineering (ICME) which links material models at multiple scales hierarchically [3]. While approaches like ICME may be of great practical value by associating material models at different scales with processing technologies and product design, they may be associated with difficulties of discontinuous transitions between scales that can lead to nonphysical phenomena. In contrast, the PF method in combination with adaptive mesh refinement was used to study the microstructure evolution on spatial scales spanning several orders of magnitude [4, 70]. Its success lies in expressing the boundary conditions on the solid-liquid interface with a partial differential equation for the evolution of a phase field variable. As the evolved phase field is a continuous function of space, the method is not well suited for modeling phenomena occurring on an atomistic scale, as it is averaged out in the phase field variable. To describe the atomic arrangement, the phase-field-crystal (PFC) methodology was introduced [5, 6]. The PFC model is a reformulation of the Swift-Hohenberg model [10] and can be derived from classical density-functional theory under some necessary assumptions[11]. The method uses a crystal density field to describe the dynamics of atomic structures. It incorporates elasticity and various topological defects in a natural way. Since the PFC method was initially developed, it has been improved in multiple ways, enabling it to be applied to even more problems. PFC models have been extended to describe materials with different crystal lattices using a 2-mode PFC model [12], model structural transformations in materials using a constructed 2-particle correlation function (XPFC model) [14, 15] and extend this approach to stabilize several phases with a 3-particle correlation function [16, 17], incorporate acoustic waves [20] and spatial anisotropy [21], describe liquid crystals [22, 23] and model phenomena occurring in ferromagnetic [24] and ferroelectric multi-component materials [25].

One important PFC model improvement that is increasing in popularity is the complex-amplitude expansion (APFC) developed by Goldenfeld *et al.* [7, 8]. The method uses a renormalization group based approach to express the atomic density function as a sum of waves, aligned with the reciprocal lattice vectors, and derives the evolution equations for the amplitudes. This approach offers the possibility to bridge the gap between the PFC method and PF methods. Such improvements greatly increase the size of the modeled material and, combined with other APFC method properties, offer the ability to study many phenomena in which larger volumes of material must be modeled at diffusive timescales. This extension has been successfully applied to the study of grain boundary motion and polycrystalline films [7, 8, 38], structural phase transitions [48], heteroepitaxial ordering of thin films [44–47] and grain boundary energies [51, 55]. The method was initially developed for single-component systems with triangular symmetry in 2D and since then has been extended to binary systems [10, 49, 50], honeycomb [46, 51] and square [48] lattices in 2D, and fcc and bcc systems [49, 52] in 3D. The APFC extension was also improved to obtain an instantaneous mechanical equilibrium [53], tune the energy of defects and interfaces [55], and couple the microstructure forming fields to the hydrodynamic velocity field [54].

To further increase the size of the simulated domain, adaptive mesh refinement (AMR) algorithms can be applied to APFC models, as demonstrated by Athreya *et al.* [9]. Despite the AMR APFC model's initial soccess, some unresolved issues are preventing its further development [10]. Consequently, most of APFC models still use simple numerical methods on a fixed grid [10, 38, 44–54]. Therefore, the main purpose of the present work is to propose a new way for solving problems related to grain rotation in APFC models. The presented model does not require the use of separate phase and amplitude equations like in Athreya *et al.* [9]. Instead, an auxiliary local rotation field is calculated and used to align the basis vectors with the rotation of grains at all calculation points.

This contribution is organized as follows. In Sec. 5.2, the main features of the PFC model and complex amplitude equations used in the present work are recapitulated. Section 5.3 contains a description of the new model, algorithm, and primary features of the numerical approach used. In Sec. 5.4, simulations results are presented and, finally, concluding remarks are given in Sec. 5.5.

5.2 APFC model

Evolution of the density field in the PFC model is given by [5]:

$$\frac{\partial \rho}{\partial t} = \Gamma \nabla^2 \left(\frac{\delta \mathcal{F}}{\delta \rho} \right) \tag{5.1}$$

where $\mathcal{F}$ is the free energy functional dependent on local free energy density $f(\rho, \nabla^2\rho)$, Γ is a constant and η is stochastic noise with zero mean and correlations $\langle\eta(\boldsymbol{r},t)\eta(\boldsymbol{r'},t')\rangle = -\Gamma k_B T\nabla^2\delta(\boldsymbol{r}-\boldsymbol{r'})\delta(t-t')$. The chosen free energy functional is minimized by a spatially uniform liquid state at high temperatures and by a spatially periodic "crystalline" phase at low temperatures [5]. A solution with the required form will naturally exhibit the properties observed in the crystals, such as the correct properties of elastic energy, defects in the crystalline phase, proper grain boundary energy, epitaxial growth, yield strength of nanocrystalline materials and proper behavior of misfit dislocations as already shown by Elder *et al.* [5, 6].

The exact form of the functional used is

$$f = \rho\left[\alpha\Delta T + \lambda(q_0^2+\nabla^2)^2\right]\rho/2 + u\rho^4/4 \tag{5.2}$$

where α, λ, q_0 and u are model parameters that can be used to match the properties of a chosen material. The model's behavior can be better understood by first rewriting the free energy in dimensionless units using $\boldsymbol{x} = \boldsymbol{r}q_0$, $\psi = \rho\sqrt{u/\lambda q_0^4}$, $r = a\Delta T/\lambda q_0^4$, $\tau = \Gamma\lambda q_0^6 t$ and $F = \mathcal{F}u/\lambda^2 q_0^{8-d}$ into

$$F = \int d\boldsymbol{x}\{\psi[r + (1+\nabla^2)^2]\psi/2 + \psi^4/4\} \tag{5.3}$$

Conversion of the dynamic Eq. (5.1) yields

$$\frac{\partial\psi}{\partial t} = \nabla^2\{[r + (1+\nabla^2)^2]\psi + \psi^3\} + \zeta \tag{5.4}$$

where $\langle\zeta(\boldsymbol{r},\tau)\zeta(\boldsymbol{r'},\tau')\rangle = \varepsilon\nabla^2\delta(\boldsymbol{r}-\boldsymbol{r'})\delta(\tau-\tau')$ and $\varepsilon = uk_bTq_0^{d-4}/\lambda^2$. The equation (5.4) was introduced by Elder *et al.* [5, 6] and since then has frequently been referred to as the PFC equation. The single mode solution of the PFC equation in the solid phase has triangular symmetry and can be approximated in terms of the complex amplitudes A_j [7–9] as

$$\psi \approx \sum_{j=1}^{3} A_j e^{i\mathbf{k_j}\cdot\mathbf{x}} + \sum_{j=1}^{3} A_j^* e^{-i\mathbf{k_j}\cdot\mathbf{x}} + \overline{\psi} \tag{5.5}$$

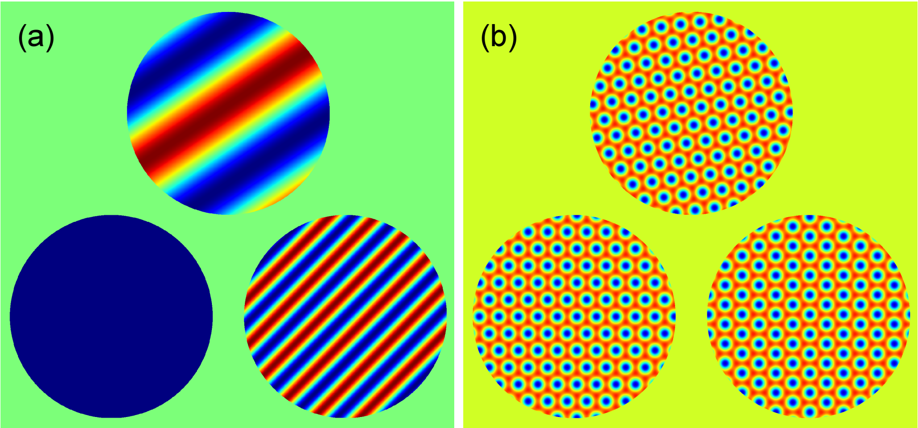

Figure 5.1: Beats in misaligned grains. The images show (a) real component of the first complex amplitude $\Re(A_1)$, and (b) the reconstructed atomic density field ψ in three seeds, rotated for (clockwise from bottom left) $\theta = 0$, $\pi/24$ and $\pi/6$.

where k_j are the reciprocal lattice vectors of a hexagonal crystal

$$\begin{aligned} \mathbf{k}_1 &= k_0(-\boldsymbol{i}\sqrt{3}/2 - \boldsymbol{j}/2), \\ \mathbf{k}_2 &= k_0\boldsymbol{j}, \\ \mathbf{k}_3 &= k_0(\boldsymbol{i}\sqrt{3}/2 - \boldsymbol{j}/2), \end{aligned} \tag{5.6}$$

and k_0 the wave number set to $k_0 = 1$ in the present work. This wave number corresponds to the atomic spacing of $a_0 = 2\pi/(\sqrt{3}/2)$. Dynamic equations for the coarse grained complex amplitudes have been derived by Goldenfeld *et al.* [7, 8]:

$$\frac{\partial A_j}{\partial t} = \tilde{\mathcal{L}}_j A_j - 3A_j|A_j|^2 - 6A_j \sum_{k:k\neq j} |A_k|^2 - 6\overline{\psi} \prod_{k:k\neq j} A_k^* \tag{5.7}$$

where $k, j \in [1, 3]$ and

$$\tilde{\mathcal{L}}_j = (1 - \nabla^2 - 2i\mathbf{k}_j \cdot \nabla)(-r - 3\overline{\psi}^2 - \{\nabla^2 + 2i\mathbf{k}_j \cdot \nabla\}^2) \tag{5.8}$$

is a rotationally covariant operator. The parameters $\overline{\psi}$ and r are the dimensionless average density and the dimensionless temperature proportional to the temperature difference to a critical temperature T_c. Due to rotational covariance of the operator $\tilde{\mathcal{L}}_j$, multiple orientations of the crystal grains can be modeled using only the set of basis vectors listed in (5.6).

Grain rotation in the complex amplitudes equations (5.7) is represented by the so called beats in the amplitudes of grains, not aligned with the initial choice of basis vectors [7, 9], as shown in Fig. 5.1. This makes adaptive mesh refinement techniques ineffective in solving the problem, as the mesh does not coarsen in misaligned grains due to the fast changing amplitudes caused by the beats. To tackle this problem, an improved approach using polar representation of the complex amplitudes equations in combination with the existing representation was introduced by Athreya *et al.* [9]. The complex amplitudes were split into phase and amplitude as $A_j = \Psi_j e^{i\Phi_j}$ and both, phase Φ and amplitude Ψ were evolved separately. The phase is computed as $\Phi = \arctan(\Im(A_j)/\Re(A_j))$ making phase Φ a locally discontinuous function, leading to calculation problems. To resolve problems with discontinuities, the simulation domain was divided into two subdomains: a liquid region, where the ordinary dynamic equations (5.7) were evolved, and a solidified region, where the new phase/amplitude equations were used. Within the solidified region an approximation of a frozen phase gradient was applied, which eliminated problems with the discontinuities of the phase gradient. As the conversion between representations is simple, the resulting computational scheme is efficient and produces significant speedups of the simulations originating from the added ability to coarsen the adaptive mesh within all grains, regardless of their orientation. The new approximations used in the framework allow the efficient use of the computational resources, although some problems still remain. In particular, the problem of a hidden grain boundary between grains rotated by a multiple of the crystal's symmetry, as reported by Spatschek and Karma [10], is not easy to solve. Therefore, other approaches are needed to study the grain behavior under full grain rotation conditions. A possible approach is proposed in the following section.

5.3 Description of the new model

5.3.1 Local rotation of the basis vectors

The new model exploits the fact that beats of complex amplitudes in solidified grains disappear, when the basis vectors for the amplitudes are correctly rotated. A local rotation field is introduced, and dynamic equations of the coarse grained complex amplitudes (5.7) are solved by taking into account the spatially dependent rotation of the basis vectors k_j.

Density function of a grain rotated by ϑ with regard to the basis vectors can be written as [9]:

$$\psi(\vartheta) = \sum_{j=1}^{3} A_j^{\vartheta} e^{i\mathbf{k}_j(\vartheta)\cdot\mathbf{x}} \quad +CC \quad +\overline{\psi} \tag{5.9}$$

$$= \sum_{j=1}^{3} A_j^{\vartheta} e^{i\delta\mathbf{k_j}(\vartheta)} e^{i\mathbf{k}_j\cdot\mathbf{x}} \quad +CC \quad +\overline{\psi} \tag{5.10}$$

$$= \sum_{j=1}^{3} A_j e^{i\mathbf{k}_j\cdot\mathbf{x}} \quad +CC \quad +\overline{\psi} \tag{5.11}$$

where $\mathbf{k}_j(\vartheta) = \mathbf{k}_j + \delta\mathbf{k}_j(\vartheta)$ are rotated basis vectors and CC denotes the complex conjugate of the first sum. We derive the connection between the rotated amplitudes A_j^{ϑ} and non-rotated amplitudes A_j by comparing the terms associated with the same wave vectors and obtain

$$A_j = A_j^{\vartheta} e^{i\delta\mathbf{k}_j(\vartheta)\cdot\mathbf{x}} \tag{5.12}$$

It follows that grains with arbitrary rotations can be described in terms of $\mathbf{k}_j$, with grain rotation resulting in beats of the amplitudes.

As the rotated amplitudes within a perfect, rotated grain remain constant, the gradient of the rotated amplitudes inside is zero:

$$\nabla A_j^{\vartheta} = (\nabla A_j)e^{-i\delta\mathbf{k}_j\cdot\mathbf{x}} + A_j(-i\delta\mathbf{k}_j)e^{-i\delta\mathbf{k}_j\cdot\mathbf{x}} = 0 \tag{5.13}$$

From (5.13) it follows that for a local rotation, at which beats disappear, the following must hold for the rotated basis vectors:

$$\delta\mathbf{k}_j(\vartheta) = \frac{\nabla A_j}{iA_j} = \mathbf{k}_j(\vartheta) - \mathbf{k}_j \tag{5.14}$$

In simulations we know the amplitudes A_j, but not the local grain rotation. From (5.14) we can derive the local rotation of the grain in which the beats disappear.

Due to rotational covariance of the operator $\tilde{\mathcal{L}}_j$ and all of its parts used in the calculation, it follows that conversion between basis vectors rotated by a different amount can be separated from the operator evaluation. The operator defined as

$$\Box^{\vartheta} = (\nabla^2 + 2i\mathbf{k}_j(\vartheta)\cdot\nabla) \tag{5.15}$$

is rotationally covariant and therefore the following must hold

$$\Box^{\vartheta} A_j^{\vartheta} = e^{-i\delta \mathbf{k_j}\cdot\mathbf{x}} \Box A_j \tag{5.16}$$

where $\Box = \Box^{\vartheta=0}$. Further, if we separate operator $\tilde{\mathcal{L}}_j$ into two operators that can each be evaluated in a single step with a simple differential schema

$$\tilde{\mathcal{L}}_{1j}^{\vartheta} = \left(-r - 3\overline{\psi}^2 - \left(\Box^{\vartheta}\right)^2\right) \tag{5.17}$$

$$\tilde{\mathcal{L}}_{2j}^{\vartheta} = (1 - \Box^{\vartheta}) \tag{5.18}$$

$$\tilde{\mathcal{L}}_{j}^{\vartheta} = \tilde{\mathcal{L}}_{2j}^{\vartheta} \tilde{\mathcal{L}}_{1j}^{\vartheta} \tag{5.19}$$

then both $\tilde{\mathcal{L}}_{1j}$ and $\tilde{\mathcal{L}}_{2j}$ are rotationally covariant. This allows us to apply dynamic evolution equation even when the rotation of the basis vectors is spatially dependent.

We can numerically apply an operator $\tilde{\mathcal{O}}^{\vartheta}$ to a locally rotated field X

$$\tilde{\mathcal{O}}^{\vartheta(\mathbf{x})}\ X^{\vartheta(\mathbf{x})}(\mathbf{x}) = \sum_{\tilde{\mathbf{x}}} \Gamma_{\tilde{\mathbf{x}}} e^{-i(\mathbf{k}(\mathbf{x})-\mathbf{k}(\tilde{\mathbf{x}}))\cdot\tilde{\mathbf{x}}} X^{\vartheta(\tilde{\mathbf{x}})}(\tilde{\mathbf{x}}) \tag{5.20}$$

where the summation goes over all neighbors included in the operator's evaluation. $\tilde{\mathcal{O}}$ can be any of the rotationally covariant operators ($\tilde{\mathcal{O}} \in \{\tilde{\mathcal{L}}_j^{\vartheta}, \tilde{\mathcal{L}}_{1j}^{\vartheta}, \tilde{\mathcal{L}}_{2j}^{\vartheta}\}$) applied to any of the derived fields ($X \in \{A_j^{\vartheta}, \tilde{\mathcal{L}}_{1j} A_j^{\vartheta}, \tilde{\mathcal{L}}_j A_j^{\vartheta}\}$). $\tilde{\mathbf{x}}$ is the location of the neighbor matching the operator kernel element $\Gamma_{\tilde{\mathbf{x}}}$. To convert between local rotations at $\mathbf{x}$ and $\tilde{\mathbf{x}}$, we need to multiply $X^{\vartheta(\tilde{\mathbf{x}})}(\tilde{\mathbf{x}})$ with a rotation conversion factor $e^{-i(\mathbf{k}(\mathbf{x})-\mathbf{k}(\tilde{\mathbf{x}}))\cdot\tilde{\mathbf{x}}}$, which needs to be stored alongside the values of $X^{\vartheta(\mathbf{x})}(\mathbf{x})$.

5.3.2 Algorithm description

When considering the evolution of the complex amplitudes in a system where the basis vectors for the amplitudes vary with location, one must take into account differences in rotation when applying the dynamic equations.

Since all the fields needed in intermediate steps of the calculation are rotationally covariant, this does not pose a problem apart from an additional multiplication step and the necessity of maintaining the rotational constants stored in the computational nodes.

The calculation works in the same way as if all neighbor nodes of the current calculation node were temporarily converted in the same rotated system as the central node. When all basis vectors are the same, the normal evolution Eq. (5.7) can be applied.

Algorithm 1 Top level algorithm for evolution of complex amplitudes.

```
loop
    if $step$ mod $adaptation = 0$ then
        Do mesh refinement
        Calculate local rotation
        Calculate rotation conversion factors
    end if
    Perform evolution iteration
end loop
```

Algorithm 2 Local rotation adjustment. Parameters p, q, $A_{minamp.}$ and $\vartheta_{max.phase}$ are heuristic.

```
for each computation node do
    Find optimal rotation $\vartheta_{\mathrm{opt}}$:
    if $|A_j^{\vartheta}| > A_{\mathrm{min\ amp.}}$ then
        In solidified regions: from gradient
        for all $j \in \{1, 2, 3\}$ do
            $\delta\mathbf{k}_j(\vartheta_{\mathrm{current}}) = \Re\left(\frac{\nabla A_j^{\vartheta_{\mathrm{current}}}}{i A_j^{\vartheta_{\mathrm{current}}}}\right)$
            $\vartheta_{x,j} = 1 + \mathbf{k}_j(\vartheta_{\mathrm{current}}) \cdot \delta\mathbf{k}_j$
            $\vartheta_{y,j} = (\mathbf{k}_j(\vartheta_{\mathrm{current}}) \times \delta\mathbf{k}_j) \cdot \hat{\mathbf{e}}_z$
        end for
        $\vartheta_{\mathrm{opt}} = \vartheta_{\mathrm{current}} + atan2(\sum_j \vartheta_{y,j}/3, \sum_j \vartheta_{x,j}/3)$
    else
        In liquid regions: drop towards zero
        $\vartheta_{\mathrm{opt}} = 0$
    end if
    Smooth the changes
    $\vartheta_{\mathrm{new}} = p \times \vartheta_{\mathrm{current}} + q \times \vartheta_{\mathrm{opt}}$
    Prevent skipping beats
    $d\vartheta = \max_{\{\mathrm{all\ neighbours\ NN}\}} |\vartheta_{NN} - \vartheta_{\mathrm{new}}|$ modulo $2\pi$
    $k_\vartheta = dx\ d\vartheta/\vartheta_{\mathrm{max.\ phase}}$
    if $k_\vartheta > 1$ then
        $\vartheta_{\mathrm{new}} = \vartheta_{\mathrm{current}} + (\vartheta_{\mathrm{new}} - \vartheta_{\mathrm{current}})/k_\vartheta$
    end if
    $\vartheta_{\mathrm{current}} = \vartheta_{\mathrm{new}}$
end for
```

Averaging over nodes, either when calculating ghost node values or when calculating values on the newly created nodes during mesh adaptation is carried out using Eq. (5.20). As changes in a local rotation affect the averaging of the fields, a small change in a local rotation is an additional criterion for mesh coarsening. The mesh adaptation algorithm therefore coarsens the mesh only where the change in a local rotation and all fields are sufficiently small.

The local rotation is calculated from the gradient of the complex amplitudes, and gradients change rapidly on the solid liquid interface and in the vicinity of dislocations. To prevent large changes in a local rotation, which could result in skipped beats, an additional averaging step to remove high frequency changes is performed before the rotation angle update. The pseudocode of the implementation is shown in algorithms 1 and 2.

Since the new model employs local orientations of the basis vectors, and the original model is rotationally covariant, the properties of both models are equivalent under the assumptions of the complex amplitudes model given with Eq. (5.7).

An explicit iteration scheme was used in the implementation. Each complex amplitude is evolved using Eq. (5.7) on an adaptive grid. In all the calculations presented in this work, the parameters were set to match those used by Athreya in [9]; i.e. $r = -0.25$, $\overline{\psi} = 0.285$ with time step set to $\Delta t = 0.04$ and minimal grid spacing $\delta x_{min} = \pi/2$. In grid adaptation, the change of amplitudes over one node is limited by $|A_j^{\vartheta,\ulcorner} - A_j^{\vartheta,\urcorner}| + |A_j^{\vartheta,\urcorner} - A_j^{\vartheta,\lrcorner}| + |A_j^{\vartheta,\lrcorner} - A_j^{\vartheta,\llcorner}| + |A_j^{\vartheta,\llcorner} - A_j^{\vartheta,\ulcorner}| < AdaptThreshold = 0.02$ for each j, where the notation $^\ulcorner$ in $A_j^{\vartheta,\ulcorner}$ denotes the top left neighbor of the node. The maximal change is further limited by an additional criterion that the maximal change in a local rotation over one node must not exceed $max_{\Delta\vartheta} = \pi/16$.

An AMR Solver was used in all the simulations, based on the work of Greenwood. The solver's implementation is described in [9, 29, 71].

5.4 Results

Figure 5.2 shows evolution of the microstructure represented by the average amplitude field ($\sum_j |A_j|/3$), of an example problem in which 12 seeds with an initial radius of 8π and orientation angles in the range $[0, \pi/12)$ were placed inside a square domain of size 256π with a periodic boundary condition. The example problem was chosen to match the example configuration employed by Athreya *et al.* in [9] as closely as possible to allow the reader to make an easy comparison. Note that the grain rotations are different and thus the number of dislocations on different grain boundaries is not the same as in [9]. A visible example is the grain boundary on the bottom right part of the simulation domain where in our simulations dislocations do not appear due to a small difference in the rotations of the impinging grains.

By introducing a local rotation field in combination with exploitation of the rotational covariance of all steps in the calculation, we were able to solve the complex amplitudes equations on an adaptive grid, with coarsening in all grains, regardless of their orientation. This ensures the computational resources spent on calculations scale with the grain surface in the same manner as achieved by Athreya *et al.* [9]. In comparison, our approach does not require different representations of the complex amplitudes in different regions of the computational domain, which eliminates difficulties that could arise from application of two different evolution equations in separate regions of the simulation domain. However, compared to the basic APFC model described by Goldenfeld *et al.* [7, 8] this model requires additional multiplications and memory for the storage and application of the rotation factors.

The evolution of the microstructure shown in Fig. 5.2 shows the results obtained with the new algorithm closely match the results obtained with the previous approach. The positions of the dislocations and the resulting microstructure overall are the same, while the grid remains dense only on the solid-liquid interface and around the dislocations, where the field values change more rapidly.

A better insight into the new model's properties can be obtained by analyzing the results displayed in Fig. 5.3 where the impingement of two grains was simulated. The left grain is rotated by $\pi/12$ and therefore exhibits the amplitude beats in all amplitudes, whereas the right grain is aligned with the choice of basis vectors and shows no beats. This may be seen in the image (c) on the third row where the phase of the first complex amplitude $\Phi(A_1)$ is shown, indicating beats in the left grain and no beats in the right grain. The newly introduced locally-rotated complex amplitude A_1^{ϑ} is shown on the second row (b) of the image, where we can see that no beats are exhibited in the interior of either grain, where the new algorithm is able to align the orientation of the basis vectors with the rotated grain on the left and remove all the beats. It can be observed that when using a local rotation the mesh coarsens inside both grains, regardless of their orientation, and remains dense on the boundary between the grains.

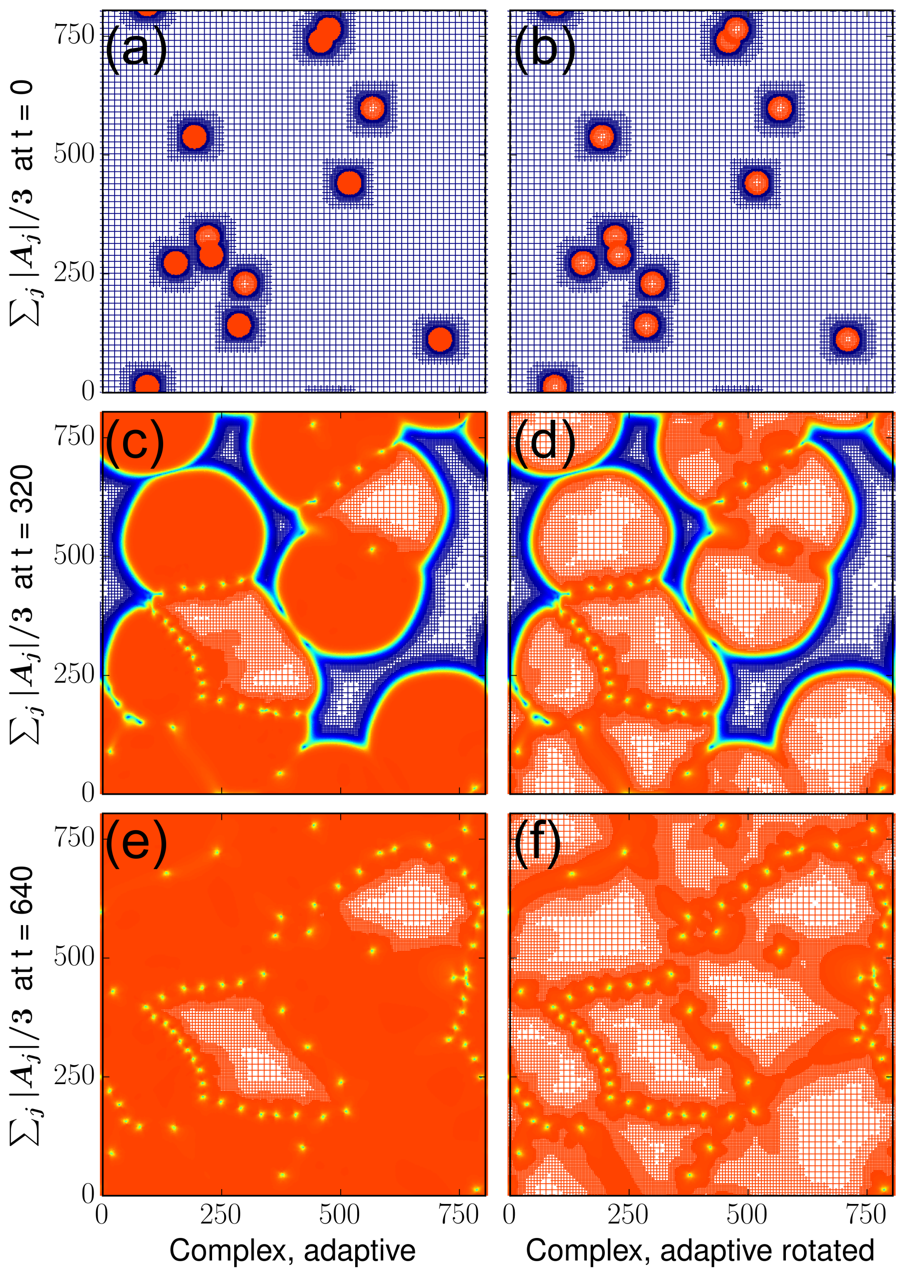

Figure 5.2: Microstructure evolution in time. Comparison of the AMR model with and without local rotation. When using a local rotation, the mesh coarsens in all seeds, regardless of their orientation, and remains dense on grain boundaries where dislocations are formed. Images show the average amplitude field ($\sum_j |A_j|/3$) at different times.

In order to more clearly demonstrate how our model behaves, we simulated the growth of 12 grains placed in an undercooled melt in different locations. As may be

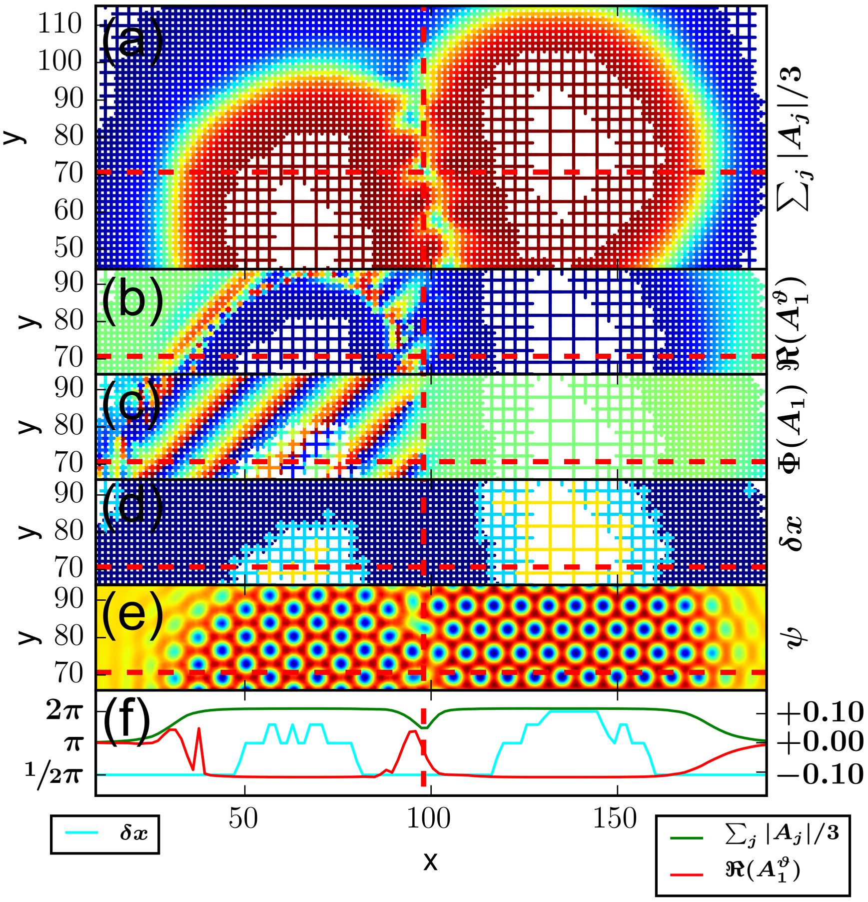

Figure 5.3: Beats and mesh refinement in rotated and non-rotated grains. The grains are rotated by $\theta = \pi/12$ and 0. From top to bottom the image shows (a) the average absolute amplitude ($\sum_j |A_j|/3$), (b) the real part of locally-rotated complex amplitude ($\Re(A_1^\vartheta)$), (c) the phase angle of the complex amplitude A_1 ($\Phi(A_1)$), (d) local mesh refinement (δx), (e) reconstructed atomic density function (ψ) and (f) the fields δx, $\sum_j |A_j|/3$ in cross-section.

seen in Fig. 5.4, the results obtained using the new model are in excellent agreement with the results obtained without local rotation and with results obtained on a regular grid. The comparison shows that the new model successfully reproduces the microstructure with grid coarsening in all grains. Figure 5.4 shows a snapshot of the microstructure's evolution at $t = 360$. Results obtained with different models are placed in consecutive columns of Fig. 5.4: the first column shows the APFC model on a uniform grid, the second column the APFC model on an adaptive grid, while the third column shows the new model. Images in the rows display the following fields: (a-c) reconstructed atomic

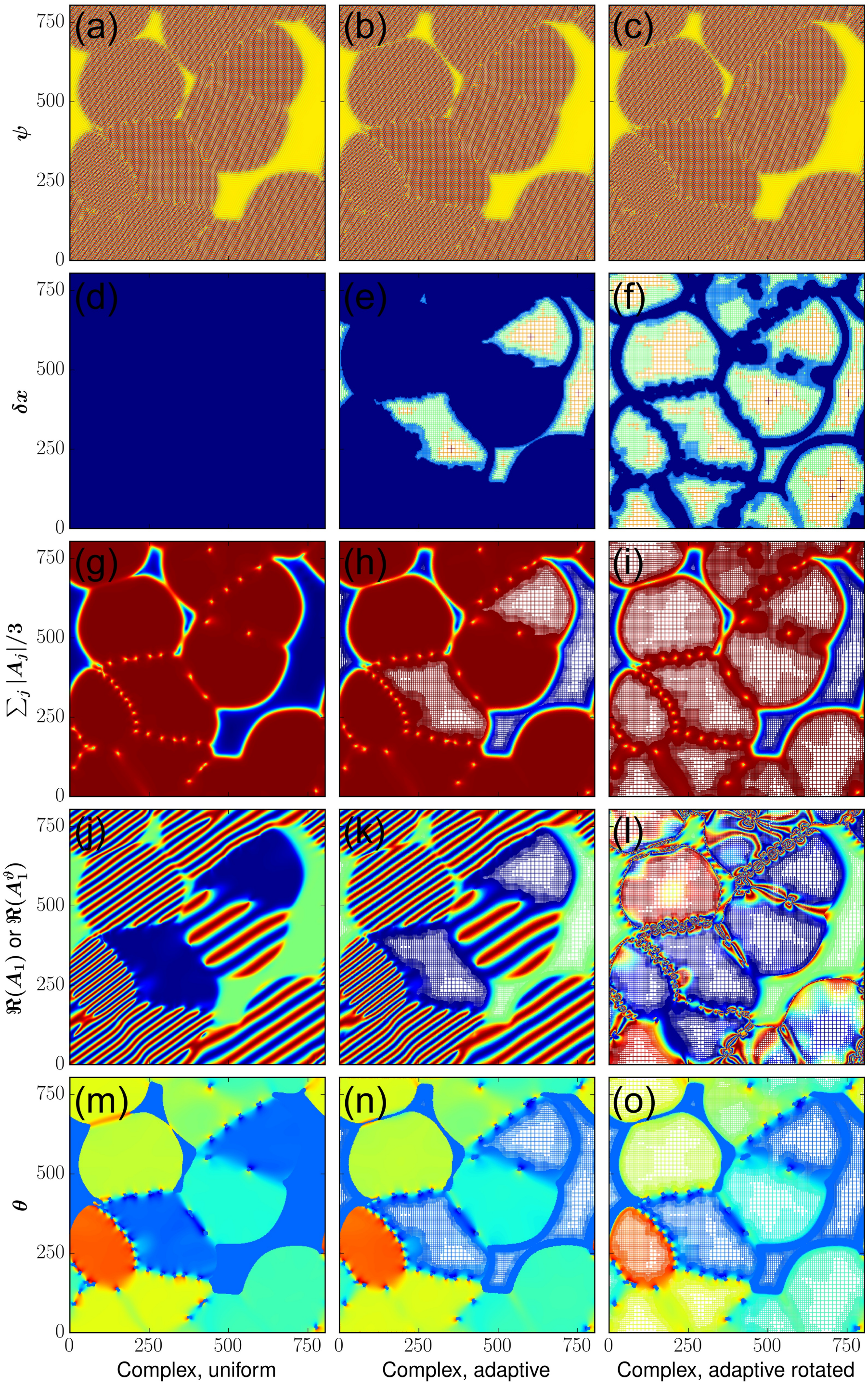

Figure 5.4: Comparison of simulation results with different models at $t = 360$. All columns show PFC model with Complex Amplitudes extension. The first column shows results when using a regular grid, the second column shows results when using Adaptive Mesh Refinement techniques and the third column shows results when using local rotation with the help of an auxiliary rotation field. From top to bottom: reconstructed atomic density field ψ, mesh density δx, average amplitude $\sum_j |A_j|/3$, real part of the first complex amplitude $\Re(A_1)$ and local grain rotation in degrees θ are shown.

density field ψ, (d-f) mesh density δx, (g-i) average amplitude $\sum_j |A_j|/3$, (j-l) real part of the first complex amplitude $\Re(A_1)$ and (m-o) local grain rotation θ in degrees. The reconstructed atomic density field ψ shown in the first row (a-c) is virtually the same in all models used. In the images showing mesh density δx in the second row (d-f) we can see that when applying AMR techniques to the APFC model the mesh coarsens only in liquid regions and non-rotated grains, whereas when using our new approach the mesh coarsens in all grains, and dense mesh remains only around the dislocations and at the solid-liquid interface. Average amplitude $\sum_j |A_j|/3$ presented in the third row (g-i) shows the same grain growth and locations of dislocations are obtained with all three models. The fourth row presents the real component of the first complex amplitude $\Re(A_1)$ in the columns corresponding to APFC models without a local rotation (j-k). We can observe the beats occurring in rotated grains that prevent the mesh from coarsening. As our model uses a locally-rotated complex amplitude field A_j^ϑ instead of A_j, the real part of this field is shown in the last column (l). We can see that the local rotation eliminates beats in all grains and enables efficient mesh coarsening. The last row shows local grain rotation. Images corresponding to APFC models (m-n) show a local rotation field obtained in post-processing, which is not used during calculations and is displayed here only for comparison. The final image in the last row (o) shows the local rotation field θ as used during the calculations in our model. We can observe that the density of dislocations on the boundary between grains corresponds to the difference in the rotation of the grains. When rotations of two grains differ only slightly, no dislocations form on the boundary. In the bottom left part of the simulation domain we placed two seeds with the same orientation, but shifted the lattice of one seed by approximately half of the lattice spacing with regard to the second seed. On the boundary between these two grains we can therefore find no dislocations since the orientation is the same. However, because the atomic lattice is shifted in one grain with regard to the other, the mesh still does not coarsen completely as some elastic deformations remain in the atomic lattice and variations in amplitudes due to the elastic deformations requiring higher mesh refinement. We can also observe that shifting the atomic lattice changes the phase of both locally rotated amplitudes A_j^ϑ and A_j. As the phase changes continuously, no defects appear on this boundary.

Selected fields in the cross section of the same simulation are shown in Fig. 5.5, where the changes in local rotation field θ across the grain boundaries can be better tracked. Rapid changes can be observed where the cross-section cut approaches the dislocation ($x \approx 200$) and the local rotation rapidly switches between rotations of both interfacing grains. A more gradual change in local rotation is observed on the interfaces between grains which differ in rotation by a smaller amount ($x \approx 480$ and $x \approx 650$), where the cut line does not pass directly through a dislocation. We can see that the mesh is refined only on the grain boundaries and remains refined even on the boundary between grains which vary only slightly in their orientations and dislocations do not appear ($x \approx 480$). This is needed due to the elastic deformations that appear there to accommodate the deformation of the crystal lattice.

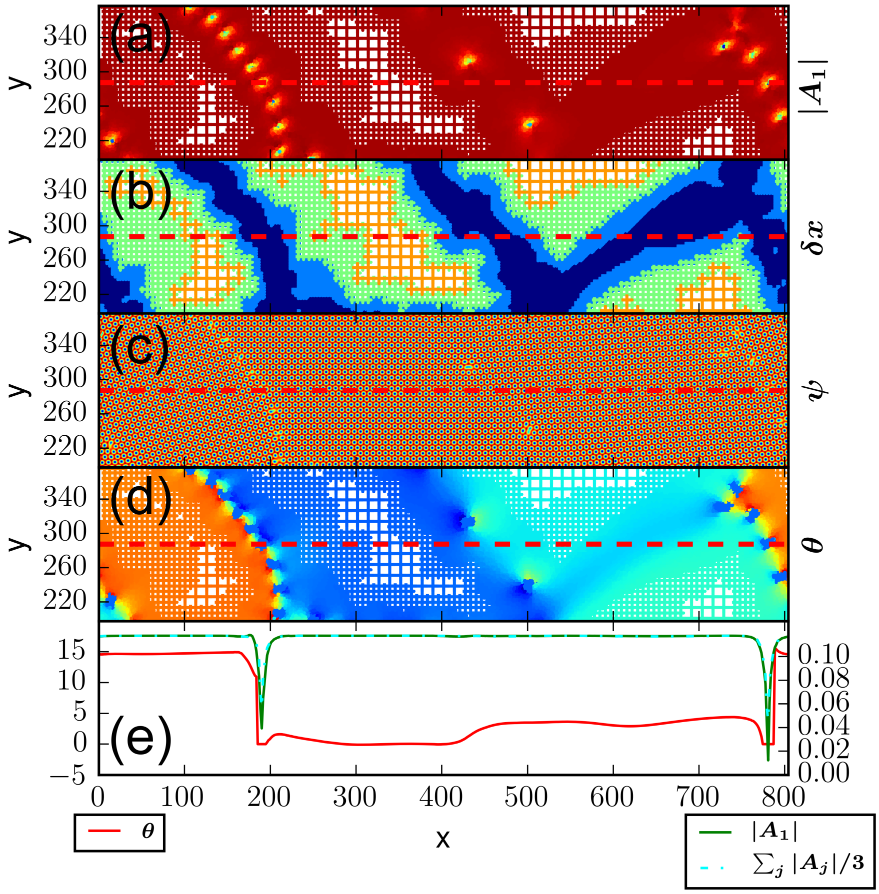

Figure 5.5: Selected variables in excerpt and cross section at $t = 560$. From top to bottom: (a) absolute value of the first complex amplitude $|A_1|$, (b) local mesh refinement δx, (c) reconstructed density field ψ and (d) local rotation θ. Values of θ, $|A_1|$ and $\sum_j |A_j|/3$ in cross section on the marked line at $y = 183\pi/2 \approx 287$ are shown in the last image (e). The local rotation field correctly tracks the grain rotation and shows large changes only on the grain boundaries.

A comparison with the results obtained on a regular grid is shown in Fig. 5.6 where the field $|A_1|$ is shown in cross section. The results are compared at two different times, in the top row (a-b) at $t = 160$ where the seeds are still growing into the undercooled melt, and in the bottom row (c-d) at $t = 560$ when the entire simulation domain has already solidified. The comparison is made between the exact values obtained on the computational nodes of the adaptive mesh that lie exactly on the cross section cut line, interpolated values from the adaptive mesh and results obtained on the uniform grid. All results are in excellent agreement, with small differences observed only at the solid-liquid interface and grain boundaries.

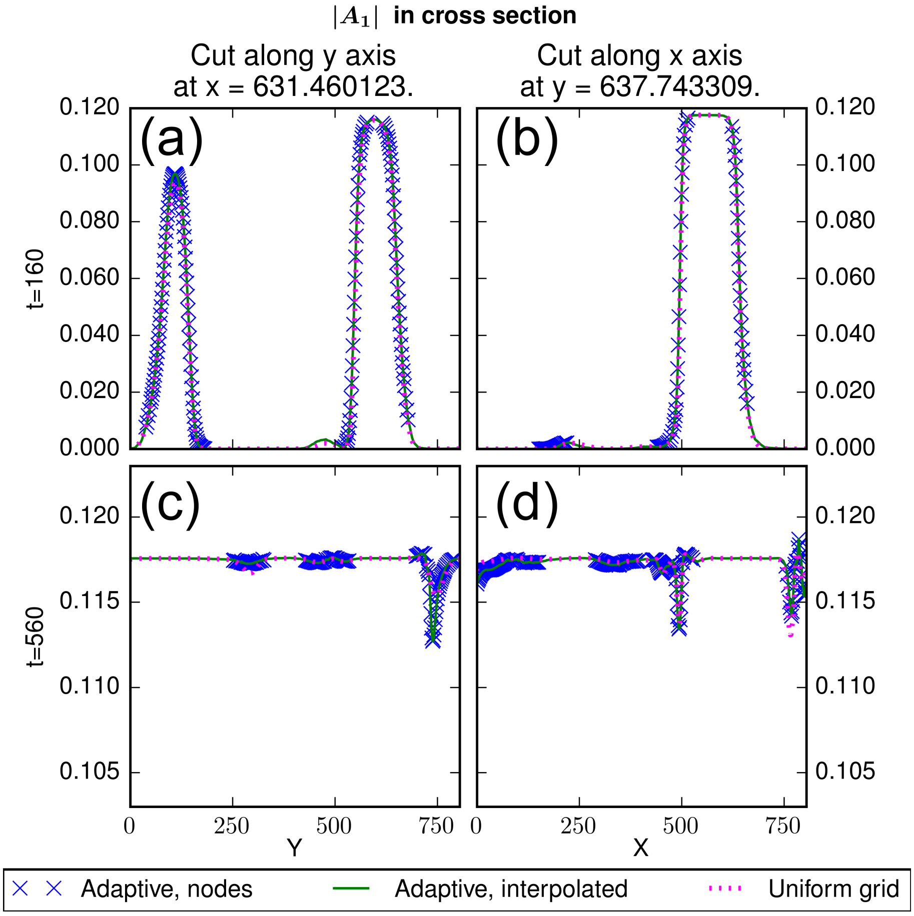

Figure 5.6: Amplitude $|A_1|$ in cross section cut along the lines $x = 201\pi \approx 631$ and $y = 203\pi \approx 638$ at times $t = 160$ and $t = 560$. Results obtained with AMR using a local rotation on an adaptive grid match the results obtained with simulations on a uniform grid. Exact values at the intersected computation nodes of the adaptive grid are shown in combination with interpolated values from the same grid in comparison with values obtained on a uniform grid.

As expected, the number of computational nodes required in the new approach is similar to that achieved by Athreya *et al.* [9] using a hybrid implementation. During simulation of the solidification, the number of computational nodes grows linearly in time at first, as the interface of the growing grains becomes larger, which may be seen in Fig. 5.7. As the mesh coarsening can be achieved in all grains, regardless of their orientation, the final number of computational nodes is significantly lower than the number of nodes of a regularly spaced grid of a similar size.

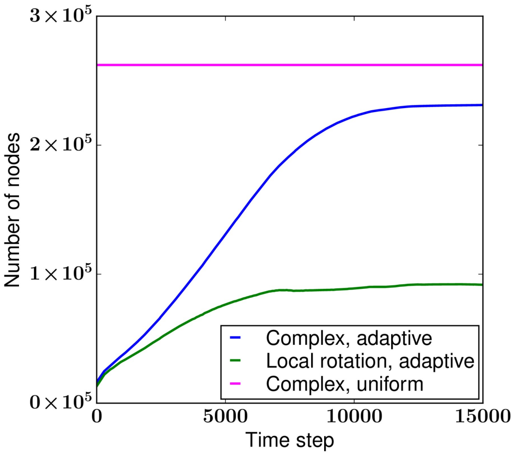

Figure 5.7: Number of computational nodes as a function of time for the summations shown in Figs. 5.2 and 5.4. After the liquid freezes, the number of nodes stops increasing. When using the scheme with a local rotation, the mesh coarsens in all nodes and therefore consists of a much smaller total number of nodes.

In order to further verify that the introduction of a local rotation field does not introduce additional errors into the calculation when local rotation is not correctly determined, we ran two simulations of an example with three seeds in an undercooled melt, shown in Fig. 5.8. One of the seeds was rotated by 2.5°, and the other two by 7.5°. The atomic lattices of two seeds with the same rotation were mutually shifted by half of the lattice spacing, resulting in an area with pure elastic deformation without rotation (at $x \approx 280$ in Fig. 5.8). In the first simulation run we let our algorithm determine the best local rotation field, and in the second run we set the local rotation field to a chosen, time independent function $\Theta(\mathbf{x}) = \Theta(x)$. We chose to use a regular grid for this simulation, as this eliminates numerical errors originating from AMR and allows for a better understanding of errors originating from imprecisions in determining the local rotation. The simulations shown in Fig. 5.8 show that the microstructure obtained in both simulation runs is virtually the same, with minor differences only around dislocation cores. The first row of the image (a) shows the microstructure obtained when our algorithm determines the local rotation and the second row (b) shows the case where we fix the local rotation to a time independent function $\Theta(x)$. The third row (c) shows local rotation as determined by our algorithm. Possible performance of our algorithm is limited by the amount of deformation that remains in the rotated amplitudes A_j^ϑ after rotation and this remainder $\Delta\epsilon = \sqrt{\sum_{i,j} E_{i,j}}$ is presented in the forth row image (d) and in cross section in the bottom row (e) in Fig. 5.8. Local rotation Θ as determined by our algorithm and the imposed rotation $\Theta(x)$ used in our second simulation run are shown in cross section plots in the last row image (e) as well. $\mathbf{E}$ is defined as

$$\mathbf{E} = \mathbf{R}(\text{-}\vartheta)\mathbf{F} - \mathbf{I} \tag{5.21}$$

where ϑ is the rotation determined by our algorithm and $\mathbf{F}$ is the deformation gradient [53], defined as

$$\mathbf{F} = \mathbf{I} + \nabla\mathbf{u} = \mathbf{I} + \frac{2}{3}\sum_{j=1}^{3} \mathbf{k}_j \nabla(arg(A_j)) \tag{5.22}$$

As the deformation gradient can be split into rotation $\mathbf{R}(\tilde{\vartheta})$ and pure deformation $\mathbf{U}$ by polar decomposition as $\mathbf{F} = \mathbf{R}(\tilde{\vartheta})\mathbf{U}$, the parameter $\Delta\epsilon$ vanishes when our algorithm can determine the correct local rotation ($\vartheta = \tilde{\vartheta}$) and there is no pure deformation ($\mathbf{U} = \mathbf{I}$). In the last row in the Fig. 5.8 we can see that the local rotation removes almost the entire deformation in the interior of grains with $\Delta\epsilon$ quickly dropping below 0.05. Around dislocations and on the grain boundaries a significant portion of the deformation remains, but this does not result in increased errors in the calculations. The comparison between images in the first and second rows in Fig. 5.8 shows that the microstructure remains the same even if we use incorrect local rotation in large areas of the computational domain. This is a consequence of rotational covariance of evolution equations, and due to this property the calculations are independent of the actual rotation used. Additional errors are not introduced due to possible inaccurracies in the calculation of a local rotation field. The new method is best understood as an exploit of the rotational covariance of the evolution equations that locally transforms the equations to a set of rotated amplitudes A_j^ϑ, defined on a set of basis vectors aligned with the local grain. This removes fast variations of the real and imaginary part of the complex amplitudes in misaligned grains that originate from rotation of the grain. With only slow variations in complex amplitudes remaining, the AMR can be effectively used in the entire simulation domain using only the Cartesian representation.

Therefore the idea of a local rotation should not be understood as a way to approximate values of the complex amplitudes and does not require additional assumptions to work. Just as AMR can be applied to a basic complex amplitudes model, the new model can be used in cases where large deformations are expected. When rotated grains are simulated with basic complex amplitudes models, the use of AMR is ineffective as the high spatial variations of amplitudes require high mesh refinement, but does not produce inaccurate results. The computational mesh refines and computational efficiency is lost, but not the accuracy. When areas with large deformations are encountered in our new model, the local rotation cannot eliminate the variations in the Cartesian representation of the complex amplitudes and the mesh refines. This results in the same accuracy as we would achieve without local rotation, with some loss in the computation speed.

Besides enabling the coarsening of the computational mesh in all grains using only the Cartesian representation of the amplitude equations, the new model helps to resolve another pressing issue of modeling with complex amplitude equations. With some aditional improvements, to be reported in detail elsewhere, we were able to eliminate an unphysical grain boundary that appears when the misfit between the impinging grains approaches the crystal's symmetry rotation (60° in our case). As reported by Spatschek and Karma [10], the amplitude equations formalism is unable to properly model grain boundaries where interfacing grain rotations differ by more than half of the angle of the crystal symmetry rotation. Our initial simulations indicate that improvements resulting in the use of a local rotation field could also lead to better modeling of grain boundaries for a whole range of misorientations.

5.5 Conclusions

A new model is presented for solving complex amplitude equations on an adaptive mesh, which solves the problem of beats in misaligned grains and allows for mesh coarsening in all grains. It is based on the observation that the beats disappear when the basis vectors for the amplitudes are correctly rotated. The proper rotation of the basis vectors was derived from the complex amplitudes and stored in an auxiliary variable used in calculations. The rotational covariance of the operators used in the evolution of the complex amplitudes allowed us to separate the conversion between differently rotated fields from the evolution equations. The results obtained using the new approach closely match the results obtained with existing models.

The new model's computational efficiency scales in the same way as the hybrid approach described by Athreya *et al.* in [9]. The model does not require a presumption of a frozen phase gradient inside the solidified grains and uses only the Cartesian representation of the fields in the entire computational domain.

The model shows promise with regard to modeling grains of a larger rotation range. With some improvements to the model, the unphysical grain boundary between grains which differ in rotation by a multiple of the crystal's symmetry rotation can be removed.

We confirmed that the model is resilient to inaccuracies in the calculation of a local rotation angle, and does not introduce errors into calculations even in areas where large strains exist. This is an expected consequence of the main idea of the new model: it is an exploit of the rotational covariance of the evolution equations, aimed at enabling AMR mesh coarsening in all grains.

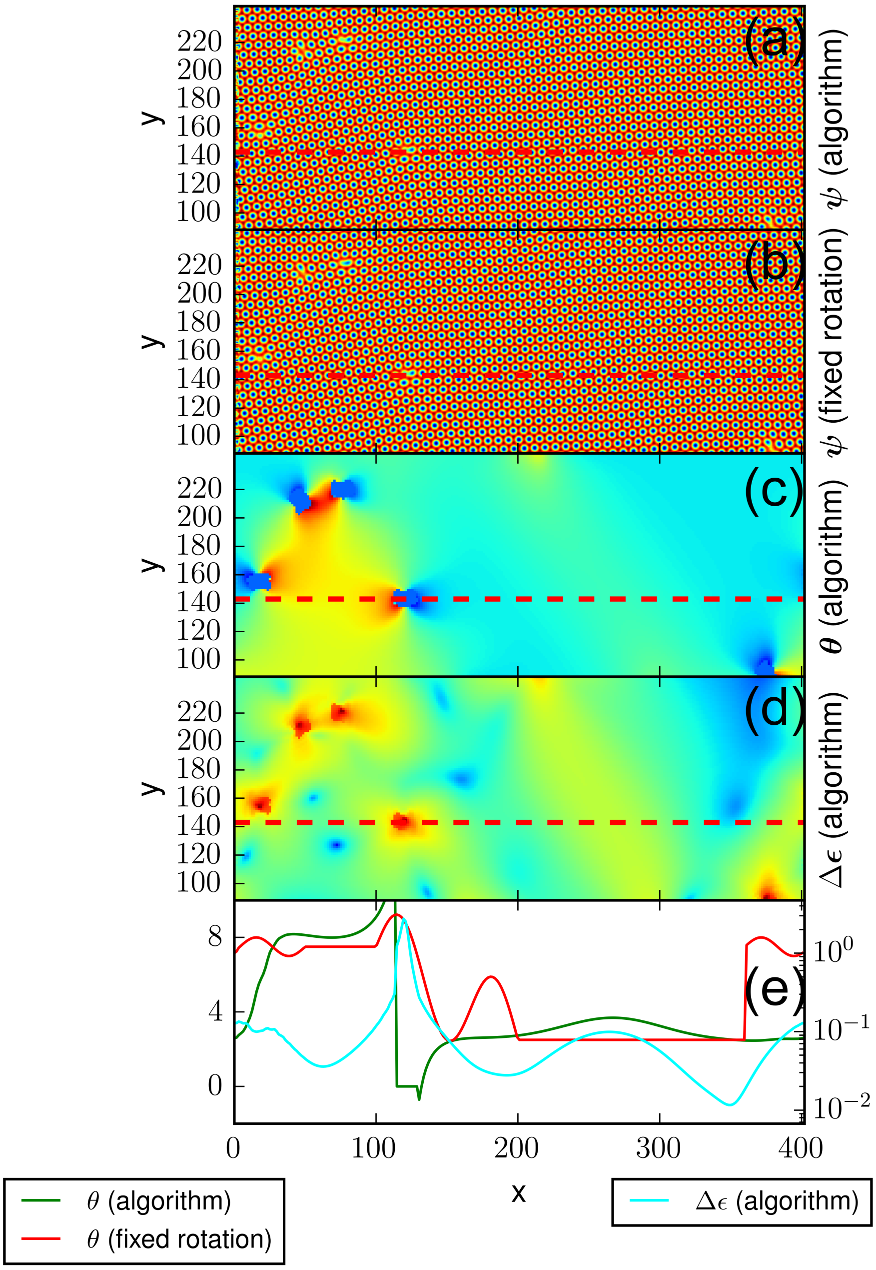

Figure 5.8: Accuracy of the simulations under conditions where local rotation might be incorrectly calculated or where large deformations exist. (a) microstructure of a simulation run where our algorithm determined local rotation. (b) microstructure of a simulation run where local rotation was fixed to a chosen function $\Theta(\mathbf{x}) = \Theta(x)$. The microstructure in both simulation runs matches closely, with minor differences observed only around dislocations. (c) local rotation field Θ as determined by our algorithm. (d) deformation remainder $\Delta\epsilon$, shown in logarithmic scale. (e) local rotation Θ as determined by our algorithm, the chosen function $\Theta(x)$ and deformation remainder $\Delta\epsilon$ in cross section. $\Delta\epsilon$ remains low inside grains, in the area with pure elastic deformation at $x \approx 280$ shows a small increase coupled with some inaccuracy in the calculation of a local rotation field Θ and rapidly increases in the vicinity of the dislocation at $x \approx 120$.

Chapter 6

Unphysical Grain Boundary in APFC model

This chapter introduces improvements to the amplitude expansion of the phase field crystal model (APFC) that enable the simulation of grains within a full range of orientations. The unphysical grain boundary between grains, rotated by a crystal's symmetry rotation, is removed using a combination of the auxiliary rotation field described in chapter 5 and an algorithm that correctly matches the complex amplitudes according to the differences in local rotation Copyright of this chapter is held by © *American Physical Society* [1].

6.1 Introduction

The microstructure plays a crucial role in determining the properties of many modern industrially important materials. Since experiments are expensive and the relationships between chemical composition, thermo mechanical processing, and the final microstructure are complex, computer simulations are an important step in the design of new materials. In order to be able to competitively price the final product, material production usually occurs in large batches of material. Computer simulations able to efficiently model processes occurring on such a large span of spatial and temporal scales are scarce, and frequently include a hierarchy of different models for modeling processes on different scales that exchange parameters. Discontinuous transitions between the different scales

---

[1] Copyright (2019) by the © *American Physical Society.*

sometimes introduce nonphysical phenomena that are hard to eliminate, therefore making use of a single model preferable. In order to enable modeling of the microstructure on diffusive time scales, the phase-field-crystal model (PFC) was developed [5, 6]. A recently developed amplitude expansion of the PFC model (APFC) [7, 8] can predict the microstructure of materials in relatively large simulation domains, and in combination with effective mesh refinement techniques (AMR) [9, 62] can span many different scales in a continuous manner.

The PFC and APFC models were successfully applied to the study of many different phenomena such as ferromagnetic [24] and ferroelectric [25] effects, the effects of hydrodynamic velocity on the microstructure formation [54], the study of grain boundary motion and polycrystalline films [7, 8, 38], structural phase transitions [14, 15, 48] and grain boundary energies [51, 55]. The models were improved to cover a wide range of possible materials, including materials with different crystal lattices [12, 16, 17, 46, 48, 49, 51, 52] in 2D and 3D, materials with spatial anisotropy [21], liquid crystals [22, 23], binary systems [10, 49, 50] and multi-component alloys [18], improved to achieve instantaneous mechanical equilibrium [53] and tune the energy of defects and interfaces [55].

In our recent work [62], we presented a new way to achieve adaptive mesh refinement in APFC models using an auxiliary local rotation field. The local rotation field was derived from the fields used in the computation, but was itself never used in calculations. It was used only to convert the amplitude equations in a system, aligned with the local grain, where the so-called beats in the amplitudes disappeared and AMR algorithm was able to coarsen the mesh.

In this work we show how the local rotation field can be used to eliminate an unphysical grain boundary described by Spatschek *et al.* [10], occurring between grains rotated by a crystal's symmetry rotation, and enable APFC simulations with a whole range of grain orientations. This can enable APFC simulations of industrially important thermo-mechanical processes where grain rotation occurs, such as the hot and cold forming of metallic materials.

6.2 APFC model

The PFC model operates on a local atomic density function ψ which minimizes the free energy functional [5, 6, 51, 53] given here in terms of dimensionless field ψ tracking the deviations of the atomic density field from its average

$$F = \int d\mathbf{r} \left\{ \frac{\Delta B}{2}\psi^2 + B^x \frac{\psi}{2}(1+\nabla^2)^2\psi - \frac{t}{3}\psi^3 + \frac{v}{4}\psi^4 \right\} \tag{6.1}$$

where $\Delta B = B^l - B^x$. Parameter B^l is related to the compressibility of the liquid state and B^x to the elastic moduli of the crystalline state. The choice of t and v determines the magnitude of the amplitudes and the liquid-solid miscibility gap. The single-mode solution of the PFC equation in the solid phase has triangular symmetry within a certain range of parameters and the solution can be approximated as [7–9]

$$\psi \approx \sum_{j=1}^{3} A_j e^{i\mathbf{k_j}\cdot\mathbf{x}} + \sum_{j=1}^{3} A_j^* e^{-i\mathbf{k_j}\cdot\mathbf{x}} \tag{6.2}$$

where A_j are the complex amplitudes of waves aligned with the wave vectors

$$\begin{aligned} \mathbf{k}_1 = &\quad k_0(-\boldsymbol{i}\sqrt{3}/2 - \boldsymbol{j}/2), \\ \mathbf{k}_2 = &\quad k_0\boldsymbol{j}, \\ \mathbf{k}_3 = &\quad k_0(\boldsymbol{i}\sqrt{3}/2 - \boldsymbol{j}/2), \end{aligned} \tag{6.3}$$

In order to be able to compare our results with already published results, we used the same free energy functional and dynamic equations for our APFC model as in Hirvonen *et al.* [51]. The free energy and the dynamic equations are

$$\begin{aligned} F = &\quad c_A \textstyle\int d\mathbf{r}\{(\Delta B/2)A^2 + (3v/4)A^4 - 2t(\prod_{j=1}^{3} A_j + c.c.) \\ &\quad + \textstyle\sum_{j=1}^{3}(B^x|\mathcal{L}_j A_j|^2 - (3v/2)|A_j|^4)\} \end{aligned} \tag{6.4}$$

$$\frac{\partial A_j}{\partial t} = -[\Delta B + B^x\mathcal{L}_j^2 + 3v(A^2 - |A_j|^2)]A_j + 2t\prod_{k\neq j} A_k^* \tag{6.5}$$

where $\mathcal{L}_j = \nabla^2 + 2\mathbf{k}_j \cdot \nabla$ and $A^2 = 2\sum_{j=1}^{3}|A_j|^2$. The dynamic equations are derived using non-conserved, dissipative dynamics. We chose the same set of parameters as Hirvonen *et al.* [51] ($B^l = 1$, $B^x = 0.98$, $t = -1/2$, $v = 1/3$, $c_A = 7.95eV$, $a_0 = 2.46\text{Å}$).

Solving the dynamic equations (6.5) in Cartesian representation has two main drawbacks. First, the grains' rotation is expressed by the so-called beats in the complex amplitudes and therefore the AMR techniques are ineffective. The beats prevent the mesh from refining in all grains that are not aligned with the initial choice of basis vectors [9]. Second, the grain boundaries between grains that differ in orientation by more than half of the crystal's symmetry rotation (30° in our case) show the effects of an unphysical grain boundary [10] that is formed between grains that differ in rotations by the crystal's symmetry rotation. Both of these shortcomings prevent APFC simulations with grains in a full range of misorientations on larger simulation domains. In order to overcome these limitations, we improved a model employing a local rotation field described in our previous work [62].

6.3 Description of improvements to the model

Our model introduces a set of locally-rotated complex amplitudes [62] A_j^ϑ

$$A_j = A_j^\vartheta e^{i\delta\mathbf{k}_j(\vartheta)\cdot\mathbf{x}} \tag{6.6}$$

where ϑ is a local rotation field and $\mathbf{k}_j(\vartheta) = \mathbf{k}_j + \delta\mathbf{k}_j(\vartheta)$ are rotated basis vectors. The local rotation field ϑ is incrementally derived from the complex amplitudes A_j based on the observation that, when the rotation of the basis vectors matches the rotation of the local grain, the beats disappear and therefore the gradient of the locally rotated amplitudes is zero:

$$\nabla A_j^\vartheta = (\nabla A_j)e^{-i\delta\mathbf{k}_j\cdot\mathbf{x}} + A_j(-i\delta\mathbf{k}_j)e^{-i\delta\mathbf{k}_j\cdot\mathbf{x}} = 0 \tag{6.7}$$

We incrementally update the local rotation field using

$$\delta\mathbf{k}_j(\vartheta) = \frac{\nabla A_j}{iA_j} = \mathbf{k}_j(\vartheta) - \mathbf{k}_j \tag{6.8}$$

where we average the rotation angle derived from (6.8) over all complex amplitudes. Due to the rotational covariance of the operator $\mathcal{L}_j$, the conversion between the basis vectors rotated by a different amount can be separated from the operator evaluation and the adaptive mesh can coarsen in all grains, regardless of the orientation. To apply an operator $\mathcal{L}_j$ on a locally rotated field $X \in \{A_j^\vartheta, L_j^\vartheta A_j^\vartheta\}$, the local rotation is treated separately as in [62]

$$\mathcal{L}_j^\vartheta X_j^\vartheta = e^{-i\delta\mathbf{k}\cdot\mathbf{x}}\mathcal{L}_j X_j \tag{6.9}$$

In the current work, we present a new way to eliminate the unphysical grain boundary between grains rotated by a crystal's symmetry rotation, using a local rotation field in combination with an algorithm that uses the local rotation field to correctly match the complex amplitudes in neighboring computational nodes. The algorithm is based on an observation that the approximation of the single-mode solution (6.2) is the sum of planar waves directed at angles that are multiples of the crystal's symmetry rotation. Table 6.1 lists the wave vectors, the angles they form with the first wave vector $\mathbf{k}_1$, the complex amplitudes A_j matching the selected wave vector, and the wave vectors we obtain with one crystal's symmetry rotation ($\pm 60°$). Our algorithm finds the best matching complex amplitudes in neighboring computational nodes by comparing the local rotation of both nodes. If the local rotation ϑ differs by more than half of the crystal's symmetry rotation ($|\vartheta_L - \vartheta_R| > 30°$), the algorithm matches the complex amplitude A_1 in one computational node with A_2^* or A_3^* in the other computational node, depending on the sign of the difference. A full list of matching amplitudes is presented in Table 6.1. In Fig. 6.1, the wave vectors in two neighboring computational nodes with different local rotations are shown. The algorithm used is the same as in [62], with the following two additions. First, when an operator is evaluated on a locally rotated field, the matching amplitudes from neighboring nodes are used. In case the differences in local rotations between nodes are greater than half of the crystal's symmetry rotation, the matching algorithm uses Table 6.1 to find appropriate matching amplitudes. Second, after the optimal local rotation is found in all solidified regions, the found local rotation is propagated to the neighboring nodes in liquid regions, and the propagation step is repeated 10 times.

Table 6.1: A list of wave vectors, their rotation and corresponding amplitudes. The matching amplitudes when the rotation is shifted by one crystal's symmetry rotation in either direction are shown in the table's last two columns.

Direction	Rotation	Amp.	Amp. (+60°)	Amp. (−60°)
$+\mathbf{k}_1$	0	A_1	A_2^*	A_3^*
$-\mathbf{k}_2$	60	A_2^*	A_3	A_1
$+\mathbf{k}_3$	120	A_3	A_1^*	A_2^*
$-\mathbf{k}_1$	180	A_1^*	A_2	A_3
$+\mathbf{k}_2$	240	A_2	A_3^*	A_1^*
$-\mathbf{k}_3$	300	A_3^*	A_1	A_2

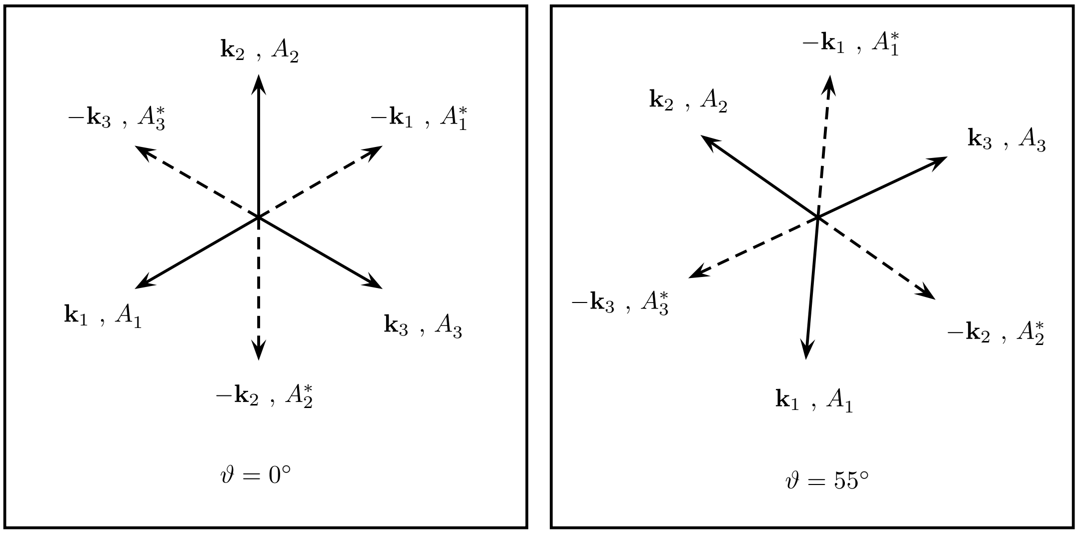

Figure 6.1: Wave vectors in two neighboring computational nodes with different local rotations (left: $\vartheta = 0°$, right: $\vartheta = 55°$). Our algorithm matches the complex amplitudes that correspond to the wave vectors that point in the closest directions. A_2 in the left computational node is therefore matched with the complex amplitude A_1^* in the right computational node, as the angle between the corresponding wave vectors is only 5°.

The first improvement eliminates the unphysical grain boundary occurring between grains that differ in orientations by more than half of the crystal's symmetry rotation. The second improvement ensures that our limit on the change in local rotation at each time step does not prevent boundaries with a mismatch close to the crystal's symmetry rotation from forming. Without this step, the algorithm smoothens a grain boundary between grains with misorientations of 0° and 55° and creates a region in which the local rotation continuously transitions between angles in the solid regions, which prevents the first improvement from finding the correct matching amplitudes on the interface.

6.4 Results

Figure 6.2 shows a grain boundary at a 50.1° tilt angle. Without amplitude matching, the result is a grain boundary that would correspond to an effective tilt angle of 50.1°, which is impossible as the crystal's symmetry rotation of 60° limits the effective tilt angles to 30°. With the amplitude matching algorithm, the amplitudes on both sides of the grain boundary that correspond to wave vectors pointing in the most similar directions are properly matched and the result is a grain boundary with a similar structure

Algorithm 3 Local rotation adjustment. Parameters p, q, $A_{\text{min. amp.}}$ and $\vartheta_{\text{max. phase}}$ are heuristic.

```
for each computation node do
    Find optimal rotation $\vartheta_{\text{opt}}$:
    if $|A_j^{\vartheta}| > A_{\text{min amp.}}$ then
        In solidified regions: from gradient
        for all $j \in \{1, 2, 3\}$ do
            $\delta\mathbf{k}_j(\vartheta_{\text{current}}) = Re(\frac{\nabla A_j^{\vartheta_{\text{current}}}}{iA_j^{\vartheta_{\text{current}}}})$
            $\vartheta_{x,j} = 1 + \mathbf{k}_j(\vartheta_{\text{current}}) \cdot \delta\mathbf{k}_j$
            $\vartheta_{y,j} = (\mathbf{k}_j(\vartheta_{\text{current}}) \times \delta\mathbf{k}_j) \cdot \hat{\mathbf{e}}_z$
        end for
        $\vartheta_{\text{opt}} = \vartheta_{\text{current}} + atan2(\sum_j \vartheta_{y,j}/3, \sum_j \vartheta_{x,j}/3)$
    else
        In liquid regions: drop towards zero
        $\vartheta_{\text{opt}} = 0$
    end if
    Smooth the changes
    $\vartheta_{\text{new}} = p \times \vartheta_{\text{current}} + q \times \vartheta_{\text{opt}}$
    Prevent skipping beats
    $d\vartheta = \max_{\{\text{all neighbours NN}\}} |\vartheta_{NN} - \vartheta_{\text{new}}|$ modulo 60°
    $k_{\vartheta} = dx\ d\vartheta/\vartheta_{\text{max. phase}}$
    if $k_{\vartheta} > 1$ then
        $\vartheta_{\text{new}} = \vartheta_{\text{current}} + (\vartheta_{\text{new}} - \vartheta_{\text{current}})/k_{\vartheta}$
    end if
    $\vartheta_{\text{current}} = \vartheta_{\text{new}}$
end for
for 10× propagate local rotation into liquid regions do
    for each computation node do
        if $|A_j^{\vartheta}| > A_{\text{min. amp.}}$ then
            mark node as "rotation is set"
        else if this node has a marked NN then
            $\vartheta_{\text{current}}$ = average $\vartheta$ over all marked NN
            mark node as "rotation is set"
        end if
    end for
end for
```

to a 10° = 60° − 50° grain boundary, as expected.

We calculated the grain boundary energies with our improved algorithm and compared them with results published by Hirvonen *et al.* [51]. Our improvements result in

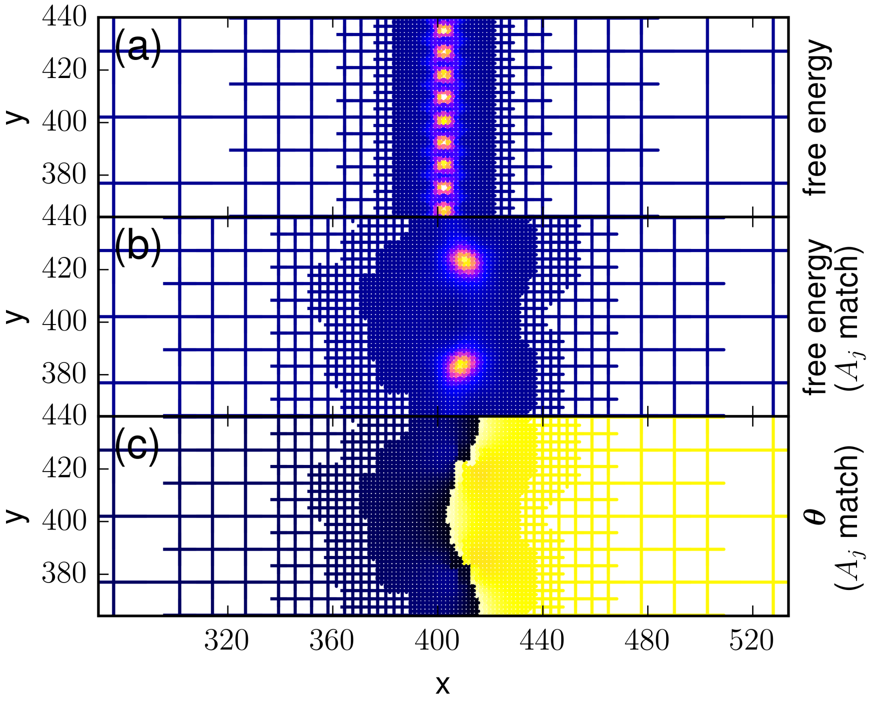

Figure 6.2: Free energy on the grain boundary in armchair configuration at a mismatch angle of 50.1°. The top row: (a) shows an unphysical grain boundary that is formed between grains at mismatch angles larger than half of the crystal's symmetry rotation [10]. Middle row: (b) shows the same grain boundary as formed in simulations with our improved algorithm that correctly matches complex amplitudes at different rotations, and therefore the unphysical effects do not occur. Bottom row: (c) shows the local rotation as used in our improved algorithm.

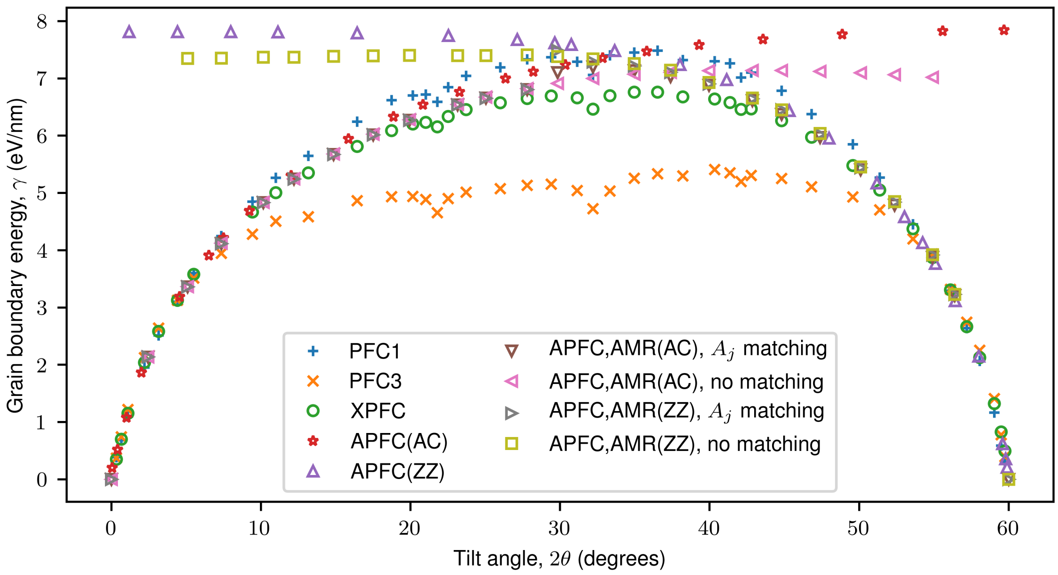

Figure 6.3: The grain boundary energy as a function of tilt angle. Values for models PFC1, PFC3, XPFC, APFC(AC) and APFC(ZZ) were published by Hirvonen *et al.* [51] and are in good agreement with our model. Our model without amplitude matching in armchair (AC) and zigzag (ZZ) configurations matches previously published results. Amplitude matching in either configuration successfully removes the unphysical increase in grain boundary energy observed when the tilt angle is more than half of the crystal's symmetry rotation away from a configuration in which complex amplitudes from both impinging grains are completely aligned.

the removal of the unphysical effects from improper matching of complex amplitudes on different sides of the grain boundary. In Fig. 6.3, we show the calculated grain boundary energies in comparison to [51]. In our calculations, we used two different ways of constructing a grain boundary, like [51] we constructed a grain boundary in armchair configuration using two grains that form a vertically oriented grain boundary and used a horizontal grain boundary for the zigzag configuration. The results of calculations obtained without the amplitude-matching algorithm agree well with previous results, and the small differences can be explained by numerical errors introduced by the use of the adaptive mesh refinement techniques and differences in construction of the grain boundaries. Results obtained with our amplitude-matching algorithm show a continuous transition between the results obtained with APFC(AC) and APFC(ZZ) configurations at an appropriate angle, confirming the successful removal of the unphysical effects on the grain boundaries.

The grain boundaries were constructed by seeding the simulation domain with a crystal phase upon two opposite rotations, as seen in Fig. 6.4. The rotation was chosen in such a way that the atomic density on the line between the domains with different orientations is exactly periodical. Before the start of the simulations, we melted the crystal phase in a small area around the grain boundary line. To calculate the grain boundary energy, we averaged the free energy density in the marked area in Fig. 6.4. The area matches the period of the initial atomic density in y direction and extends into pure, undeformed crystal in x direction. We used sufficiently large simulation domains ($L = 512\pi/2$) to ensure that the center-most area remains periodic in the direction along the grain boundary and the crystal is undeformed at both ends of the marked area. Due to these properties of the area over which we averaged the free energy density, the grain boundary energy can be calculated as

$$\gamma = \Delta F/\Delta y \tag{6.10}$$

where $\Delta F = F_{\square} - F_{crystal,\square}$ is the increase in free energy in the marked area and Δy is the grain boundary length (in the horizontal grain boundary configuration the axes are switched appropriately).

The effects of our improvements in an example of a simulation with many grains are presented in Fig. 6.5. 12 seeds with rotations in a full rotation range ($\theta \in [-30°, +30°)$) were grown in undercooled melt using the algorithm presented in this article and compared to our previous work [62]. We can see that the improvements remove unphysically

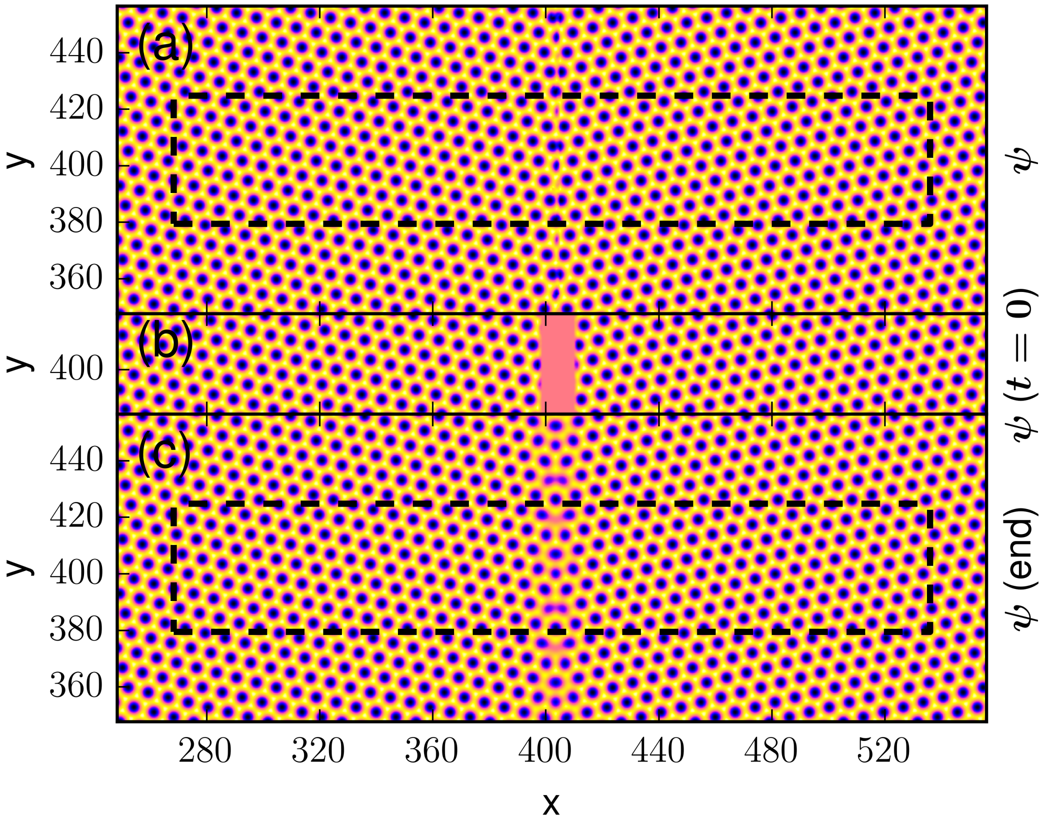

Figure 6.4: Grain boundary construction and calculation of free energy. In order to calculate the free energy of a symmetric tilt grain boundary, we simulate two impinging grains, each rotated by an angle at which the microstructure in the middle of the grains repeats periodically, presuming an infinite simulation domain. We calculate the free energy per grain boundary length from the average free energy in the marked regions.

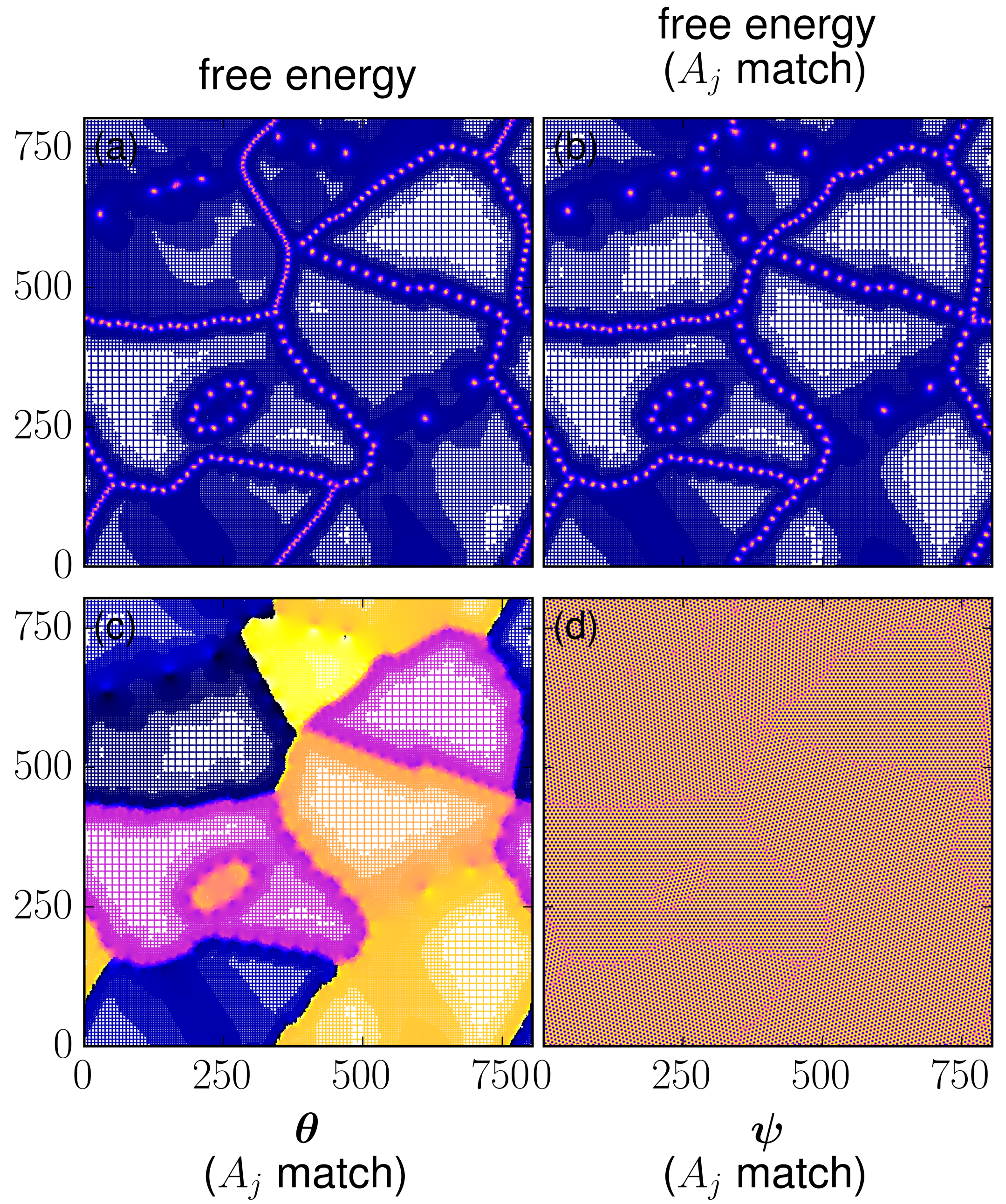

Figure 6.5: Grain boundary energies in an example simulation. 12 seeds with rotations in a full rotation range ($\theta \in (-30°, +30°)$) were placed in undercooled melt. The images in the top row show free energy density in the full simulation domain, as calculated: (a) with the algorithm published in [62], and (b) the algorithm presented here. We can see that our improved algorithm removes the unphysical effects on grain boundaries. The images in the bottom row show: (c) the local rotation field; and (d) the reconstructed microstructure.

high grain boundary energies on the grain boundaries where the impinging grains are at a tilt angle above 30°. Presuming a completely uniform distribution of grain orientations, this results in the removal of the unphysical effects on half of the grain boundaries.

6.5 Conclusions

This article presents a new improvement to the APFC model that removes the unphysical grain boundary that occurs in the APFC models between grains, rotate by a crystal's symmetry rotation. The origin of such an unphysical phenomena is in the dual representation of the rotation of the grains, first by the basis vectors and second by the beats in the complex amplitudes representing the density waved associated with the basis vectors. Our improvement removes the unphysical grain boundary by connecting both representations of grain rotation. The local rotation field tracking the grain rotation expressed by the beats in the complex amplitudes is connected to the rotation of the basis vectors through an angle to amplitude matching table. The approach eliminates the unphysical grain boundary in the model and the improved model demonstrates grain boundary energies matching best APFC models at a given real misfit at the grain boundary in the whole range of crystal orientations. This enables APFC simulations of processes where grain rotation occurs or where limiting the rotations of grains to an interval of values can not be justified.

6.6 Appendix A: Selected simulations in comparison

This section presents a selected set of simulations, useful for understanding the benefits and limitations of the presented improvements. All images show the local free energy density at the grain boundary on an adaptive mesh, in three different model/configuration combinations.

While the APFC model can not provide an accurate description of atomic structures around dislocations, it gives good approximations of the PFC model for small tilts and deformations [43], and has already been used to investigate grain boundaries. The dislocation density on the grain boundary determines the grain boundary free energy to a large extent, and the dislocation cores can be observed in plots of free energy density. Therefore we chose to present the grain boundaries in comparison in terms of free energy density plots. We present free energies obtained without amplitude matching algorithm in two configurations, armchair in the top row of the figures and zigzag in the bottom row. Plots of the zigzag configurations are transposed, as swapping x and y axes makes them easier to compare with other plots. In the middle row we present the results obtained with our improved model, which match the results obtained with the previous model in armchair configuration at small mismatch angles and those obtained in zigzag configuration for large mismatch angles, that is in mismatch ranges where the previous models derive correct free energy densities in a given configuration. In the middle of the range of misorientations ($25^\circ < \theta < 35^\circ$) we can observe a gradual transition of the microstructure obtained with our improved model between both correct limits. While there are some transient effects and the exact structure of dislocations does not match at all angles, the density of dislocations which determines the grain boundary properties matches the appropriate configuration (armchair for low mismatches, zigzag for large mismatches) of the previous models.

Note that in the images presenting grain boundaries with 0° or 60° mismatch, the adaptive mesh coarsens completely and only very few computational nodes of the adaptive mesh are shown. This is an expected and desired result.

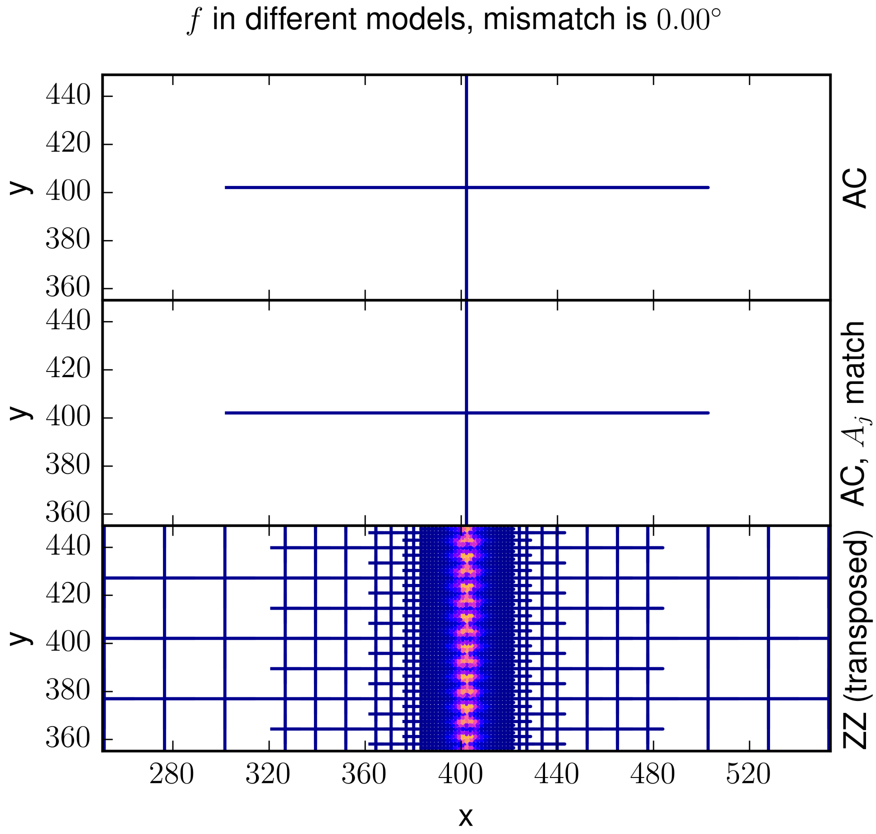
f in different models, mismatch is $0.00°$

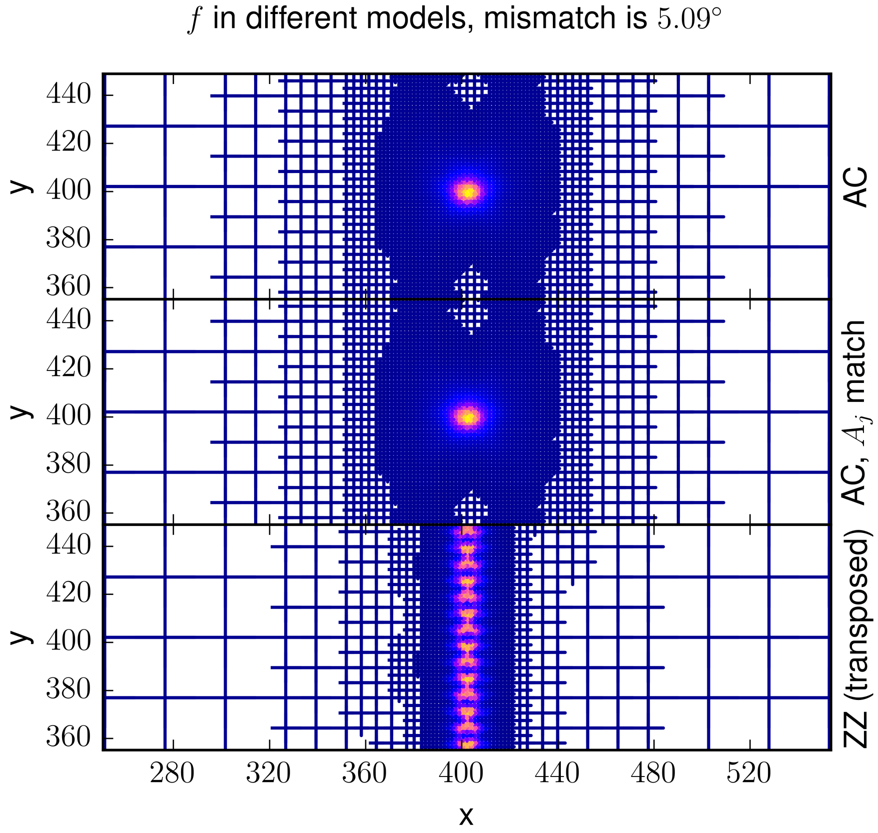
f in different models, mismatch is $5.09°$

Figure 6.6: Grain boundary structure at 0° and 5.09° misfits.

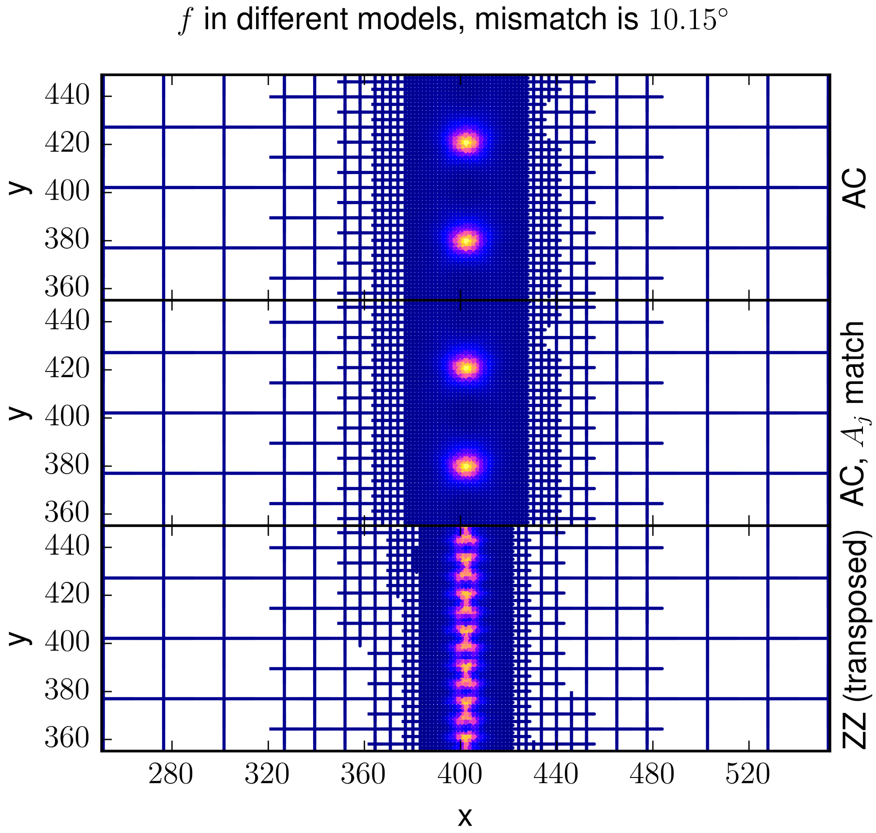

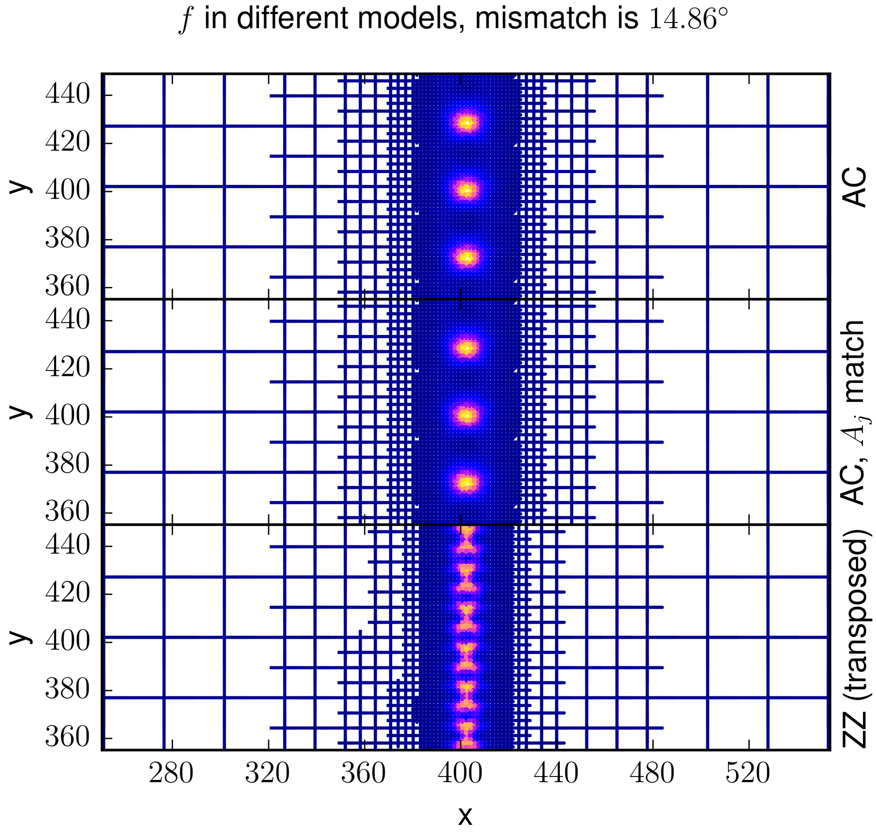

Figure 6.7: Grain boundary structure at 10.15° and 14.86° misfits.

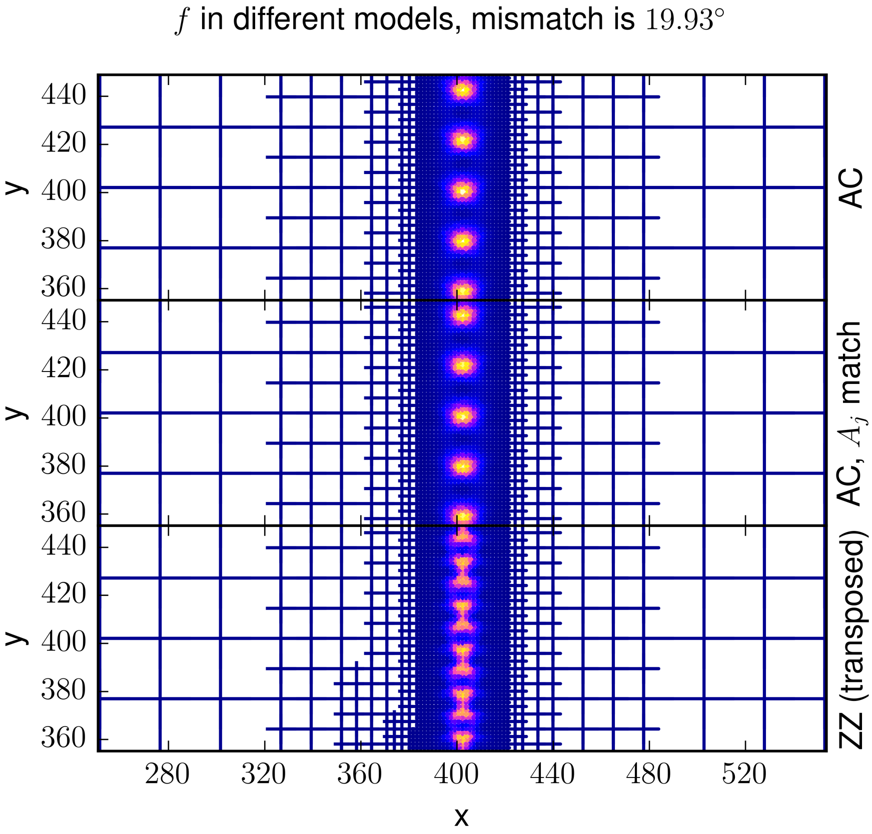

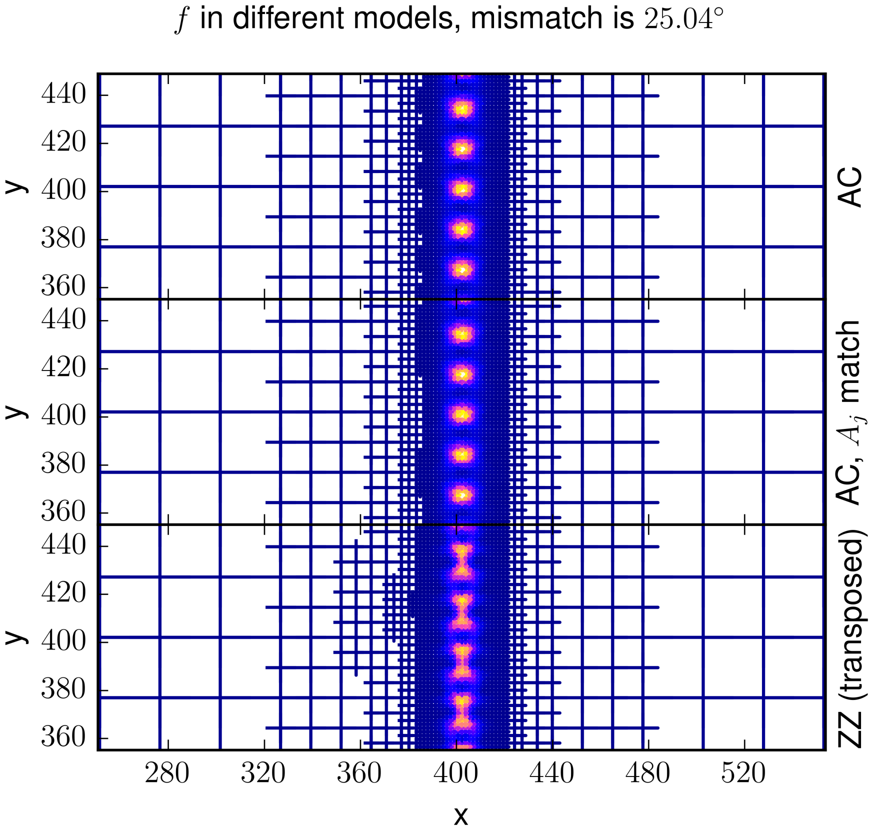

Figure 6.8: Grain boundary structure at 19.93° and 25.04° misfits.

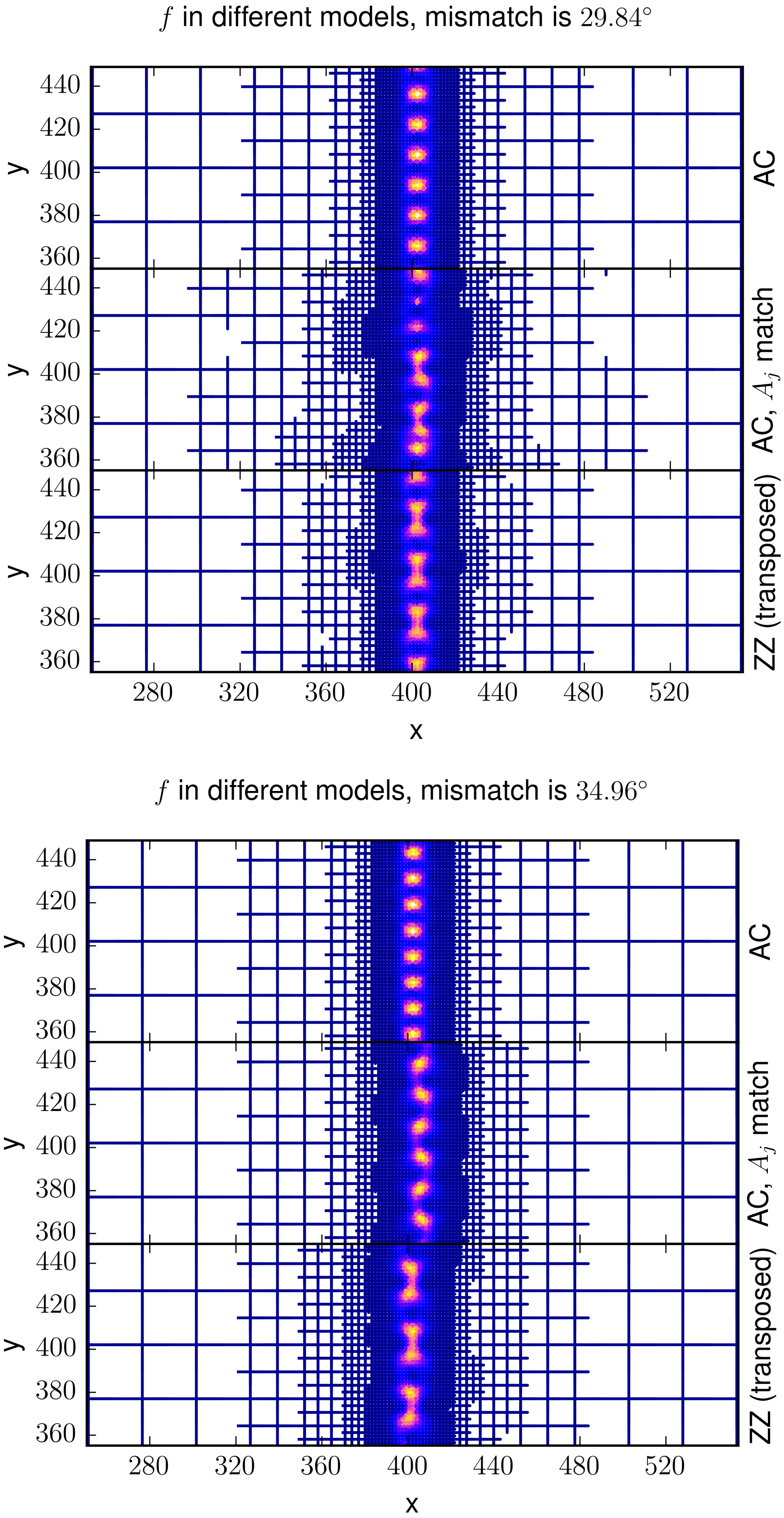

Figure 6.9: Grain boundary structure at 29.84° and 34.96° misfits.

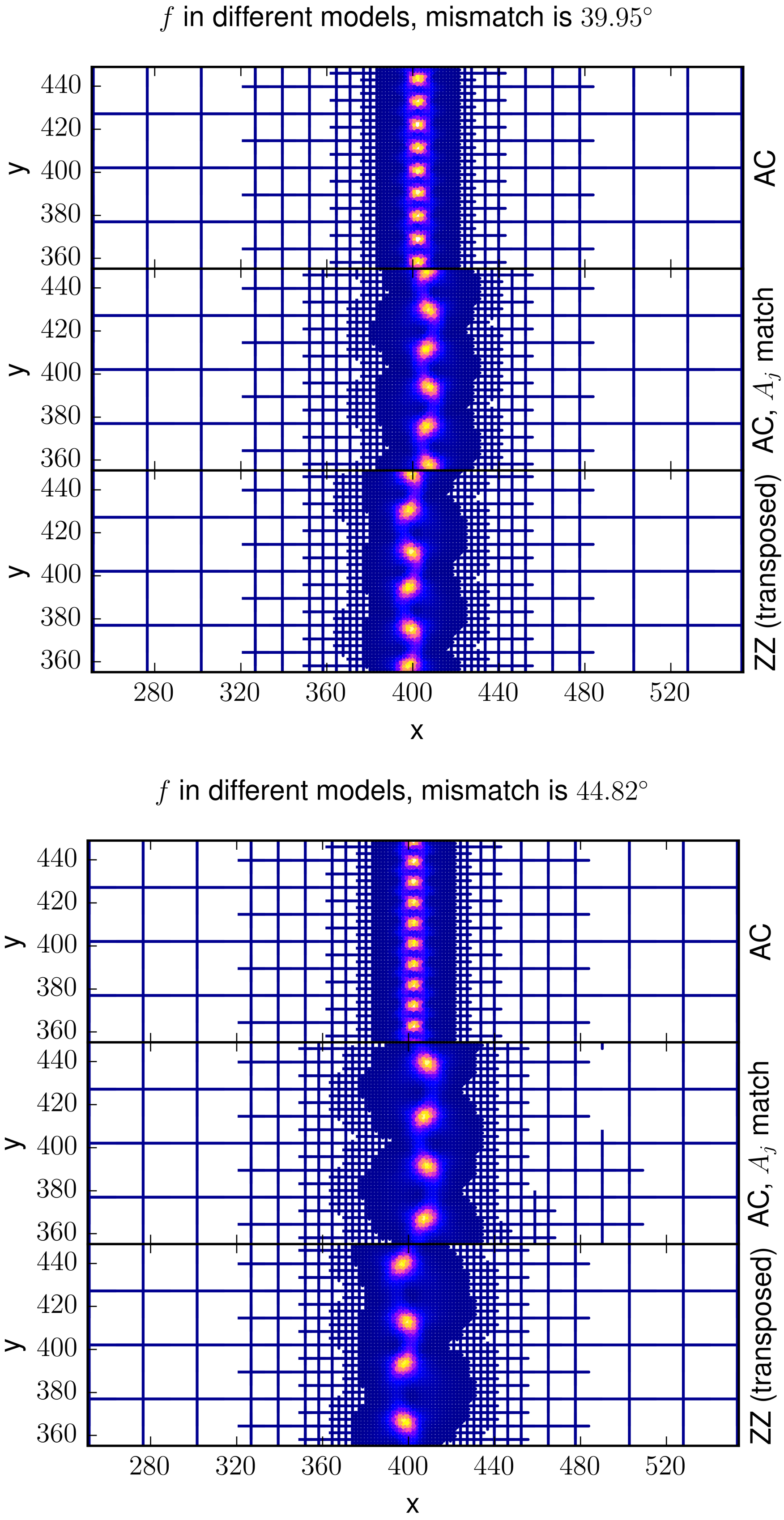

Figure 6.10: Grain boundary structure at 39.95° and 44.82° misfits.

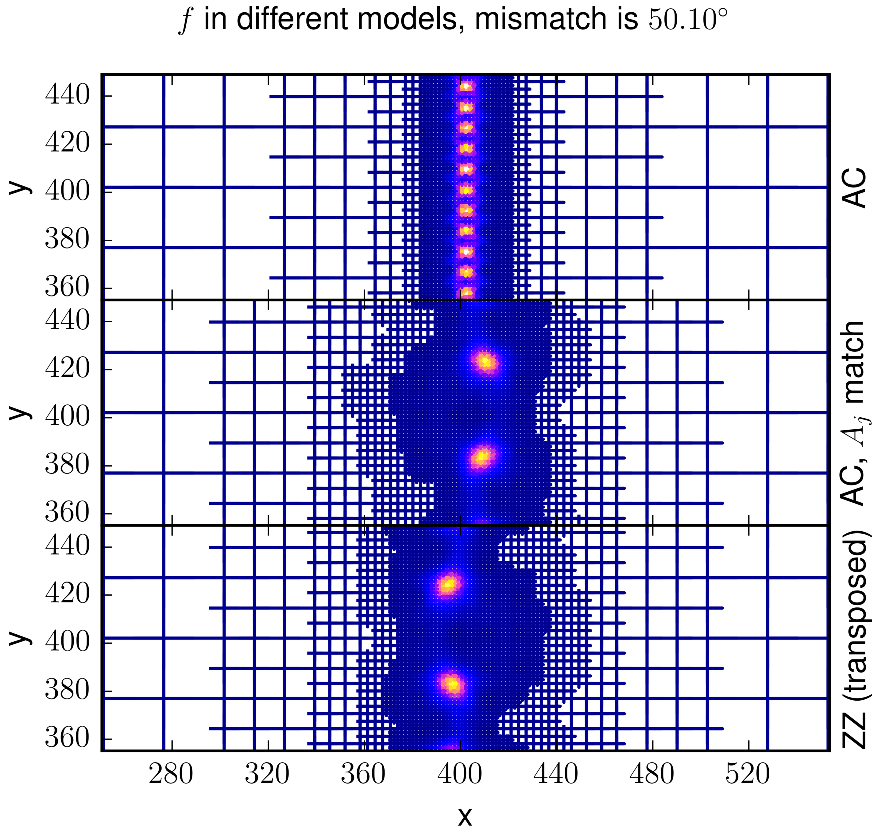
f in different models, mismatch is $50.10°$

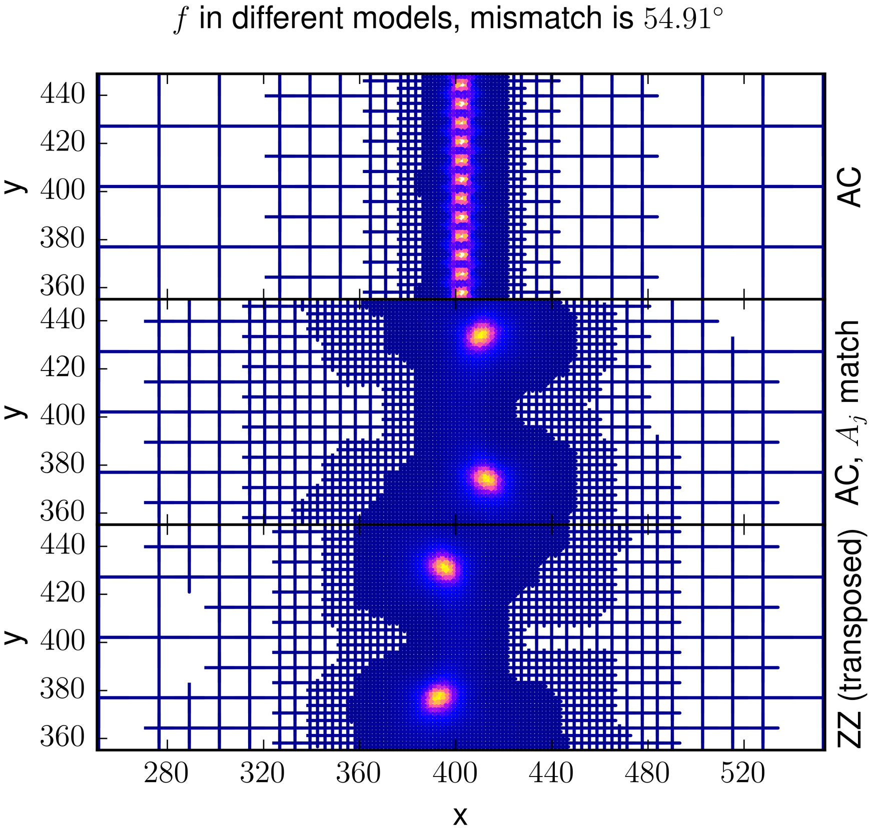
f in different models, mismatch is $54.91°$

Figure 6.11: Grain boundary structure at 50.10° and 54.91° misfits.

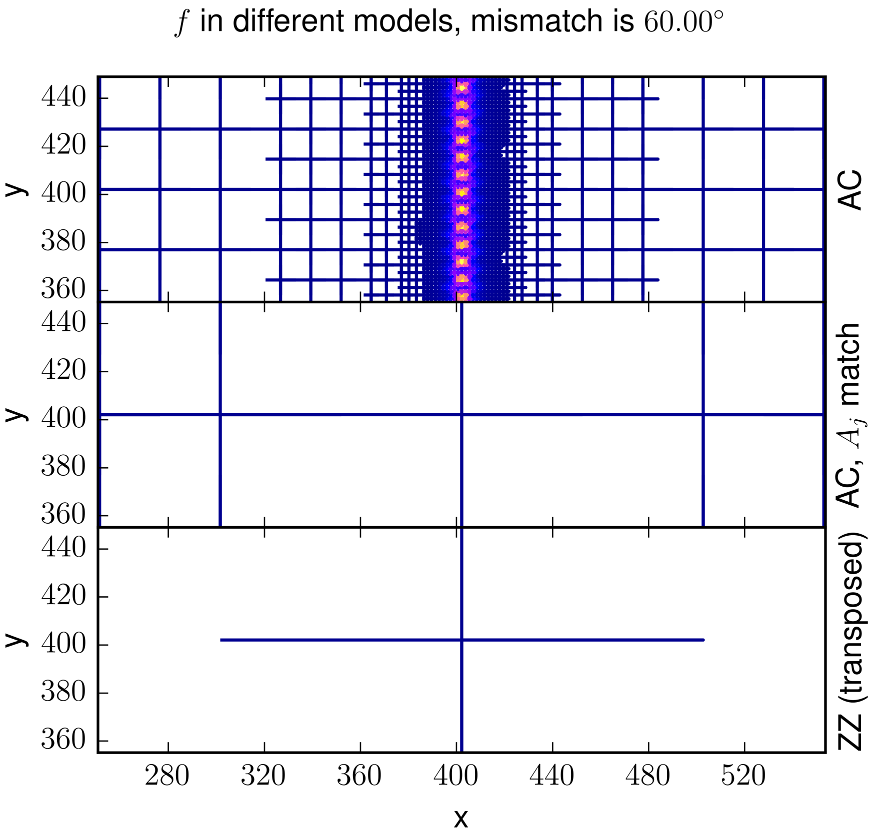

Figure 6.12: Grain boundary structure at 60.00° misfit.

Chapter 7

Dynamic grain rotation in the APFC model

This chapter introduces improvements to the amplitude expansion of the phase field crystal model (APFC) that enable simulations of grains rotating in the full range of possible rotations. A rotating circular grain is simulated, while some effects of the memory of the material can be observed in the simulation.

7.1 Introduction

The ability to predict the microstructure of material with a given chemical composition after different thermo mechanical processes is a key steps in the efficient design of modern materials. Since processes of forming the microstructure occur on length scales that are measured in microns, whereas the production of the material occurs in large batches, numerical methods able to consistently span the considerable differences in length scales are a tool of growing importance in materials modelling.

In past decades, several approaches to scaling different length scales were developed: the increasingly popular concept of integrated materials engineering (ICME) links material models at multiple scales hierarchically [3]. It can be used to connect models based on molecular dynamics or kinetic Monte Carlo on the atomistic scale with a phase field (PF) or cellular automata based model on the mesoscopic scale. While this approach is very useful, the discontinuous transitions between different length scales sometimes lead to problems that are hard to remove. Another popular approach to scaling the differences in length scales is the phase field method (PF) in combination with adaptive mesh refinement techniques, which was successfully applied to the study of microstructure evolution on spatial scales spanning several orders of magnitude [4, 70].

The PF method describes the material through a spatially-continuous order parameter corresponding to the phase of the material at various spatial points. As such, this method is not optimal for studying phenomena where the atomic arrangement is crucially important as the positions of individual atoms are averaged out. To preserve the information of the atomic arrangement and enable the study of related phenomena, the phase-field-crystal (PFC) methodology was introduced [5, 6]. The PFC model can be derived from classical density-functional theory under some assumptions [11], and is based on minimization of a free energy functional constructed in such a way that the ground state is a periodic function of space corresponding to the lattice of the crystal. The PFC method naturally incorporates crystal elasticity and various topological defects, and since being established has been extended to model multi component materials, materials with different crystal lattices [12, 14–17], incorporate acoustic waves [20] and spatial anisotropy [21], and include ferromagnetic [24] and ferroelectric [25] effects in multi-component materials.

Since the PFC model retains the information about the atomic arrangement through the calculated atomic density field, the density field variable is unsuitable for the mesh refinement because it describes a spatially oscillating field. To increase the amount of material that can be modelled and pave the way for a connection with the PF methods, the complex-amplitude expansion (APFC) of the PFC method was introduced by Goldenfeld *et al.* [7, 8]. Using a renormalization group based approach, it expresses the atomic density function of the PFC model as a sum of waves aligned with the vectors of the reciprocal lattice of the crystal. The dynamic equations then express the evolution of the complex amplitudes associated with the waves, therefore making them better suited for the application of adaptive mesh refinement techniques [9, 62]. The transition from the atomic density field to complex amplitudes introduces unphysical phenomena such as unphysical grain boundaries between grains, rotated by a crystal's symmetry rotation [10]. This problem limits the APFC's applicability model to processes where grain rotation occurs.

In our current work, we demonstrate improvements to the APFC model that enable APFC simulations in conditions where grains rotate by a full range of rotation. We simulate a single circular grain in a matrix, and impose the condition of constant rotation speed on the circular grain as a boundary condition. We compare the results obtained with the improved APFC model with those obtained using a classical PFC model, and find a good level of agreement between the observed phenomena, indicating the unphysical effects were successfully removed.

This work is organized as follows. The theoretical description of the PFC and APFC models used in the present work is outlined. Section 7.3 describes the new model, algorithm, and features of the chosen numerical approach. Section 7.4 presents the results of our simulations and, finally, concluding remarks are given in 7.5.

7.2 Models

7.2.1 PFC model

The PFC model is based on the minimization of free energy given by the functional derived by Elder *et al.* [5, 6]:

$$F = \int d\boldsymbol{x}\{\psi[r + (1 + \nabla^2)^2]\psi/2 + \psi^4/4\} \tag{7.1}$$

here given in dimensionless units where r is the dimensionless temperature proportional to the temperature difference to a critical temperature T_c. The dynamic equation for the atomic density field ψ is derived using

$$\frac{\partial \rho}{\partial t} = \Gamma \nabla^2 \left(\frac{\delta \mathcal{F}}{\delta \rho} \right) \tag{7.2}$$

and yields

$$\frac{\partial \psi}{\partial t} = \nabla^2 \{[r + (1 + \nabla^2)^2]\psi + \psi^3\} \tag{7.3}$$

The atomic density functions ψ at minimal free energy have different shapes depending on the parameter r and initial average atomic density. In 2D the solutions form three different phases [6]: liquid phase where $\psi = \overline{\psi}$ in the entire area, striped phase and crystalline phase where the solution forms a crystal lattice with honeycomb symmetry.

7.2.2 APFC model

The solid phase solution to the PFC equation has honeycomb symmetry and can be approximated in terms of the complex amplitudes A_j [7–9] as

$$\psi \approx \sum_{j=1}^{3} A_j e^{i\mathbf{k_j}\cdot\mathbf{x}} + \sum_{j=1}^{3} A_j^* e^{-i\mathbf{k_j}\cdot\mathbf{x}} + \overline{\psi} \tag{7.4}$$

where k_j are the reciprocal lattice vectors of a hexagonal crystal

$$\begin{aligned} \mathbf{k}_1 = &\quad k_0(-\boldsymbol{i}\sqrt{3}/2 - \boldsymbol{j}/2), \\ \mathbf{k}_2 = &\quad k_0\boldsymbol{j}, \\ \mathbf{k}_3 = &\quad k_0(\boldsymbol{i}\sqrt{3}/2 - \boldsymbol{j}/2), \end{aligned} \tag{7.5}$$

and k_0 is the wave number. Goldenfeld *et al.* derived the dynamic equations for the complex amplitudes [7, 8]:

$$\frac{\partial A_j}{\partial t} = \tilde{\mathcal{L}}_j A_j - 3A_j|A_j|^2 - 6A_j \sum_{k:k\neq j} |A_k|^2 - 6\overline{\psi} \prod_{k:k\neq j} A_k^* \tag{7.6}$$

where $k, j \in [1, 3]$,

$$\tilde{\mathcal{L}_j} = (1 - \nabla^2 - 2i\mathbf{k}_j \cdot \nabla)(-r - 3\overline{\psi}^2 - \{\nabla^2 + 2i\mathbf{k}_j \cdot \nabla\}^2) \tag{7.7}$$

is a rotationally covariant operator and $\overline{\psi}$ is the dimensionless average density.

The free energy of the system in terms of the complex amplitudes was derived by Chan and Goldenfeld [61]

$$\begin{aligned} F/k_{APFC} = &\quad -\sum_{j=1}^{3} A_j^*(-r - 3\overline{\psi}^2 - \{\nabla^2 + 2i\mathbf{k}_j \cdot \nabla\}^2)A_j \\ &\quad +3\sum_{j,l=1}^{3} |A_j|^2|A_l|^2 - \frac{3}{2}\sum_{j=1}^{3} |A_j|^4 \\ &\quad +6\overline{\psi}(A_1A_2A_3 + A_1^*A_2^*A_3^*) \end{aligned} \tag{7.8}$$

where k_{APFC} is a constant we used to fit the grain boundary energies of the APFC model to those of the PFC model and is normally equal to 1.

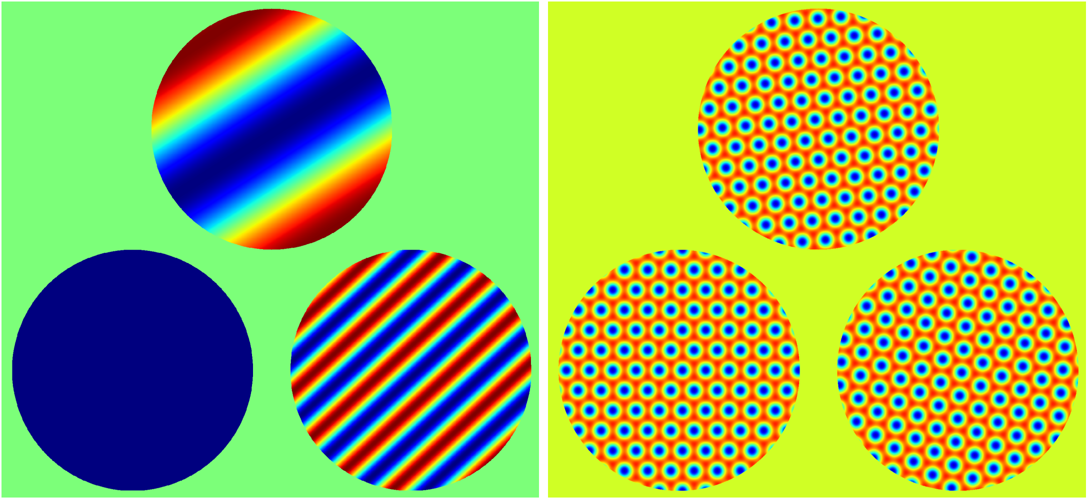

Figure 7.1: The images show the phenomenon of beats in misaligned grains: (a) real component of the first complex amplitude $\Re(A_1)$; and (b) the reconstructed atomic density field ψ in three seeds, rotated by (clockwise from bottom left) $\theta = 0°$, $5°$, and $25°$.

Multiple orientations of the crystal grains can be modelled using only one set of basis vectors due to the rotational covariance of the operator $\tilde{\mathcal{L}}_j$.

The rotation of the grains in the complex amplitudes representation is represented by the so called beats in the complex amplitudes of the grains, not aligned with the initial choice of the basis vectors [7, 9]. Figure 7.1 shows the phenomenon of beats in three grains rotated by 0°, 5°, and 25°.

The phenomenon of beats mean that the adaptive mesh refinement (AMR) techniques applied to APFC models are ineffective because in rotated grains the mesh must be refined in order to properly resolve the considerable variations in the complex amplitudes due to the beats. To solve this problem and enable AMR techniques to work in APFC models, two approaches have emerged.

Athreya *et al.* [9] combined the Cartesian representation of the complex amplitude equations with the polar representation in a hybrid formulation and evolved the complex amplitudes in their polar representation within the rotated grains.

The present authors proposed an approach using an auxiliary local rotation field variable that tracks the location of the local grain in combination with an exploit of the rotational covariance of the complex amplitude equations [62]. This approach allowed for the rotation of the local grain to be separated from the complex amplitude equations, virtually aligning the basic vectors with the rotation of the local grain at all computational points.

In addition to enabling AMR techniques to perform well inside rotated grains, the local rotation field can be exploited to sidestep the problem of an unphysical grain boundary occurring between grains rotated by a multiple of the crystal's symmetry rotation, first described by Spatched *et al.* [10]. This problem originates in the complex amplitudes representation of a grain, rotated by a crystal's symmetry rotation (60° for triangular symmetry) not being the same as the representation of a non-rotated grain, even though both grains physically represent the same crystal rotation. In order to overcome this problem, the authors of this contribution proposed to combine the local rotation field with an amplitude-matching algorithm that correctly matches the complex amplitudes on both sides of an inter-grain boundary based on the physical directions of the local grain's underlying basis vectors in works described in Chapters 5 and 6.

7.3 Numerical methods

To compare the new results with existing models, we matched the parameters of the PFC and APFC models as closely as possible. The common parameters were $\overline{\psi} = 0.285$, $r = -0.25$. We simulated the PFC model (eq. (7.3)) using a finite difference computation scheme with time step $dt = 0.001$ and spatial discretization $dx = k_X l_{PFC}\pi/4$, $dy = l_{PFC}\pi/4$ $N_x = N_y = 512$, where the numeric constant ($k_X = 1.01036$) in dx was used to precisely match the matrix's periodicity in x direction and l_{PFC} is a constant capturing the unit cell size of the PFC model compared with the 1-mode solution, obtained with a minimization method ($l_{PFC} = 0.97453$).

The APFC model (eq. (7.6)) was solved on an adaptive grid with time step $dt = 0.04$ and minimal grid spacing $dx = \pi/2$ and size $L = 256\pi/2$, as described in our previous work [62] (described in Chapters 5 and 6). The algorithm solves the complex amplitude equations in the Cartesian representation using an auxiliary local rotation field to align the basis vectors with the local grain at all calculation points, further additionally uses the local-rotation information to match the correct complex amplitudes A_j in neighboring computation nodes, as illustrated in Fig. 7.2.

All simulations were performed using periodic boundary conditions. In dynamic simulations of a rotating grain, a circular grain was placed inside the matrix, with the entire simulation domain initialized to a 1-mode solution of the PFC equation at $t = 0$.

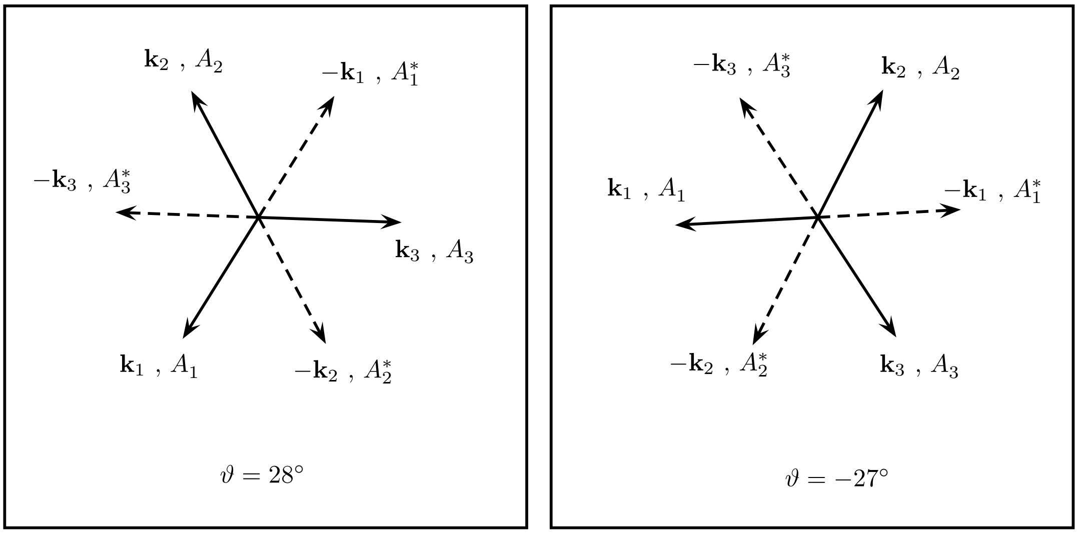

Figure 7.2: Wave vectors in two neighboring computational nodes with different local rotations (left: $\vartheta = 28°$, right: $\vartheta = -27°$). The algorithm matches the complex amplitudes in neighboring computation nodes that correspond to wave vectors pointing in the most similar directions. A_1 in the left node is matched with A_2^* in the right node, as the angle between these two wave vectors is only 5°.

The inside of a circular grain was then fixed to this 1-mode solution, when the matrix outside of the grain was left to relax into the minimal free-energy configuration until $t = 40$. After this time, the circular grain was periodically rotated at a specified rotation speed, while outside of the circular grain normal evolution equations were applied. The rotating circular grain was treated as a boundary condition and therefore the free energy inside it was not changed during the simulation run. In static simulations, the setup was similar with a circular grain of exactly the same radius in the center of the matrix, rotated by a specified angle at the start of the simulation. To enable the free energies obtained in simulations to be compared, the free energy inside the grain was fixed in this case as well. Before the start of the simulation, a small area of the matrix around the circular grain was melted, and the crystal was left to grow into a free-energy optimal configuration during the simulation.

As the lattice constant in PFC and APFC models differs by a factor l_{PFC}, the radiuses of the circular grains in compared simulations were also corrected by this factor in order to preserve the same configuration of atoms at the boundary between the imposed atomic configuration of the circular grain and the matrix. In the PFC model, the optimal atomic configuration differs from the 1-mode solution imposed on the boundary of the circular grain, also creating some differences in the results of the two models. Since the PFC and APFC models give different grain boundary energies, we used k_{APFC} in eq. (7.8) to fit the grain boundary energies of the APFC model to the grain boundary energies of the PFC model. We calculated the grain boundary energies of a symmetric tilt grain boundary at 3.8902° in the same way as described in Chapter 6. with both models and obtained $\gamma_{PFC,3.8^\circ} = 0.004819$, $\gamma_{APFC,3.8^\circ} = 0.006013$. Based on this, we set $k_{APFC} = \gamma_{PFC,3.8^\circ}/\gamma_{APFC,3.8^\circ}$.

7.4 Results

Figure 7.3 shows an example of different structures forming around a circular grain rotated by 10° in the PFC (left column) and APFC (right column) models. The first row presents the microstructure around a static circular grain. The second row of the figure presents the microstructure around a dynamically rotating grain (the rotation period is $t_0 = 200000$) when the grain is rotated by 10°. The structure differs from the static configuration because the dynamic rotation meant the grain boundary could not relax into the lowest energy configuration. The third row in the figure presents the microstructure from the same simulation as shown in the second row at a time when the grains are rotated by 70°. We may observe the structure is different from the structure observed at a 10° rotation, which is due to the history of the sample. Both models show that at 70° the ring of dislocations remaining from the first rotation round is pushed outwards, while a new ring is formed on the edge of the central grain, which is frozen in structure while being rotated. This phenomenon is present in all cases where the rotation is slow enough for it to occur while the size of this effect depends on the rotation speed (the lower the speed, the more information that can be preserved about the sample's history).

Figure 7.4 shows the grain boundary free energies of rotated grains. The APFC model does not show artifacts of an unphysical grain boundary which would increase the free energy of the grain boundary at rotation angles above 30° to unphysically high levels. Statically rotated grains show the same grain boundary free energies for angles α and $60^\circ - \alpha$, which confirms that the unphysical grain boundary was removed in the APFC model. Since the grain size is small, the calculated free energy of the grain boundary depends strongly on the exact atomic structure at the distance of the radius from the center of the atomic lattice. The radiuses of the grains are too small for the

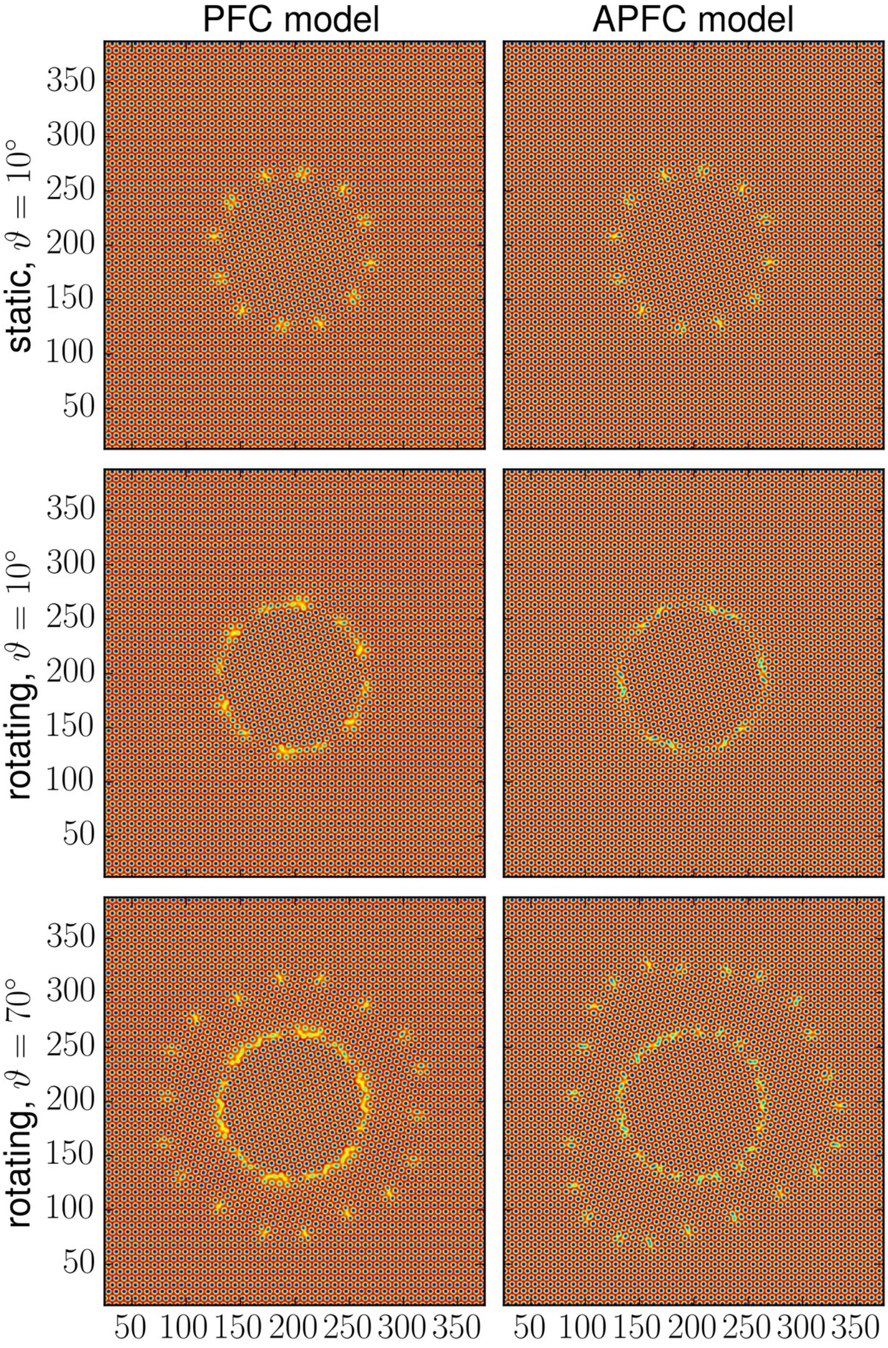

Figure 7.3: The images show the microstructure surrounding a rotated circular grain in the PFC (left column) and APFC (right column) models. The first row shows the microstructure around a static grain rotated by 10°. The second row shows the microstructure from a simulation with a dynamically rotating grain (rotation period $t_0 = 200000$) when the rotation of the grain matches 10°. The third row shows the microstructure after the same seed as in the second row was rotated by 70°. Since the rotational symmetry of the triangular crystal lattice equals the difference of the rotations in the last two rows, the difference in microstructure in the last two rows is due to the memory effects in the material. For better comparison, the size of the APFC model plots was scaled with l_{APFC}, like elsewhere in the present work.

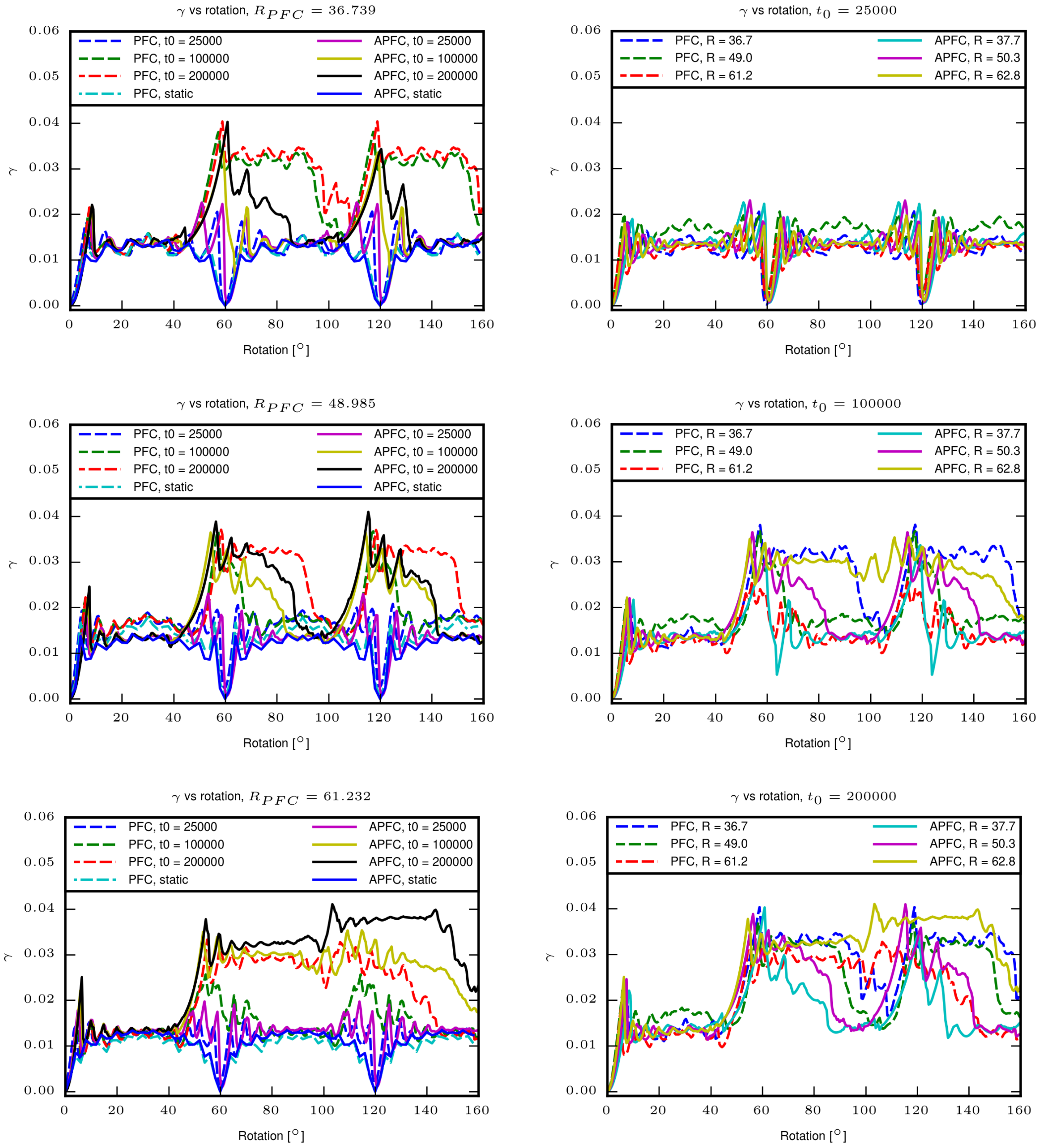

Figure 7.4: Free energy of the grain boundary formed around a rotating circular grain. The memory effect, observed by an increase in the grain boundary free energy in the second rotation period ([60°, 120°]) compared with the first period ([0°, 60°]), increases with a longer period of rotation of the grains (t_0) in both models. Due to the small size of the rotating grains, the exact atomic structure at the grain boundary has a large effect on the final grain boundary free energy, bringing the result that the grain with medium radius ($R = 49.0$) has the grain boundary with the highest free energy of all grains with the same rotation period in the PFC model. For static configurations simulations were performed only for rotation angles [0°, 60°] and were periodically repeated in the graphs.

discretization effects to be averaged out. Accordingly, the calculated free energy for the middle of three selected grain radiuses ($R = 49.0$) exceeds that of the other two selected grain radiuses. With increasing grain radius, the discretization effects should disappear. As this would also considerably increase the simulation times, smaller radiuses were chosen since the aim of the comparison was to qualitatively compare the two models in a setting with dynamical grain rotation, and the small grain size was sufficient for demonstrating the improved model's ability to perform well in such conditions.

Both models show qualitatively the same effects of increasing the grain rotation time (t_0) and dependency of the grain boundary energy on the rotation angle. At fast rotation speeds ($t_0 = 25000$), the atomic structure does not have enough time to find a free energy minimal configuration before the seed is again rotated and the most energetically favorable configuration changes. The grain boundary therefore has a structure that has only partially relaxed from an imposed configuration into an energetically more favorable configuration and does not exhibit any memory effects. The grain boundary structures are presented in Fig. 7.5. At slow rotation speeds ($t_0 = 200000$), the atomic structure relaxes into a local free energy minimum before the grain is sufficiently rotated to change the free energy minimal configuration. The atomic configuration around the grain boundary therefore keeps some memory of the past configurations since the current configuration represents a local minimum closest to the previous local free energy minimum. Due to this material memory effect, the grain boundary does not disappear when the grain is rotated by the crystal's symmetry rotation ($60°$). The free energies of the rotating grains show an increase in the free energies in the second rotation period ($60° - 120°$) for slowly rotating grains. This is due to the first ring of the dislocations that formed in the first rotation period ($0° - 60°$) not being annihilated upon completion of the rotation period (at the rotation $60°$ of the crystal's symmetry) but being instead pushed outwards with a new ring of dislocations forming inside the first ring, as presented in Fig. 7.6. This phenomenon is observed in both models. At some rotation α above $60°$, the two rings of dislocations partially annihilate each other and the free energy drops to similar values as observed in the first rotation period. The delay of this effect ($\alpha - 60°$) increases with the length of the rotation period since with a decrease of rotation speed the microstructure is not perturbed as much with the imposed rotation and stays at the same gradually changing local free energy minimum.

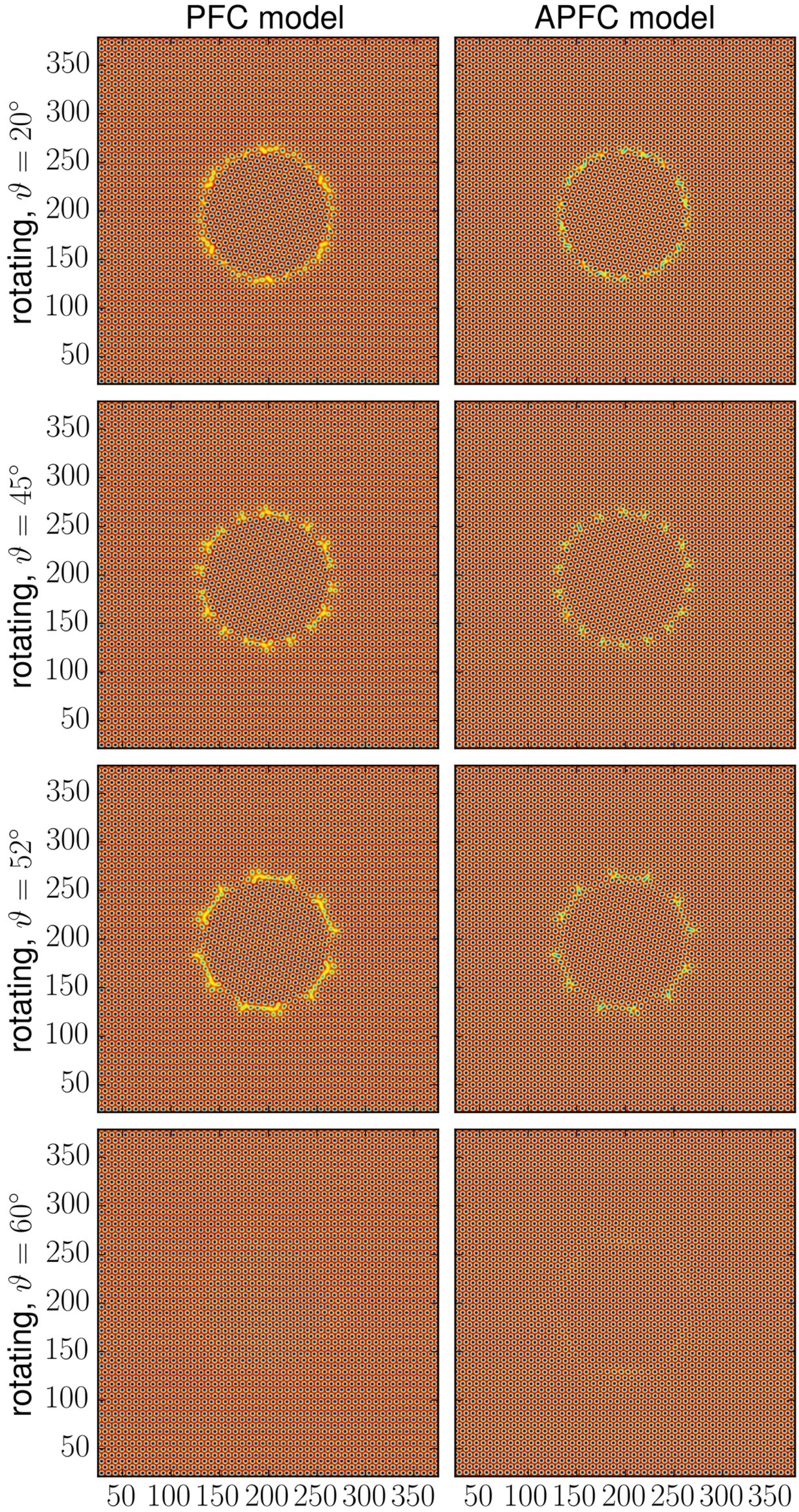

Figure 7.5: Grain boundary structures around a rotating grain. The grain rotates fast ($t_0 = 25000$), therefore the atomic structure on the grain boundary does not relax far from the imposed configuration and does not remember the past. The images in the rows show the microstructure calculated with the PFC (left column) and APFC (right column) models when the grain is rotated by 20°, 45°, 52°, and 60°.

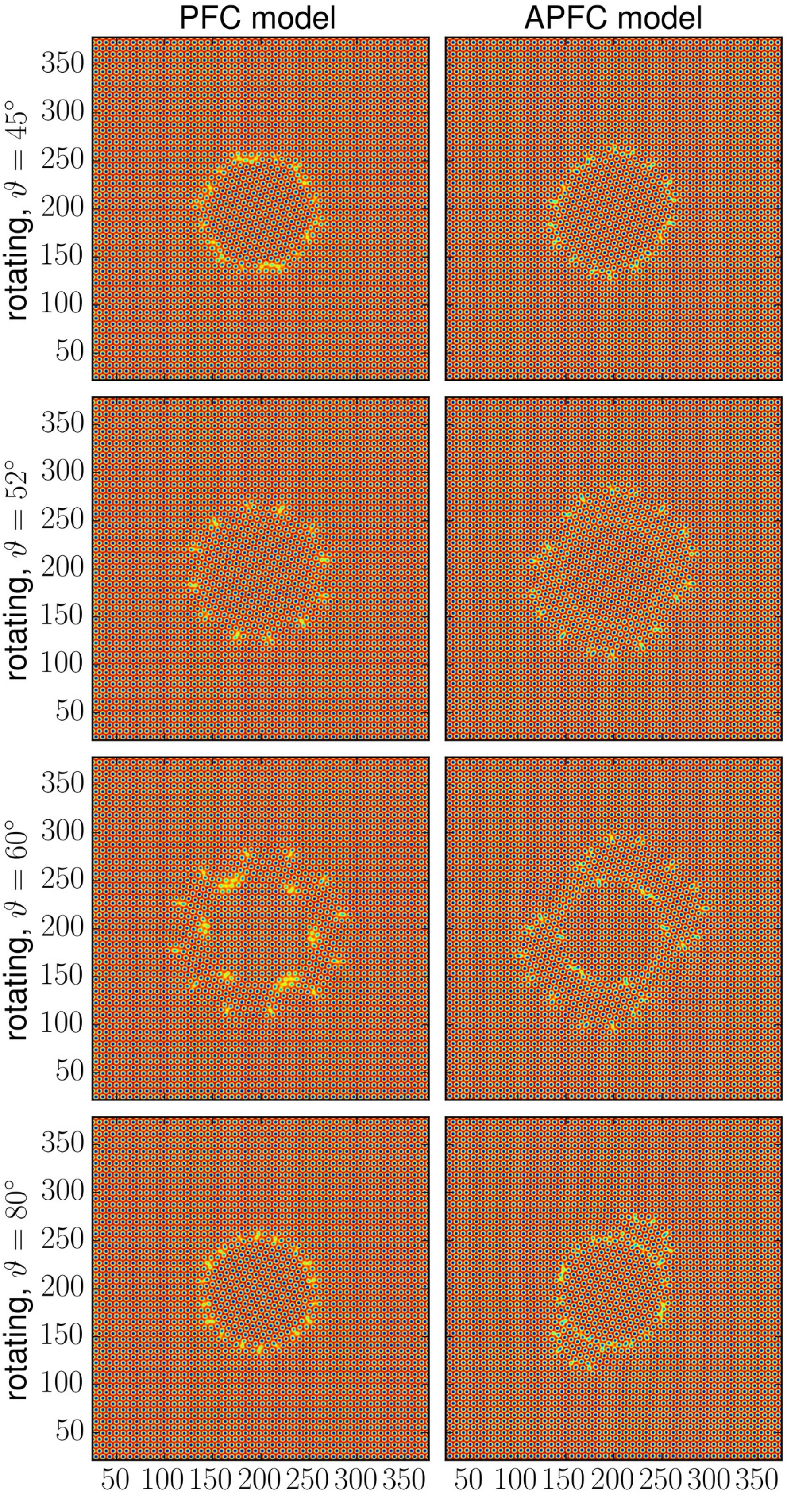

Figure 7.6: Grain boundary structures around a rotating grain. The grain rotates slowly ($t_0 = 100000$), therefore the atomic structure on the grain boundary relaxes into the new local free energy minimum before the grain is rotated; the microstructure thus reflects the past free energy minimal configurations. The images in rows show the microstructure calculated with the PFC (left column) and APFC (right column) models when the grain is rotated by 45°, 52°, 60°, and 80°.

7.5 Summary and conclusion

The development and transformation of the microstructure in our chosen dynamic process show the same effects in the PFC and APFC models, thereby assuring that our improvements to the APFC model may be used in simulations of processes that include dynamic changes in grain rotation, without the effects of an unphysical grain boundary.

Our improvements to the APFC model enable microstructure modelling for larger sizes of material during industrially important processes where grain rotation occurs. Enabling AMR algorithms to efficiently focus the computational power in the areas around the grain boundaries a key step in efficiently modelling microstructure development in larger simulation domains, while with our improvements the use of AMR is not hindered by an artificial grain boundary.

We chose the problem of a single circular grain that is forcibly rotated in an unperturbed matrix as the simplest possible example to verify the new model's behavior in conditions of dynamically rotating grains. This example model also appears to demonstrate some effects of material memory which could be further analyzed. Due to limited computational resources, we chose the smallest grain sizes that would allow us to check our APFC model's behavior. Unfortunately, the very small grain sizes do not allow us to deduce much about the effects of material memory due to the free energy's great dependence on the exact configuration of the atoms at the cut-off grain boundary on the edge of the rotating grain. Increasing the grain sizes would solve this problem and allow investigation of the memory effects in the material using a simple simulation setup.

7.6 Appendix A: Comparing selected simulations

This section presents a selected set of simulations for use in understanding the differences/similarities in the observed microstructures of rotating grains. The microstructure is presented at 8 different grain rotations, the even pages showing the PFC model and the odd pages showing the APFC model. When static configurations are shown, the configurations for rotation angles exceeding $\vartheta = 60°$ present the results obtained for angles $\vartheta_{calculation} = \vartheta \ modulo \ 60°$, and are presented at the same location on the pages so that a comparison can easily be made with microstructures, obtained from simulations of rotating grains.

The first set of Figures 7.7-7.12 presents grains in static configurations. The images at $\vartheta = 56°$ reveal some of the reasons the results calculated for the grain boundary free energies vary much too much to allow a good generalization of the results. The rotated grain observed at a small radius $R = 36.7$ does not even form any dislocations. At a medium radius $R = 49.0$, the deformation is spread over the entire grain perimeter, increasing the grain boundary energy. At the largest radius $R = 61.2$, the deformation is condensed in 6 dislocations, which lowers the calculated grain boundary energy.

For a slowly rotating grain ($t_0 = 100000$), the dislocations formed on the grain boundary are slowly pushed outwards in all cases. Above the crystal's symmetry rotation angle of 60°, another ring of dislocations forms within the ring of existing dislocations and is again pushed outwards. At some even larger rotation both groups of dislocations at least partially annihilate each other. This phenomenon is observed in all simulations. When the grain is rotating too fast, the dislocations do not travel far out and are immediately annihilated by the newly forming dislocations, and the structure of two rings of dislocations therefore does not form. The angle at which the dislocations annihilate or when the second set of dislocations forms also differs among the models, with grain rotation period t_0, and with grain radiuses.

Overall, our simulations demonstrate the new model's feasibility for simulating phenomena with rotating grains. We can also observe that, in order to draw general conclusions about how the rotation time affects the memory of the material, simulations using bigger grains are required. Qualitatively matching phenomena are observed in both models, giving assurance that the new model does not introduce unexpected numerical errors into the calculations.

The simulations show static grains of all three chosen radiuses simulated with the PFC and APFC models. A slowly rotating grain ($t_0 = 100000$) is shown with the largest and smallest of the selected radiuses, simulated with both the PFC and APFC models. A fast rotating grain ($t_0 = 25000$) is shown only with the largest of the selected radiuses, simulated with both the PFC and APFC models.

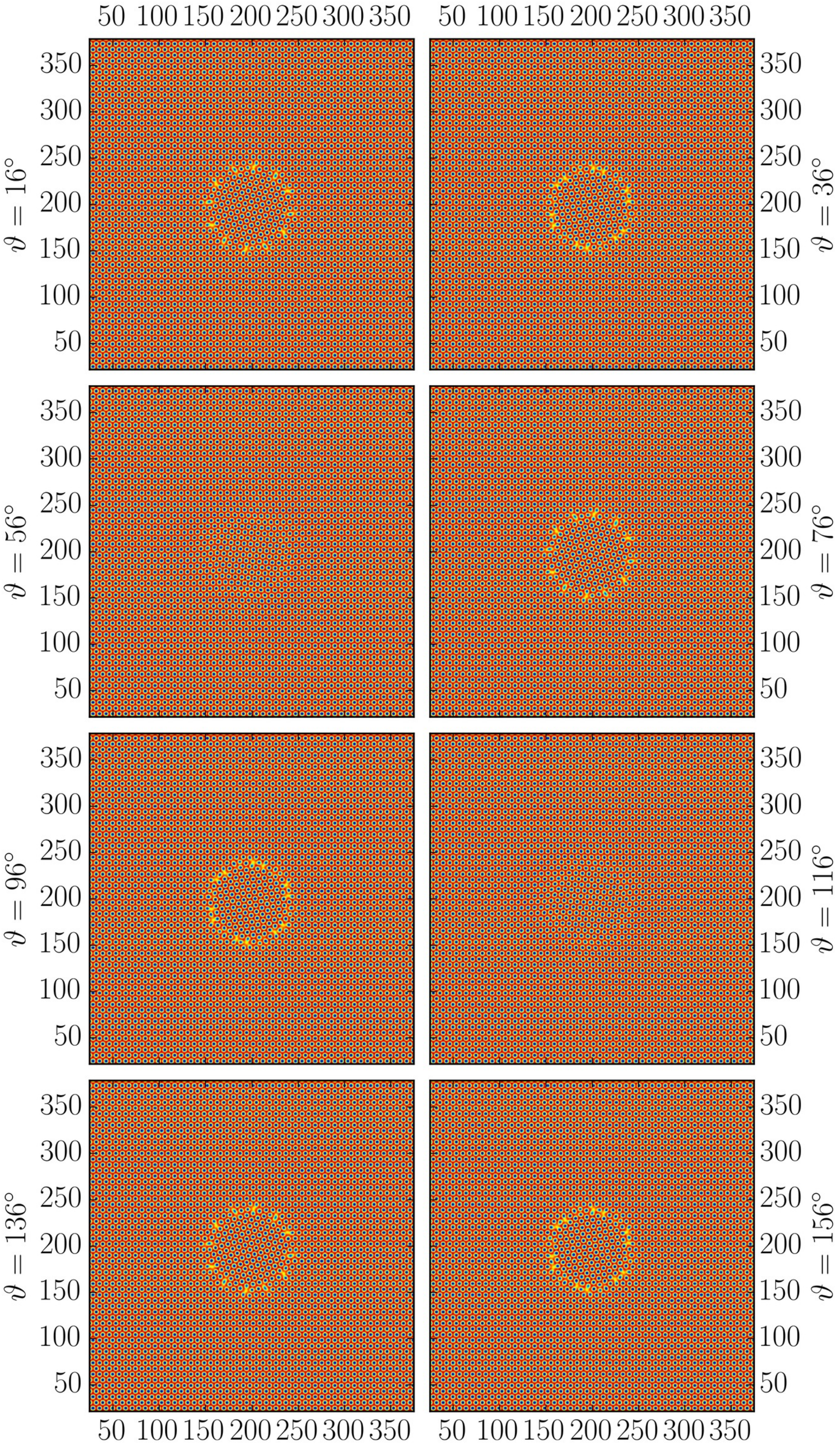

Figure 7.7: Microstructure in the PFC model at selected rotations. Static grain with $R_{PFC} = 36.7$.

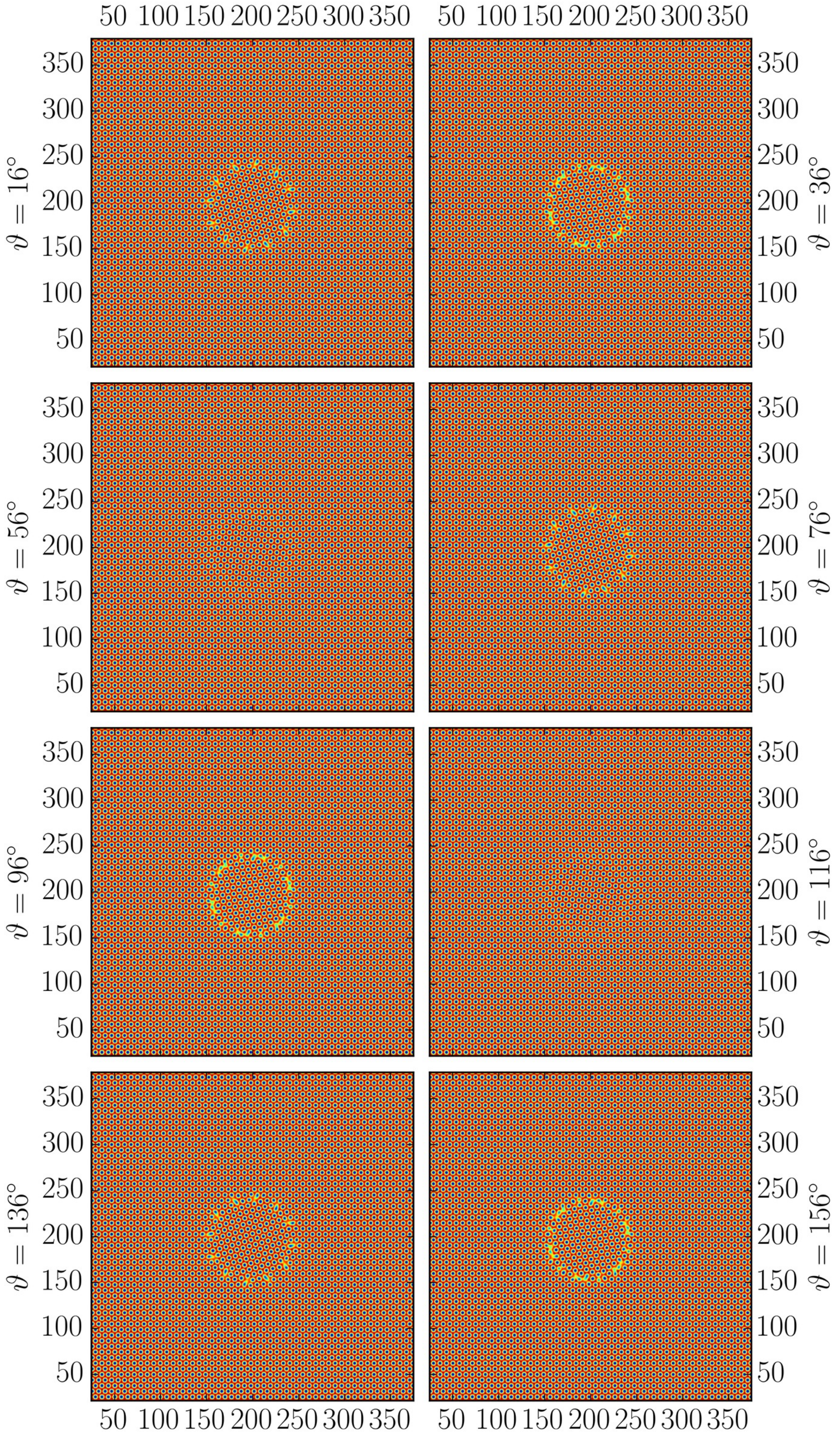

Figure 7.8: Microstructure in the APFC model at selected rotations. Static grain with $R_{PFC} = 36.7$.

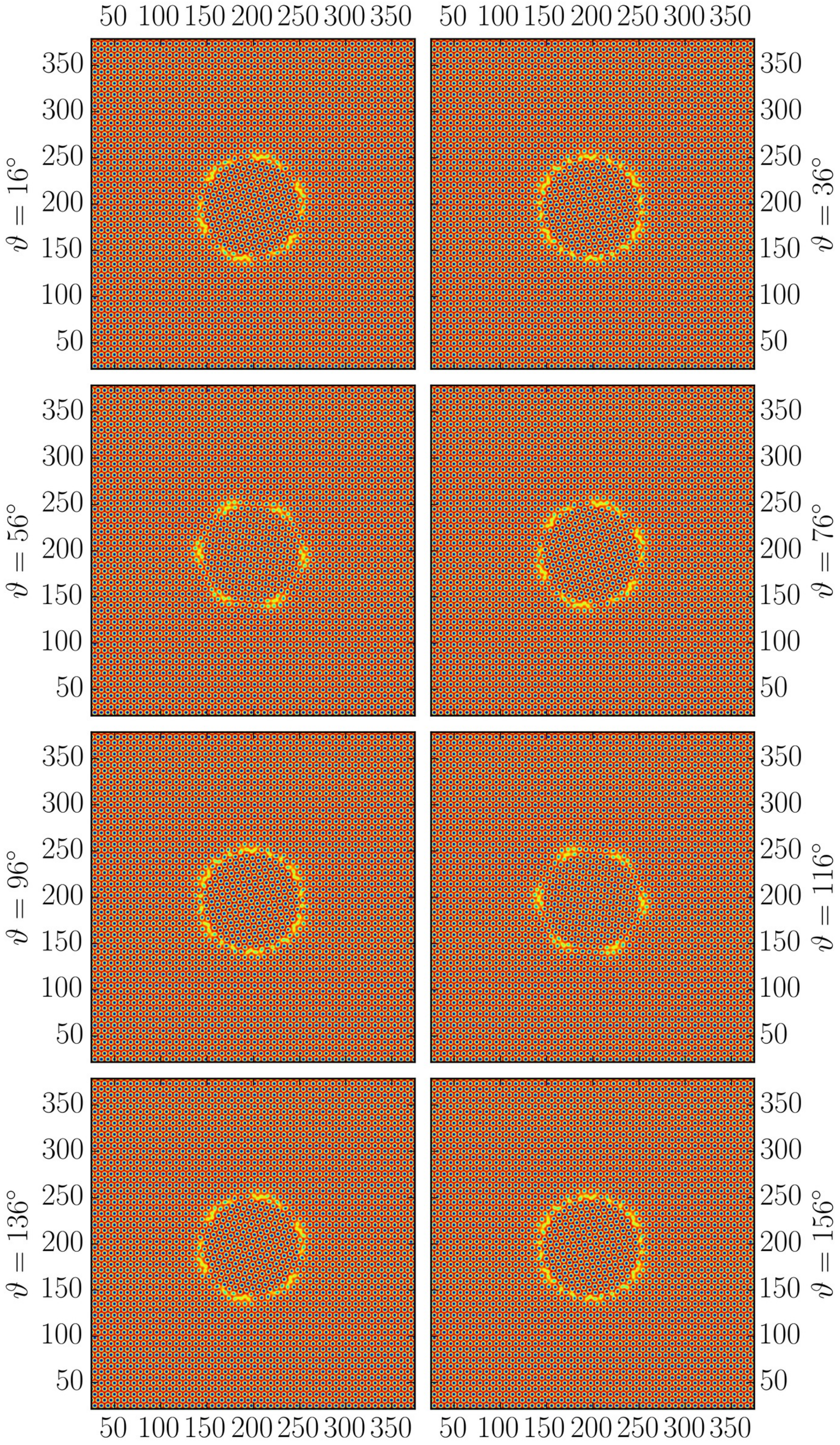

Figure 7.9: Microstructure in the PFC model at selected rotations. Static grain with $R_{PFC} = 49.0$.

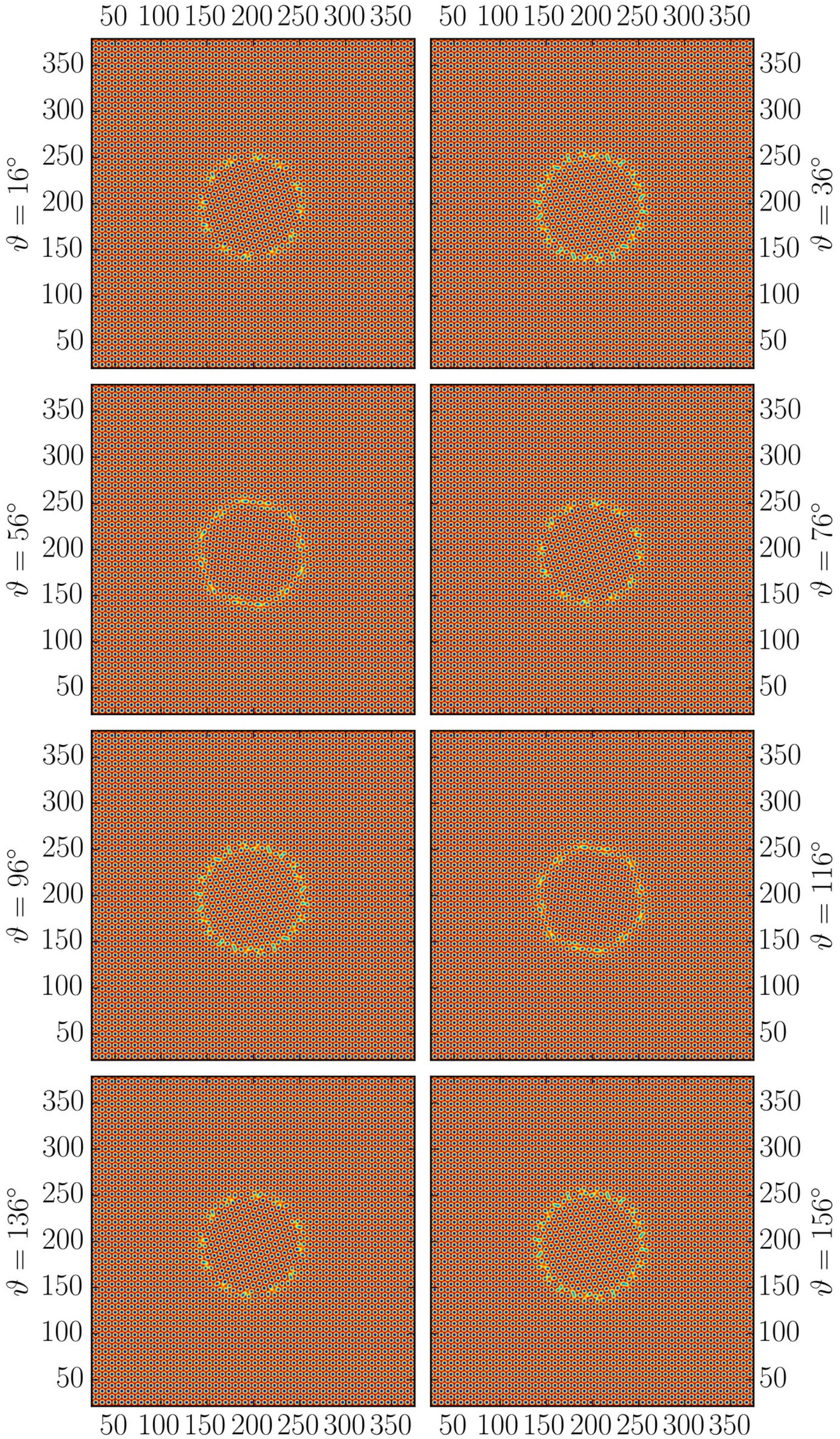

Figure 7.10: Microstructure in the APFC model at selected rotations. Static grain with $R_{PFC} = 49.0$.

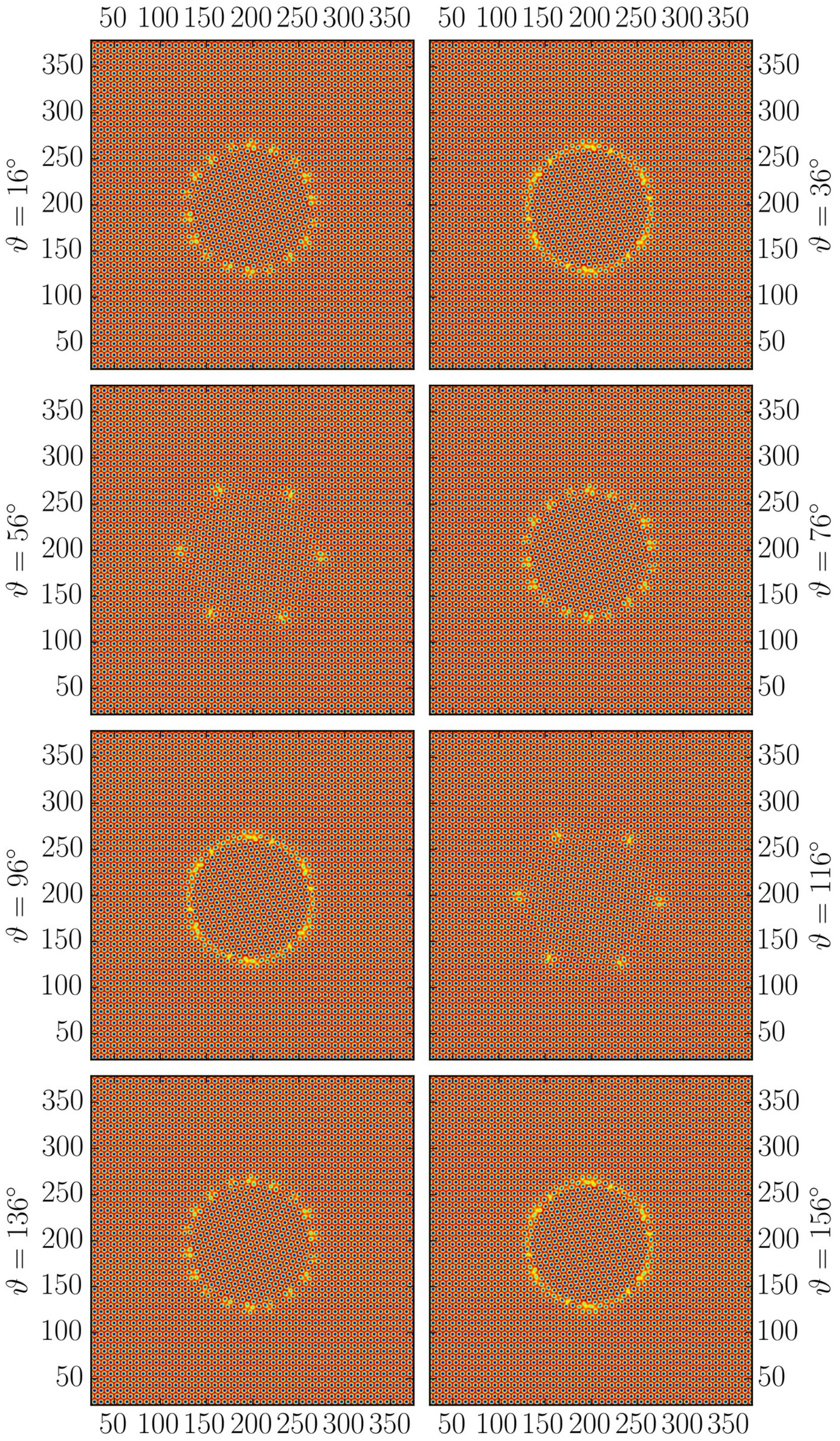

Figure 7.11: Microstructure in the PFC model at selected rotations. Static grain with $R_{PFC} = 61.2$.

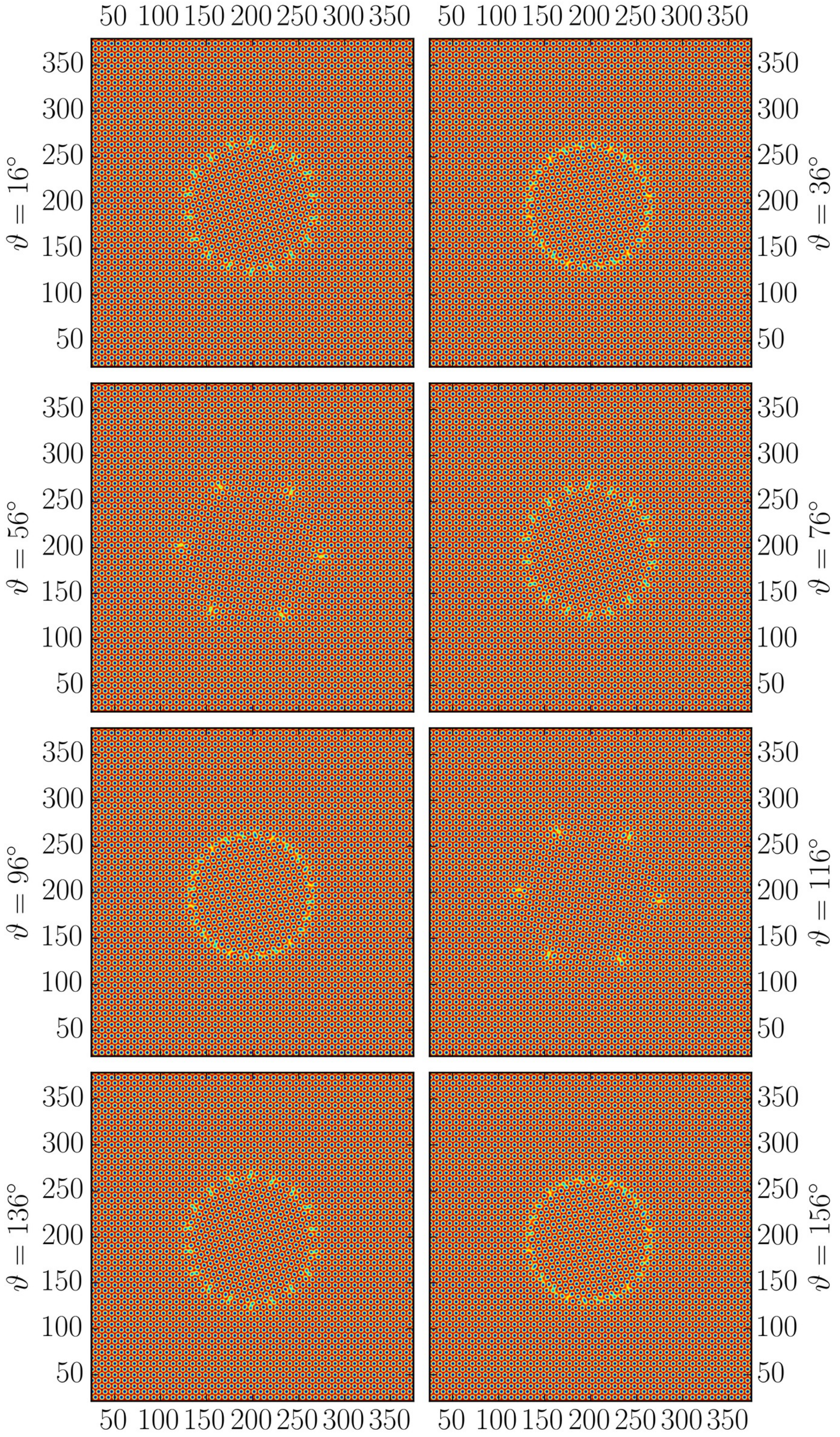

Figure 7.12: Microstructure in the APFC model at selected rotations. Static grain with $R_{PFC} = 61.2$.

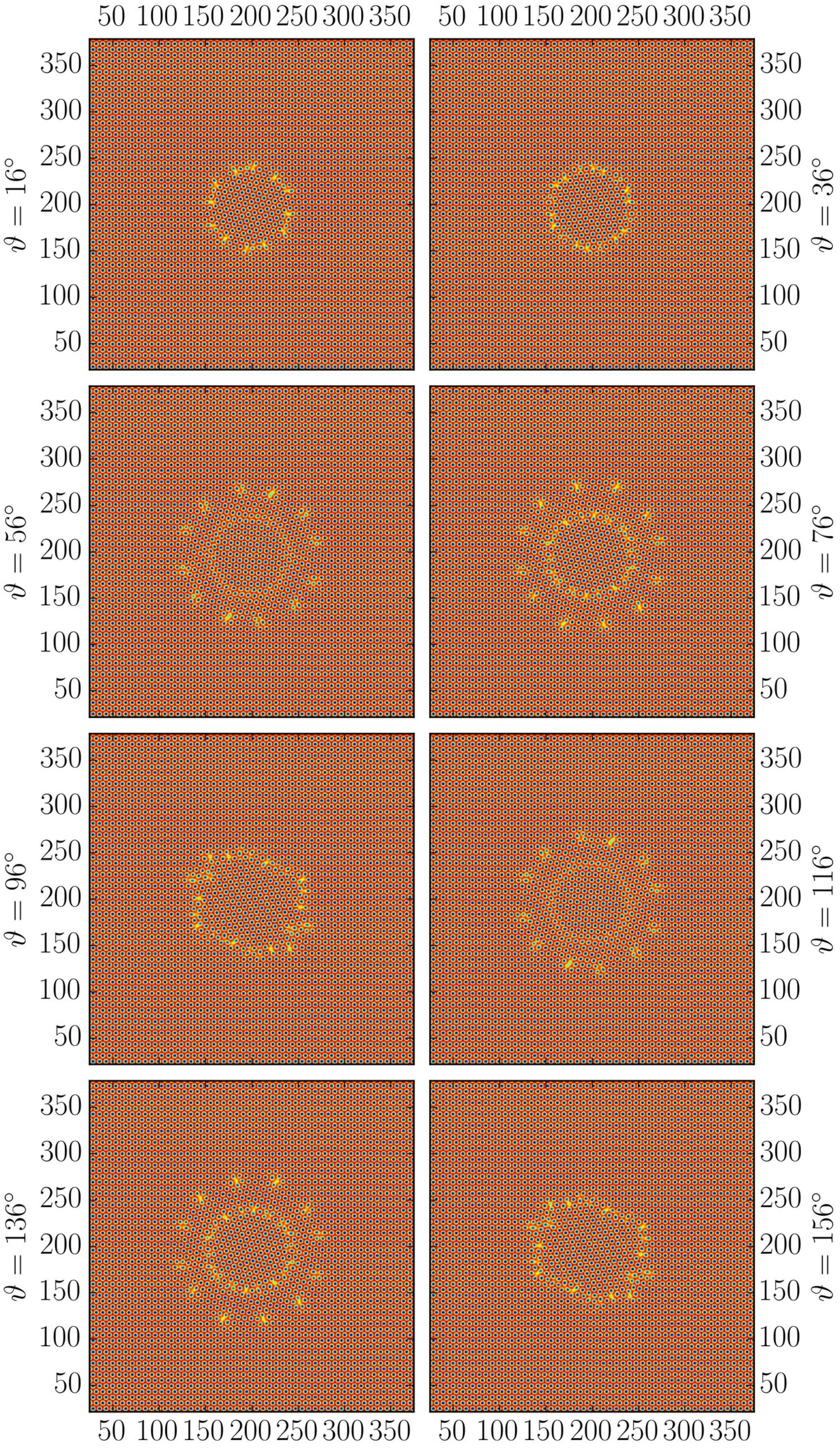

Figure 7.13: Microstructure in the PFC model at selected rotations. Rotating grain with $t_0 = 100000$ and $R_{PFC} = 36.7$.

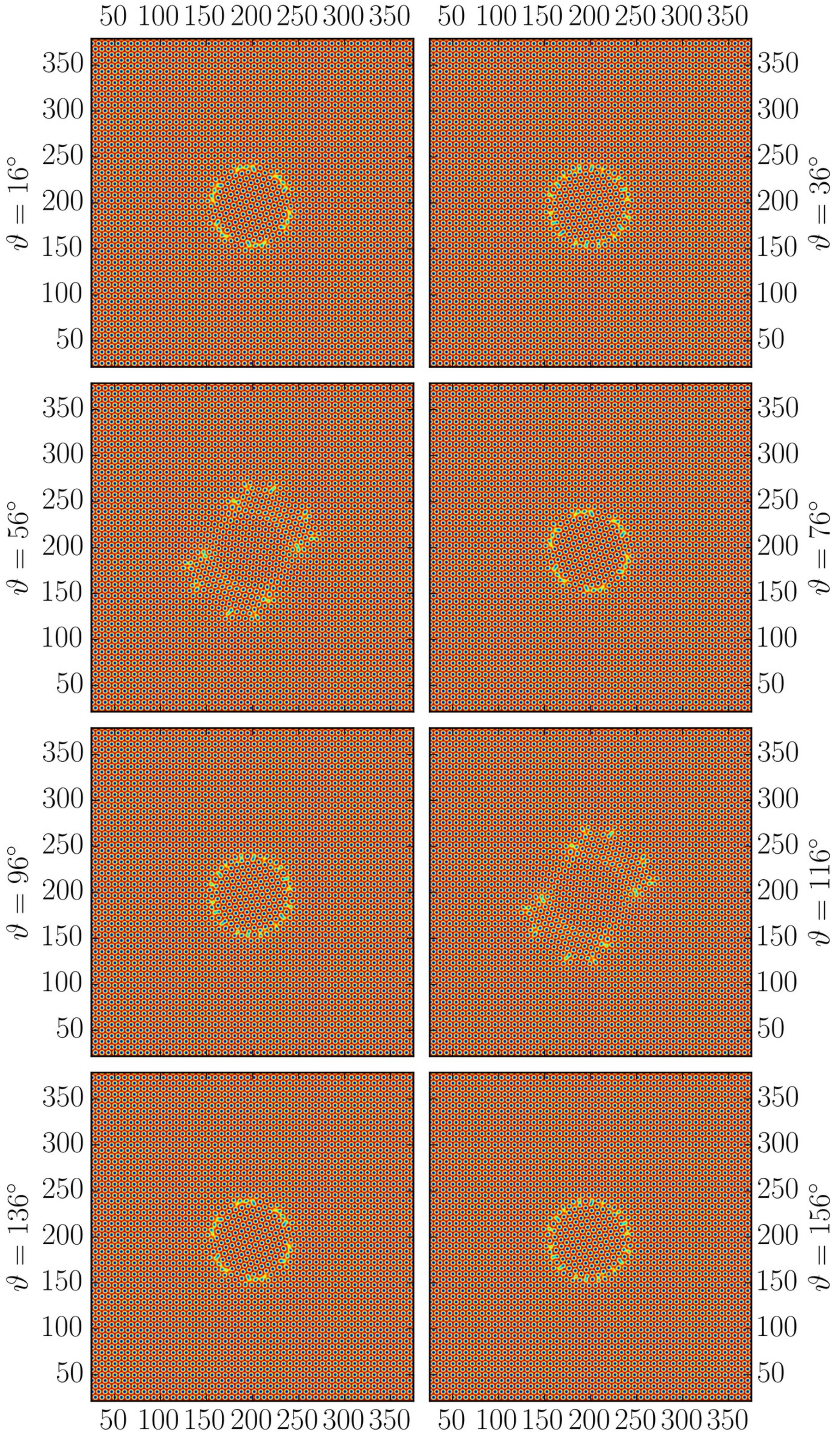

Figure 7.14: Microstructure in the APFC model at selected rotations. Rotating grain with $t_0 = 100000$ and $R_{PFC} = 36.7$.

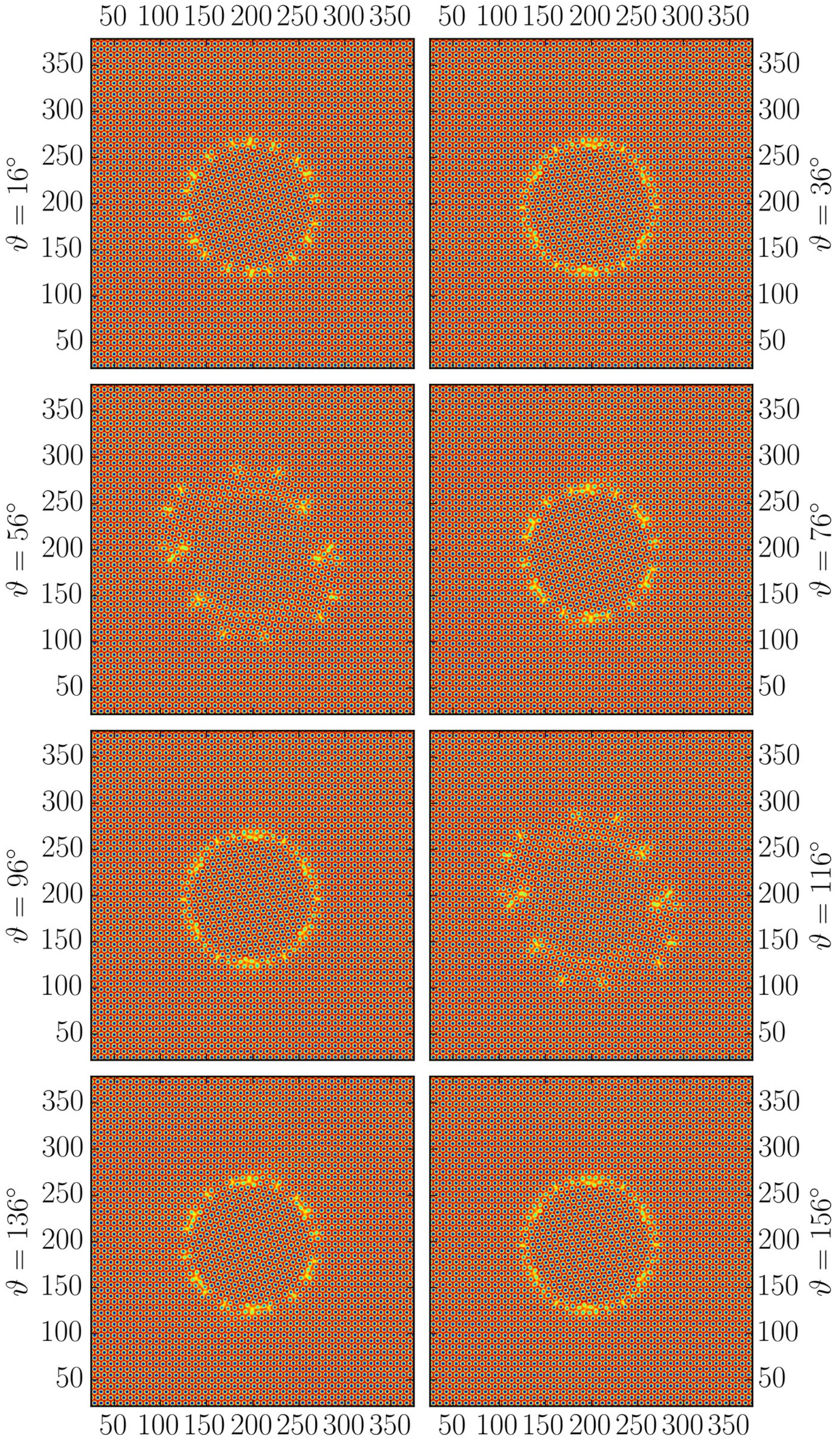

Figure 7.15: Microstructure in the PFC model at selected rotations. Rotating grain with $t_0 = 100000$ and $R_{PFC} = 61.2$.

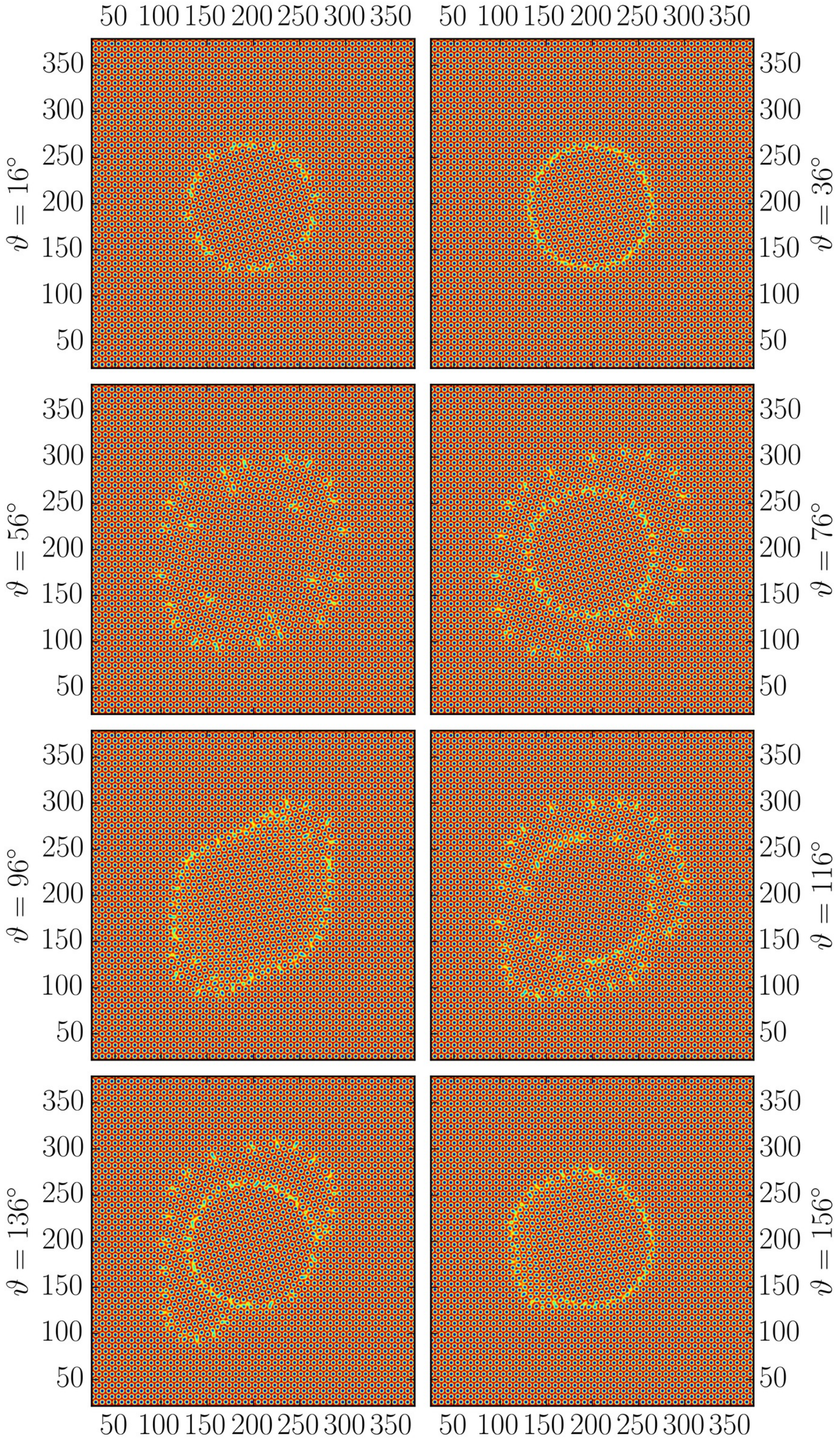

Figure 7.16: Microstructure in the APFC model at selected rotations. Rotating grain with $t_0 = 100000$ and $R_{PFC} = 61.2$.

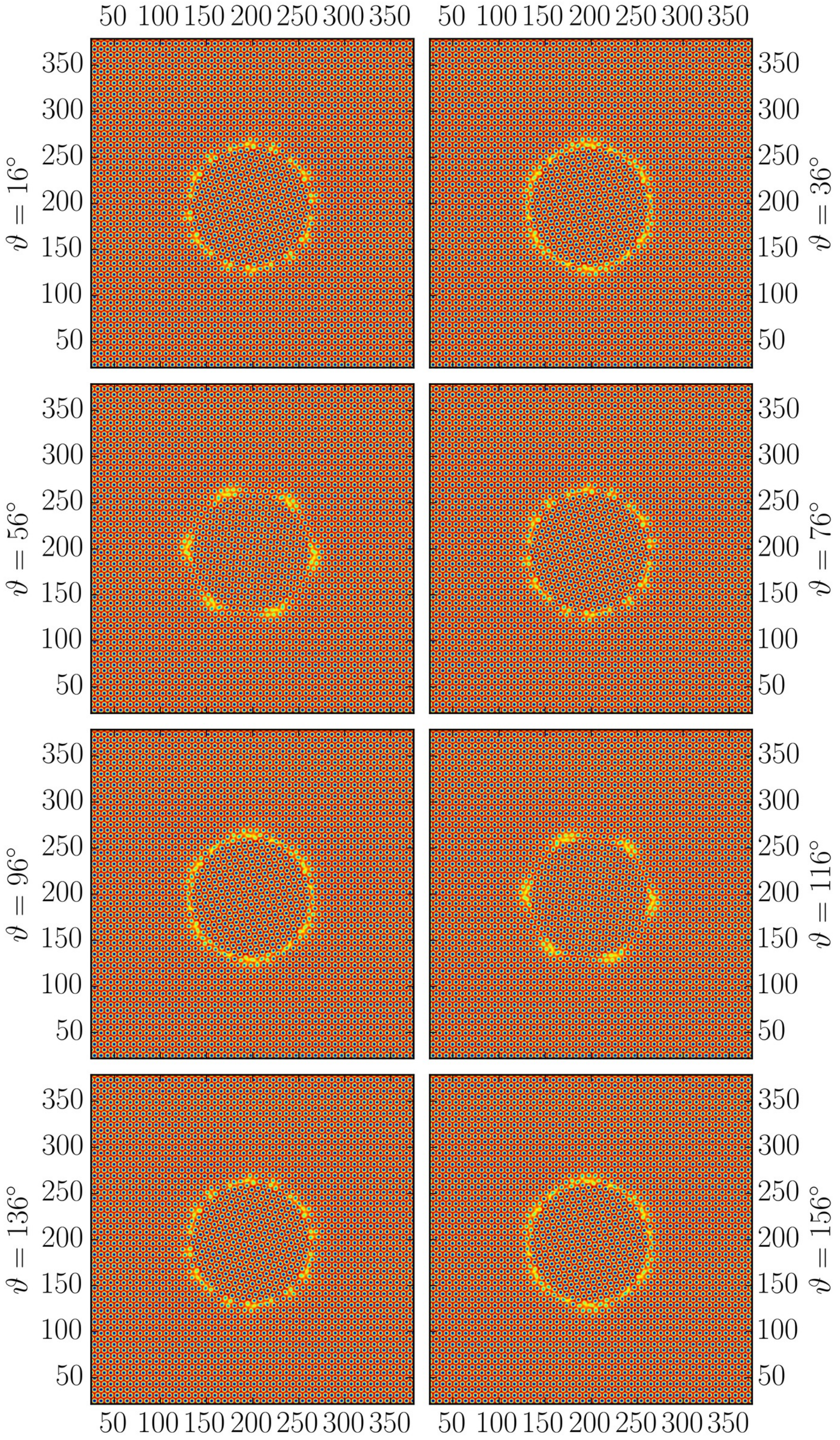

Figure 7.17: Microstructure in the PFC model at selected rotations. Rotating grain with $t_0 = 25000$ and $R_{PFC} = 61.2$.

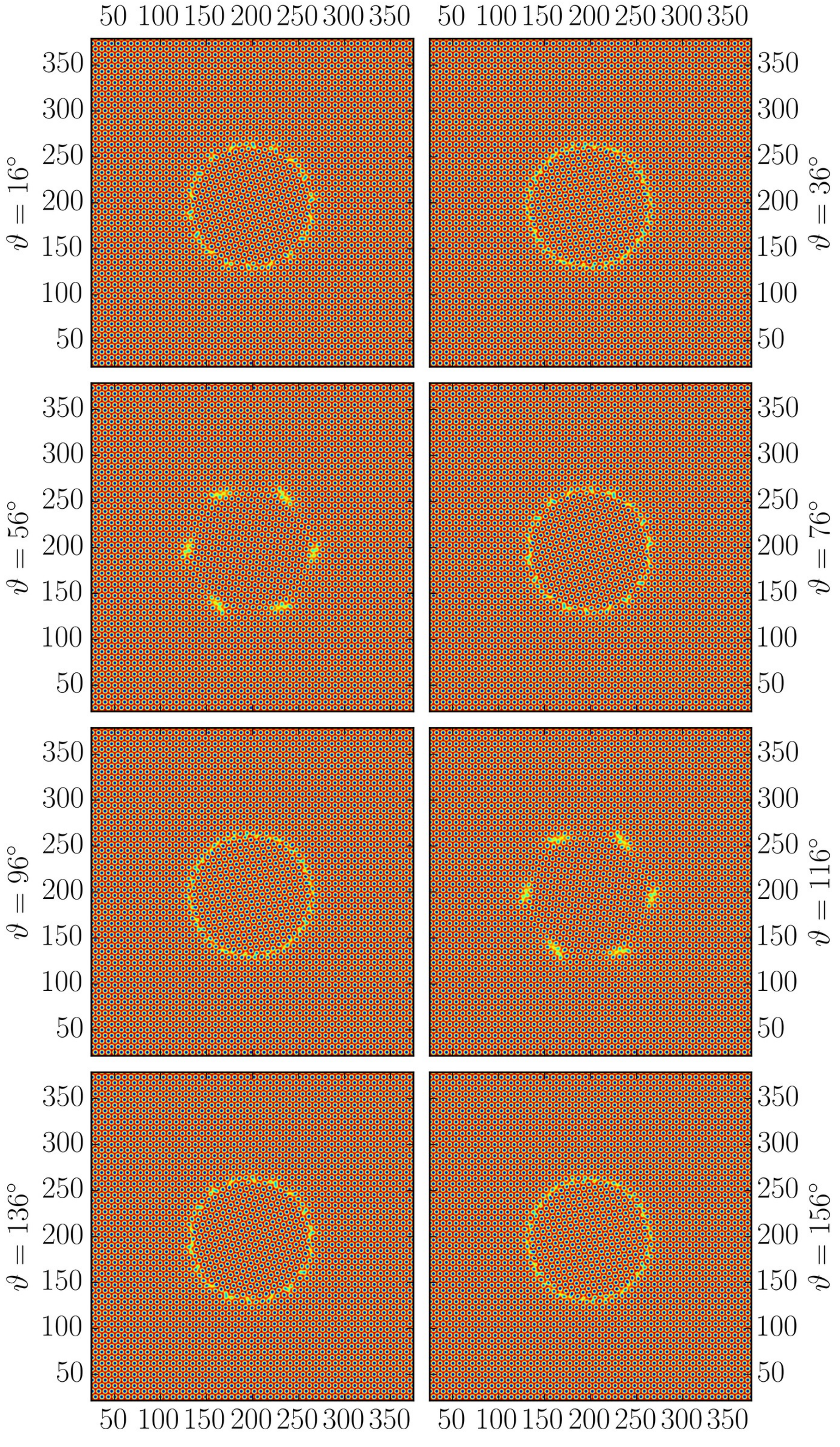

Figure 7.18: Microstructure in the APFC model at selected rotations. Rotating grain with $t_0 = 25000$ and $R_{PFC} = 61.2$.

Chapter 8

Conclusions

In this work we improved the amplitude expansion of the PFC model (APFC) to enable simulations of grains with arbitrary and changing rotations on an adaptive mesh. Our improvements eliminate the problem of beats in the complex amplitudes of APFC models that hinder use of AMR techniques in these models, and eliminate the unphysical grain boundary that occurs between grains rotated by a crystal's symmetry rotation and effectively limits the grain rotations which the APFC models can describe for up to a of the crystal's symmetry rotation.

The improvements are based on introducing an auxiliary field that describes rotation of a local grain in the APFC model. This field is derived from the main phase field variables (A_j) and is never directly used in calculations. The idea of deriving an additional field that is not to be used in the calculations represents a new contribution of this thesis. The utility of such a field may not seem obvious (i.e. why derive an extra field, if not for use in calculations?). However, in cases where the area occupied by the grain boundaries is much larger than the total simulation domain, which is the case when simulating the microstructure's evolution in metallic alloys, the usability of such a field vastly exceeds the costs of its calculation. We successfully used the auxiliary local rotation field to exploit the rotational covariance of the complex amplitude equations in the APFC model and effectively align the basis vectors for the complex amplitudes with the local grain in all calculation points. By doing this, we removed the problem of the beats in complex amplitudes and enabled mesh refinement at all computational points.

As presented in Chapter 3, the results of simulations using the improved algorithm closely match the previous results, and the scaling of the number of computational nodes is similar to that achieved in earlier works [9]. This verifies that our improvements merely exploit the structure of the APFC equations in a way that does not introduce any notable sources of error into the model, while transforming the equations into a form able to be used with AMR techniques in the Cartesian form of the equations.

In our next step, we made a further improvement to the model that removes the unphysical grain boundary from the APFC model, enabling APFC simulations with grains of arbitrary rotations. The APFC model is derived from the PFC model using an expansion of the density function in the form of density waves defined in equation (3.1), repeated here for convenience

$$\psi = \sum_{j=1}^{3} A_j e^{i\mathbf{k_j}\cdot\mathbf{x}} \qquad + \sum_{j=1}^{3} A_j^* e^{-i\mathbf{k_j}\cdot\mathbf{x}} \qquad + \overline{\psi} \tag{8.1}$$

This ansatz expresses the rotation of grains described by the density function ψ in two different ways, by rotation of the base vectors $\mathbf{k}_j$ and by beats in the complex amplitudes described in equation (3.12). Both expressions of the rotation of the local grain are treated separately in the APFC model, and thus when the rotation expressed by the beats approaches the amounts of rotation expressed by the base vectors, which happens at approximately half the symmetry rotation of the modelled crystal structure, standard APFC models are unable to connect both expressions of the rotation and show an unphysical grain boundary [10] in areas where this occurs. Our improvements enable the models to make the connection between both expressions of the grain rotation by use of the local rotation field, which captures the rotation expressed by the beats in the complex amplitudes. The algorithm matches the complex amplitudes in all computational nodes according to the physically correct rotations of the local grain, which removes the unphysical grain boundary as seen in Fig. 3.5.

The removal of the unphysical grain boundary from the APFC models effectively corrects the grain boundary energies in approximately half of the grain boundaries in case where the initial seeds were arbitrarily rotated within the range of one symmetry rotation of the crystal lattice. In case the grain rotation is truly random or the grains can rotate during the simulation, the fraction of grain boundaries with correct energies in the APFC model is $1/2N_{sym}$ where N_{sym} is the order of the rotational symmetry of the crystal lattice ($N_{sym} = 6$ for triangular lattice). This significantly improves the applicability of the APFC models to the modelling of industrially important processes because grain rotation occurs in many of them.

We compared the grain boundary energies obtained with our improved APFC model with previously published results [51] (see Fig. 6.3) and found good agreement between the results for angles less than half the crystal's symmetry rotation. For larger angles, our improvements successfully removed the effects of the unphysical grain boundary and matched the published results for grain boundaries at a shifted angle. The new improvements correctly matched results published previously at small and large rotation angles, with a smooth transition between configurations at an appropriate angle.

In Chapter 7 we verified that the new improvements do not introduce unexpected errors into the APFC model when grains rotate dynamically in the simulation, by modelling a rotating grain in a solidified matrix. We observed the same phenomena in our improved APFC model and in the basic PFC model (Fig. 7.3), corroborating that the newly developed improvements can enable APFC simulations of processes, where grain rotation occurs.

The improvements we developed are based on a local rotation field derived from the complex amplitudes of the APFC model combined with an exploit of the rotational covariance of the dynamic equations of the APFC model. It should be noted that the application of local rotation comes at the price of having to numerically convert the amplitudes between different local rotations in all steps of the calculation. This introduces additional calculations compared to using the basic APFC model. However, as the improvements significantly reduce the number of computational points required, this is a good tradeoff in simulations of samples with a realistic grain boundary to volume ratios. It is also noted that the local rotation can be turned off in parts of the model where it is not needed, which speeds up the calculations in that part of the model. The improvement should be seen as a tool to accelerate simulations: it can be selectively applied to areas/computational nodes where its introduction has a positive effect on the speed of simulations. Most notably, the local rotation could be turned off at the lowest level of mesh refinement where it is not of much use and where most of the computational power is spent. The aim of the local rotation is to enable mesh refinement. Therefore, where the mesh cannot be refined, it might be best to turn it off. This can be easily achieved as its introduction does not change the evolution equations in any way. Another possibility for further speedups in simulations is to discretize the local rotation angles. After the local rotation values are discretized, the conversion of complex amplitudes at different local rotations must be performed in a significantly smaller area than before. As this is the first research based on the new approach, we opted to simplify the algorithms as much as possible and not introduce any of the possible improvements mentioned above, which are listed here mode as reference for any reader interested in further developing this approach.

The improvements presented in this thesis can also be applied to other variants of the APFC model and combined with other improvements made to it. Extending this approach to 3D is straightforward and changing applications to APFC models with a different set of dynamic equations (e.g. an APFC model that includes instantaneous relaxation of elastic deformations [53]) is possible as all models derived from the APFC model should preserve the rotational covariance of the governing equations.

A relatively straightforward application of the improvements would be to study the evolution of the grain orientation distribution function in a process where a sample with larger grains is deformed. The deformation could be imposed on the simulation domain by engineering proper boundary conditions which could match an industrial process such as rolling or forging. The temperature profile could also be varied during such simulations to match the same industrial conditions. It would be interesting to see the atomistic picture and dislocation motion in phenomena observed during material flow and deformation, usually studied only on the level where the material is treated as a continuum.

Bibliography

[1] Raabe, D., "Computational Materials Science: The Simulation of Materials Microstructures and Properties," *Wiley-VCH*, 1998.

[2] Weinan, E., *Principles of Multiscale Modeling.* Cambridge University Press, 2011.

[3] Horstemeyer, M. F., *Integrated Computational Materials Engineering (ICME) for Metals.* TMS, Wiley, 2012.

[4] Provatas, N. and Elder, K., *Phase-Field Methods in Materials Science and Engineering.* John Wiley & Sons, 2010.

[5] Elder, K. R., Katakowski, M., Haataja, M. and Grant, M., "Modeling elasticity in crystal growth," *Phys. Rev. Lett.*, vol. 88, p. 245701, June 2002.

[6] Elder, K. R. and Grant, M., "Modeling elastic and plastic deformations in nonequilibrium processing using phase field crystals," *Phys. Rev. E*, vol. 70, p. 051605, Nov. 2004.

[7] Goldenfeld, N., Athreya, B. P. and Dantzig, J. A., "Renormalization group approach to multiscale simulation of polycrystalline materials using the phase field crystal model," *Phys. Rev. E*, vol. 72, p. 020601, Aug. 2005.

[8] Goldenfeld, N., Athreya, B. P. and Dantzig, J. A., "Renormalization group approach to multiscale modelling in materials science," *J. Stat. Phys.*, vol. 125, pp. 1019–1027, 2006.

[9] Athreya, B. P., Goldenfeld, N., Dantzig, J. A., Greenwood, M. and Provatas, N., "Adaptive mesh computation of polycrystalline pattern formation using a renormalization-group reduction of the phase-field crystal model," *Phys. Rev. E*, vol. 76, p. 056706, Nov. 2007.

[10] Spatschek, R. and Karma, A., "Amplitude equations for polycrystalline materials with interaction between composition and stress," *Phys. Rev. B*, vol. 81, p. 214201, June 2010.

[11] Elder, K. R., Provatas, N., Berry, J., Stefanovic, P. and Grant, M., "Phase-field crystal modeling and classical density functional theory of freezing," *Phys. Rev. B*, vol. 75, p. 064107, Feb. 2007.

[12] Wu, K.-A., Adland, A. and Karma, A., "Phase-field-crystal model for fcc ordering," *Phys. Rev. E*, vol. 81, p. 061601, June 2010.

[13] Wu, K.-A., Plapp, M. and Voorhees, P. W., "Controlling crystal symmetries in phase-field crystal models.," *J. Phys.: Condens. Matter*, vol. 22, no. 36, p. 364102, 2010.

[14] Greenwood, M., Provatas, N. and Rottler, J., "Free Energy Functionals for Efficient Phase Field Crystal Modeling of Structural Phase Transformations," *Phys. Rev. Lett.*, vol. 105, p. 045702, July 2010.

[15] Greenwood, M., Ofori-Opoku, N., Rottler, J. and Provatas, N., "Modeling structural transformations in binary alloys with phase field crystals," *Phys. Rev. B*, vol. 84, p. 064104, Aug. 2011.

[16] Kocher, G. and Provatas, N., "New Density Functional Approach for Solid-Liquid-Vapor Transitions in Pure Materials," *Phys. Rev. Lett.*, vol. 114, p. 155501, Apr. 2015.

[17] Seymour, M. and Provatas, N., "Structural phase field crystal approach for modeling graphene and other two-dimensional structures," *Phys. Rev. B*, vol. 93, no. 3, p. 035447, 2016.

[18] Ofori-Opoku, N., Fallah, V., Greenwood, M., Esmaeili, S. and Provatas, N., "Multicomponent phase-field crystal model for structural transformations in metal alloys," *Phys. Rev. B*, vol. 87, p. 134105, Apr. 2013.

[19] Fallah, V., Ofori-Opoku, N., Stolle, J., Provatas, N. and Esmaeili, S., "Simulation of early-stage clustering in ternary metal alloys using the phase-field crystal method," *Acta Mater.*, vol. 61, no. 10, pp. 3653–3666, 2013.

[20] Stefanovic, P., Haataja, M. and Provatas, N., "Phase-Field Crystals with Elastic Interactions," *Phys. Rev. Lett.*, vol. 96, p. 225504, June 2006.

[21] Prieler, R., Hubert, J., Li, D., Verleye, B., Haberkern, R. and Emmerich, H., "An anisotropic phase-field crystal model for heterogeneous nucleation of ellipsoidal colloids.," *J. Phys.: Condens. Matter*, vol. 21, no. 46, p. 464110, 2009.

[22] Wittkowski, R., Löwen, H. and Brand, H. R., "Derivation of a three-dimensional phase-field-crystal model for liquid crystals from density functional theory," *Phys. Rev. E*, vol. 82, p. 031708, Sept. 2010.

[23] Wittkowski, R., Löwen, H. and Brand, H. R., "Polar liquid crystals in two spatial dimensions: The bridge from microscopic to macroscopic modeling," *Phys. Rev. E*, vol. 83, no. 6, p. 061706, 2011.

[24] Faghihi, N., Provatas, N., Elder, K. R., Grant, M. and Karttunen, M., "Phase-field-crystal model for magnetocrystalline interactions in isotropic ferromagnetic solids," *Phys. Rev. E*, vol. 88, no. 3, p. 032407, 2013.

[25] Seymour, M., Sanches, F., Elder, K. and Provatas, N., "Phase-field crystal approach for modeling the role of microstructure in multiferroic composite materials," *Phys. Rev. B*, vol. 92, no. 18, p. 184109, 2015.

[26] Emmerich, H., Löwen, H., Wittkowski, R., Gruhn, T., Tóth, G. I., Tegze, G. and Gránásy, L., "Phase-field-crystal models for condensed matter dynamics on atomic length and diffusive time scales: An overview," *Adv. Phys.*, vol. 61, no. 6, pp. 665–743, 2012.

[27] Stolle, J. F., *Phase Field Crystal Studies of Strain-Mediated Effects in the Thermodynamics and Kinetics of Interfaces.* PhD thesis, McMaster University, 2014.

[28] Adland, A. J., *Phase-Field Crystal Modeling of Polycrystalline Materials.* PhD thesis, Northeastern University, 2013.

[29] Greenwood, M., *Using Phase-Field Modeling With Adaptive Mesh Refinement To Study Elasto-Plastic Effects In Phase Transformations.* PhD thesis, McMaster University, 2008.

[30] Faghihi, N., *Phase Field Crystal Approach to the Solidification of Ferromagnetic Materials.* PhD thesis, The School of Graduate and Postdoctoral Studies, The University of Western Ontario, 2012. PhD Thesis.

[31] Ofori-Opoku, N., *Phase-Field-Crystal Models for Microstructural Evolution and Phase Selection in Materials Science.* PhD thesis, McMaster University, 2013.

[32] Landau, E. M., L. D. . L., *Statistical Physics 3rd Edition, Part 1.* Pergamon Press, third edition edition ed., 1986.

[33] Ramakrishnan, T. and Yussouff, M., "First-principles order-parameter theory of freezing," *Phys. Rev. B*, vol. 19, no. 5, p. 2775, 1979.

[34] Hohenberg, P. C. and Halperin, B. I., "Theory of dynamic critical phenomena," *Rev. Mod. Phys.*, vol. 49, pp. 435–479, July 1977.

[35] Stefanovic, P., Haataja, M. and Provatas, N., "Phase field crystal study of deformation and plasticity in nanocrystalline materials," *Phys. Rev. E*, vol. 80, Oct. 2009.

[36] Chaikin, P. M. and Lubensky, T. C., *Principles of Condensed Matter Physics*, vol. 1. Cambridge Univ Press, 2000.

[37] Seitz, F., *The Modern Theory of Solids.* McGraw-Hill Book Company, Inc; New York, 1940.

[38] Athreya, B. P., Goldenfeld, N. and Dantzig, J. A., "Renormalization-group theory for the phase-field crystal equation," *Phys. Rev. E*, vol. 74, p. 011601, July 2006.

[39] Adland, A., Karma, A., Spatschek, R., Buta, D. and Asta, M., "Phase-field-crystal study of grain boundary premelting and shearing in bcc iron," *Phys. Rev. B*, vol. 87, Jan. 2013.

[40] Geslin, P.-A., Xu, Y. and Karma, A., "Morphological instability of grain boundaries in two-phase coherent solids," *Phys. Rev. Lett.*, vol. 114, no. 10, p. 105501, 2015.

[41] Xu, Y.-C., Geslin, P.-A. and Karma, A., "Elastically mediated interactions between grain boundaries and precipitates in two-phase coherent solids," *Phys. Rev. B*, vol. 94, no. 14, p. 144106, 2016.

[42] Hüter, C., Neugebauer, J., Boussinot, G., Svendsen, B., Prahl, U. and Spatschek, R., "Modelling of grain boundary dynamics using amplitude equations," *Continuum Mech. Thermodyn.*, pp. 1–17, 2015.

[43] Salvalaglio, M., Backofen, R., Elder, K. R. and Voigt, A., "Defects at grain boundaries: A coarse-grained, three-dimensional description by the amplitude

expansion of the phase-field crystal model," *Phys. Rev. Materials*, vol. 2, p. 053804, May 2018.

[44] Elder, K. R., Rossi, G., Kanerva, P., Sanches, F., Ying, S.-C., Granato, E., Achim, C. V. and Ala-Nissila, T., "Patterning of Heteroepitaxial Overlayers from Nano to Micron Scales," *Phys. Rev. Lett.*, vol. 108, p. 226102, May 2012.

[45] Elder, K. R., Rossi, G., Kanerva, P., Sanches, F., Ying, S.-C., Granato, E., Achim, C. V. and Ala-Nissila, T., "Modeling self-organization of thin strained metallic overlayers from atomic to micron scales," *Phys. Rev. B*, vol. 88, p. 075423, Aug. 2013.

[46] Elder, K. R., Chen, Z., Elder, K., Hirvonen, P., Mkhonta, S., Ying, S.-C., Granato, E., Huang, Z.-F. and Ala-Nissila, T., "Honeycomb and triangular domain wall networks in heteroepitaxial systems," *J. Chem. Phys.*, vol. 144, no. 17, p. 174703, 2016.

[47] Smirman, M., Taha, D., Singh, A. K., Huang, Z.-F. and Elder, K. R., "Influence of misorientation on graphene Moiré patterns," *Phys. Rev. B*, vol. 95, no. 8, p. 085407, 2017.

[48] Ofori-Opoku, N., Stolle, J., Huang, Z.-F. and Provatas, N., "Complex order parameter phase-field models derived from structural phase-field-crystal models," *Phys. Rev. B*, vol. 88, p. 104106, Sept. 2013.

[49] Elder, K. R., Huang, Z.-F. and Provatas, N., "Amplitude expansion of the binary phase-field-crystal model," *Phys. Rev. E*, vol. 81, p. 011602, Jan. 2010.

[50] Huang, Z.-F., Elder, K. R. and Provatas, N., "Phase-field-crystal dynamics for binary systems: Derivation from dynamical density functional theory, amplitude equation formalism, and applications to alloy heterostructures," *Phys. Rev. E*, vol. 82, p. 021605, Aug. 2010.

[51] Hirvonen, P., Ervasti, M. M., Fan, Z., Jalalvand, M., Seymour, M., Vaez Allaei, S. M., Provatas, N., Harju, A., Elder, K. R. and Ala-Nissila, T., "Multiscale modeling of polycrystalline graphene: A comparison of structure and defect energies of realistic samples from phase field crystal models," *Phys. Rev. B*, vol. 94, p. 035414, July 2016.

[52] Elder, K. R. and Huang, Z.-F., "A phase field crystal study of epitaxial island formation on nanomembranes," *J. Phys.: Condens. Matter*, vol. 22, no. 36, p. 364103, 2010.

[53] Heinonen, V., Achim, C. V., Elder, K. R., Buyukdagli, S. and Ala-Nissila, T., "Phase-field-crystal models and mechanical equilibrium," *Phys. Rev. E*, vol. 89, p. 032411, Mar. 2014.

[54] Heinonen, V., Achim, C. V., Kosterlitz, J. M., Ying, S.-C., Lowengrub, J. and Ala-Nissila, T., "Consistent Hydrodynamics for Phase Field Crystals," *Phys. Rev. Lett.*, vol. 116, p. 024303, Jan. 2016.

[55] Salvalaglio, M., Backofen, R., Voigt, A. and Elder, K. R., "Controlling the energy of defects and interfaces in the amplitude expansion of the phase-field crystal model," *Phys. Rev. E*, vol. 96, no. 2, p. 023301, 2017.

[56] Huang, Z.-F. and Elder, K. R., "Morphological instability, evolution, and scaling in strained epitaxial films: An amplitude-equation analysis of the phase-field-crystal model," *Phys. Rev. B*, vol. 81, p. 165421, Apr. 2010.

[57] Yeon, D.-H., Huang, Z.-F., Elder, K. R. and Thornton, K., "Density-amplitude formulation of the phase-field crystal model for two-phase coexistence in two and three dimensions," *Philos. Mag.*, vol. 90, no. 1-4, pp. 237–263, 2010.

[58] Majaniemi, S. and Provatas, N., "Deriving surface-energy anisotropy for phenomenological phase-field models of solidification," *Phys. Rev. E*, vol. 79, p. 011607, Jan. 2009.

[59] Provatas, N. and Majaniemi, S., "Phase-field-crystal calculation of crystal-melt surface tension in binary alloys," *Phys. Rev. E*, vol. 82, p. 041601, Oct. 2010.

[60] Majaniemi, S. and Grant, M., "Dissipative phenomena and acoustic phonons in isothermal crystals: A density-functional theory study," *Phys. Rev. B*, vol. 75, Feb. 2007.

[61] Chan, P. Y. and Goldenfeld, N., "Nonlinear elasticity of the phase-field crystal model from the renormalization group," *Phys. Rev. E*, vol. 80, p. 065105, Dec. 2009.

[62] Berčič, M. and Kugler, G., "Adaptive mesh simulations of polycrystalline materials using a Cartesian representation of an amplitude expansion of the phase-field-crystal model," *Phys. Rev. E*, vol. 98, p. 033303, Sept. 2018.

[63] Steinbach, I., "Phase-field models in materials science," *Modell. Simul. Mater. Sci. Eng.*, vol. 17, no. 7, p. 073001, 2009.

[64] Elder, K. R., Drolet, F., Kosterlitz, J. M. and Grant, M., "Stochastic eutectic growth," *Phys. Rev. Lett.*, vol. 72, pp. 677–680, Jan. 1994.

[65] Drolet, F., Elder, K. R., Grant, M. and Kosterlitz, J. M., "Phase-field modeling of eutectic growth," *Phys. Rev. E*, vol. 61, pp. 6705–6720, June 2000.

[66] Casselman, B., "Yale Babylonian Collection's Tablet YBC 7289, Copyright Bill Casselman and Yale Babylonian Collection, http://www.math.ubc.ca/~cass/Euclid/ybc/ybc.html."

[67] Press, W. H., Teukolsky, S. A., Vetterling, W. T. and Flannery, B. P., *Numerical Recipes 3rd Edition: The Art of Scientific Computing.* Cambridge, UK ; New York: Cambridge University Press, 3 edition ed., Sept. 2007.

[68] Raabe, D., *Computational Materials Science.* Weinheim: Wiley-VCH, June 1998.

[69] Matoŭs, K., Geers, M. G., Kouznetsova, V. G. and Gillman, A., "A review of predictive nonlinear theories for multiscale modeling of heterogeneous materials," *J. Comput. Phys.*, vol. 330, pp. 192–220, 2017.

[70] Provatas, N., Goldenfeld, N. and Dantzig, J., "Efficient Computation of Dendritic Microstructures Using Adaptive Mesh Refinement," *Phys. Rev. Lett.*, vol. 80, pp. 3308–3311, Apr. 1998.

[71] Greenwood, M., Hoyt, J. J. and Provatas, N., "Competition between surface energy and elastic anisotropies in the growth of coherent solid-state dendrites," *Acta Mater.*, vol. 57, no. 9, pp. 2613–2623, 2009.

Razširjeni povzetek v slovenskem jeziku

9.1 Uvod

Sodobna znanost o inženirskih materialih temelji na spoznanju, da so lastnosti materialov do velike mere odvisne od mikrostrukture in niso povsem določene s kemijsko ali fazno sestavo materiala. To še posebej velja za termomehanske lastnosti kovinskih zlitin. Mikrostrukturo lahko opišemo na več skalah [1, 2], ki jih v grobem delimo na kvantnomehansko, atomistično, mezoskopsko, ki ustreza nivoju zrn oziroma podzrn, in makroskopsko, ki je običajno večja ali enaka vzorcem za mehanske preizkuse. Zaradi tako velike dimenzijske raznolikosti posameznih mikrostrukturnih elementov, kompleksnosti vseh možnih interakcij med njimi in različnih časovnih skal, na katerih potekajo procesi, ki določajo kinetiko razvoja mikrostruktur, zahteva njihovo kvantitativno fizikalno napovedovanje uporabo modelov in simulacij. To še posebej velja za primere, ko je raziskovani pojav eksperimentalno težko določljiv. S stališča prakse je uporaba numeričnih pristopov z napovedno močjo zaželena predvsem zaradi zmanjšanja števila večinoma dragih eksperimentov, potrebnih za optimizacijo materialnih lastnosti, in za načrtovanje novih postopkov ter tehnologij. Poseben pomen imajo računalniške simulacije pri razumevanju pojavov, kjer preizkusov v praksi ni mogoče izvesti zaradi varnostnih ali praktičnih razlogov.

Seveda pa imajo tudi računalniške simulacije pri raziskavah inženirskih materialov svoje omejitve, ki največkrat izvirajo predvsem iz časovnih in prostorskih skal procesov, ki jih je mogoče z razpoložljivo računalniško opremo simulirati. Na primer metode, ki niso oprte na nobene eksperimentalne vhodne podatke in jih imenujemo “ab initio” ter temeljijo na kvantni mehaniki, so v današnjem času dimenzijsko izredno omejene. Po drugi strani pa se je omenjenim omejitvam zaradi časovne in prostorske skale delno mogoče izogniti, kadar uspemo teorije in modele na različnih skalah medsebojno sklopiti. Takšen opis imenujemo večnivojski pristop oziroma simulacije na več skalah (ICME) [3], pri tem pa velikokrat ravnamo tako, da za vsako skalo posebej uporabimo najprimernejše modele in metode, ki jih po navadi z raznimi ad-hoc rešitvami sklopimo tako, da izbrane parametre izmenjujemo med skalami, ali pa s simulacijami na nižjih skalah v reprezentativnih volumnih določimo vrednosti spremenljivk, ki jih nato uporabimo na višji skali. Takšno medsebojno "mešanje" različnih modelov je povezano z različnimi težavami in velikokrat vodi do vprašljivih rezultatov. Na atomističnem nivoju je pogosto uporabljana metoda molekularne dinamike, ki pa je numerično zelo zahtevna in zato omejena na spremljanje pojavov preko kratkih časov v majhnih vzorcih simuliranega materiala. Večje vzorce materiala lahko modeliramo s pomočjo klasične teorije gostotnih funkcionalov, pri kateri material že opišemo s poljem. Opis s pomočjo polja uporabimo tudi pri metodi faznega polja kristala (PFC) [5, 6], pri kateri polje predstavlja verjetnostno gostoto atomov na določenem mestu in na kateri temelji ta doktorska naloga. Metoda PFC namreč predstavlja pomemben napredek pri modeliranju materialov na atomskem nivoju. Njena izboljšava, ki temelji na uporabi pristopa renormalizacijske grupe (metoda APFC) [7, 8] omogoča modeliranje in simulacije mnogo večjih volumnov materiala in prehod z atomistične skale na mezoskopsko preko povezave z zelo razširjenimi metodami faznega polja [4], ki omogočajo simulacije razvoja mikrostruktur na mezoskopski prostorski skali. Metoda APFC izrazi atomsko gostoto kot vsoto valov z določenimi kompleksnimi amplitudami. Te kompleksne amplitude se s krajem spreminjajo veliko počasneje kot atomska gostota, saj predstavljajo amplitudo hitro nihajoče funkcije atomske gostote, in so kot take že veliko bolj primerne za uporabo v kombinaciji s tehnikami prilagodljivega zgoščevanja mreže računskih točk (AMR). Učinkovito uporabo tehnik AMR v APFC modelih omejuje pojav utripanja kompleksnih amplitud v zrnih, ki so rotirana glede na izbrane osnovne vektorje, uporabljene pri razvoju gostote. Poleg utripanja kompleksnih amplitud pa je v modelih APFC problematičen tudi pojav nefizikalne meje med zrni, ki so medsebojno rotirana za simetrijsko rotacijo kristala. Ta meja onemogoča APFC simulacije pojavov, pri katerih zrna kristalov lahko rotirajo ali pa je nesmotrno omejevati rotacije zrn na določen interval.

Ta doktorska disertacija prinaša nove načine za odpravo ovir pri efektivni uporabi modelov APFC za modeliranje industrijsko pomembnih procesov za preoblikovanje materiala. V poglavju 5 predstavimo razvito rešitev za odpravo utripanja v modelih APFC z uvedbo polja lokalne rotacije, preko katerega omogočimo prostorsko odvisno rotacijo osnovnih vektorjev za razvoj atomske gostote, v poglavju 6 nadgradimo uporabo polja lokalne rotacije z izboljšavo, ki odpravi nefizikalno mejo med zrni, v poglavju 7 pa predstavimo simulacije rotirajočih zrn z izboljšanim modelom APFC. Celotne izboljšave modelov APFC, razvite v sklopu te doktorske disertacije omogočijo APFC simulacije procesov, pri katerih zrna lahko rotirajo, na mrežah s prilagodljivo gostoto računskih točk. To odpre nove možnosti za raziskave razvoja mikrostrukture v industrijsko pomembnih procesih.

9.2 Uvod v model faznega polja kristala

Model faznega polja kristala temelji na minimizaciji proste energije funkcionala, ki je oblikovan tako, da so njegove rešitve periodične funkcije s simetrijo kristalne mreže [5, 6]. Kot tak naravno vsebuje mnogo pojavov, povezanih s kristali: elastičnost v kristalni fazi, topološke defekte v kristalni mreži, rast kristalnih zrn, energijo meje med zrni in fazne transformacije med trdno in tekočo fazo. Zasnovan je bil na podobnosti kristalnih sistemov z drugimi periodičnimi sistemi, a ga lahko izpeljemo tudi iz klasične teorije gostotnih funkcionalov (CDFT) pod nekaj predpostavkami [11]. Za razliko od modelov, temelječih na CDFT model PFC operira s časovno in krajevno povprečenim poljem gostote atomov, zato lahko doseže večje volumne in simulacijske čase. Zaradi navedenih lastnosti je model PFC zelo primeren za preučevanje pojavov, pomembnih za razumevanje razvoja mikrostrukture kovinskih materialov, saj lahko z njim modeliramo mikrostrukturo dovolj velikih volumnov za preučevanje interakcije med mejami zrn in defekti.

Začetna oblika modela PFC je lahko stabilizirala samo eno kristalno strukturo [5], čeprav je lahko prikazala tudi druge, metastabilne kristalne strukture in stabilizirala progasto fazo. Osnovna oblika funkcionala PFC stabilizira kristalne oblike, za opis katerih je dovolj le en vrh v dvodelčni korelacijski funkciji. Z dodajanjem novih načinov za stabilizacijo več vrhov dvodelčnih korelacijskih funkcij se lahko stabilizira faze, v katerih je za opis kristalne simetrije pomembnih več vrhov teh funkcij [12, 13]. Strukturni model PFC (XPFC) [14, 15] je bil razvit z namenom enostavnejše stabilizacije faz s kompleksno simetrijo in deluje na modeliranju v Fourierovem prostoru, kjer je dvodelčna korelacijska funkcija predstavljena kot vsota Gaussovih vrhov pri valovnih vektorjih, ki ustrezajo valovnim vektorjem faz, ki jih želimo stabilizirati. Še boljše možnosti stabilizacije faz s kompleksnimi simetrijami prinaša vključevanje trodelčnih korelacijskih funkcij v model PFC [16, 17]. Osnovni model PFC [5], ki je vključeval le binarno zmes, so tudi razširili [18, 19] na ternarne zmesi.

Model PFC je bil prav tako razširjen, da vključuje tudi pojave, ki jih osnovni model PFC ni najbolje opisal, na primer hitre elastične deformacije [20], prostorsko anizotropijo [21], tekoče kristale [22, 23], feromagnetične in feroelektrične pojave [24, 25]. Za poglobljen opis možnih razširitev modela PFC priporočamo pregledni članek [26], za detajlne opise določenih razširitev pa disertacije [27–31].

9.2.1 Landauova teorija faznih prehodov

Landauova teorija faznih prehodov temelji na predpostavki, da je prosta energija sistema zvezna funkcija parametra urejenosti

$$f(\Omega, T) = a_2\Omega^2 + a_3\Omega^3 + a_4\Omega^4 \tag{9.2}$$

kjer je Ω parameter urejanja, T pa temperatura. Za simulacijo faznih prehodov mora biti koeficient a_2 odvisen od temperature kot $a_2 = \frac{T-T_c}{T_c}\tilde{a}_2$, kjer je $\tilde{a}_2$ pozitivna konstanta. Fazni prehodi drugega reda so zvezni v parametru urejanja, prehodi prvega reda pa predstavljajo prehode med fazami z neničelno latentno toploto. Prikazani so na sliki 9.1.

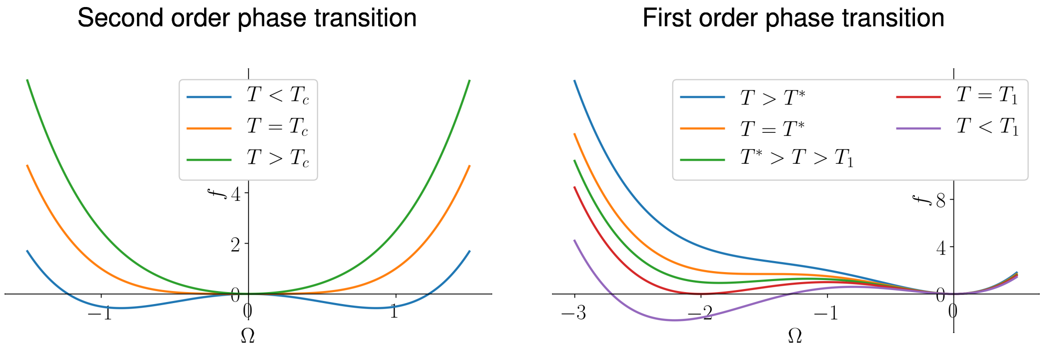

Slika 9.1: Proste energije v Landauovi teoriji faznih prehodov. V zveznem faznem prehodu prvega reda se parameter urejanja Ω zvezno spremeni pri prehodu skozi kritično temperaturo T_c. V faznih prehodih drugega reda pa se pri prehodu skozi temperaturo faznega prehoda T_1 parameter urejanja spremeni nezvezno, in pri tej temperaturi globalni minimum proste energije nezvezno preskoči na neničelno vrednost Ω.

Landauova teorija faznih prehodov je osnova za modele faznega polja (PF), in v modelu PFC nastopa kot del funkcionala proste energije, ki opiše prehod med fazami.

9.2.2 PFC-model čistega materiala

Prosta energija čistega materiala je podana z enačbo

$$\Delta\mathcal{F} = \Delta\mathcal{F}_{id} + \Delta\mathcal{F}_{ex} + \Delta\mathcal{F}_{ext} \tag{9.3}$$

kjer je $\Delta\mathcal{F}$ prosta energija celotnega sistema, $\Delta\mathcal{F}_{id}$ je prosta energija sistema, ki izvira iz termodinamskih odvistnosti, $\Delta\mathcal{F}_{ex}$ je prosta energija, ki izvira iz interakcije med delci, in $\Delta\mathcal{F}_{ext}$ je prosta energija zaradi zunanjih polj. Če prosto energijo sistema izrazimo z atomsko gostoto, dobimo

$$\Delta\mathcal{F}_{id}/k_BT = \int d\mathbf{r}\,[\rho\ln(\rho/\rho_0) - \delta\rho] \tag{9.4}$$

kjer je k_B Boltzmanova konstanta, T temperatura $\rho = \rho(\mathbf{r})$, $\delta\rho = \rho - \rho_0$ in ρ_0 povprečna atomska gostota [11, 33]. Prosta energija, ki izvira iz atomskih interakcij, pa je po teoriji CDFT

$$\Delta\mathcal{F}_{ex}/k_BT = \int d\mathbf{r}\left[-\sum_{n=2}^{\infty}\frac{1}{n!}\int_{i=1}^{n} d\mathbf{r}_i\delta\rho(\mathbf{r}_i)C_n(\mathbf{r}_1, \mathbf{r}_2, \ldots, \mathbf{r}_n)\right] \tag{9.5}$$

kjer je C_n n-delčna korelacijska funkcija izotropne tekočine [11]. Prispevek k prosti energiji zaradi zunanjih polj je

$$\Delta\mathcal{F}_{ext} = \int d\mathbf{r}M(\mathbf{r})\frac{\delta F}{\delta M} \tag{9.6}$$

kjer je M zunanje polje (npr. magnetno polje) [4]. V tem delu ne obravnavamo vpliva zunanjih polj, zato ta prispevek k prosti energiji vedno zanemarimo ($\Delta\mathcal{F}_{ext} = 0$).

Uvedemo brezdimenzijsko atomsko gostoto kot $\psi = (\rho - \rho_0)/\rho_0$. Da izpeljemo model PFC, razvijemo idealno prosto energijo do ψ^4

$$\Delta\mathcal{F}_{id}/k_BT\rho_0 = \int d\mathbf{r}\left[\frac{\Delta B}{2}\psi^2 - \frac{t}{3}\psi^3 + \frac{v}{4}\psi^4\right] \tag{9.7}$$

kjer so $\Delta B = 1$, $t = 1/2$ in $v = 1/3$ parametri, kot jih dobimo iz teorije CDFT, v praksi pa jih uporabimo kot proste parametre za prilagajanje faznega diagrama materialu, ki ga želimo modelirati.

Prispevek k prosti energiji zaradi meddelčnih interakcij v modelu PFC razvijemo v vrsto do dvodelčnih interakcij (nekatere razširitve modela PFC vsebujejo trodelčne interakcije). Dvodelčno korelacijsko funkcijo v Fourierovem prostoru aproksimiramo s polinomom četrte stopnje $\hat{C}_2(k) = \hat{C}_{20} + \hat{C}_{22}k^2 + \hat{C}_{24}k^4$, kjer so sode potence prepovedane zaradi simetrije. Za to so v modelu vrhovi gostotne funkcije bolj razmazani kot v modelih CDFT. Končna oblika tega prispevka k prosti energiji je tako

$$\Delta\mathcal{F}_{ex}/k_BT\rho_0 = \int d\mathbf{r} \left[B_X \frac{\psi}{2}(1 + 2\nabla^2 + \nabla^4)\psi \right] \tag{9.8}$$

kjer so konstante $\hat{C}_{20}$,$\hat{C}_{22}$ in $\hat{C}_{24}$ izbrane tako, da jih lahko izrazimo z le eno konstanto.

Končna oblika PFC funkcionala proste energije je tako

$$\Delta\mathcal{F}/k_BT\rho_0 = F = \int d\mathbf{r} \left[\frac{B_L}{2}\psi^2 - \frac{t}{3}\psi^3 + \frac{v}{4}\psi^4 + B_X \frac{\psi}{2}(2\nabla^2 + \nabla^4)\psi \right] \tag{9.9}$$

$$= \int d\mathbf{r} \left[\frac{\Delta B}{2}\psi^2 - \frac{t}{3}\psi^3 + \frac{v}{4}\psi^4 + B_X \frac{\psi}{2}(1 + \nabla^2)^2\psi \right] \tag{9.10}$$

kjer je $B_L = \Delta B + B_X$. B_L in B_X sta izotermični stisljivosti tekoče in trdne faze. Prvotni model PFC je bil izpeljan preko podobnosti s Swift-Hohenbergovim modelom in ni vseboval kubičnega člena. Neničelno vrednost tega člena utemeljimo preko izpeljave iz teorije CDFT , v praksi pa ta čelen uporabimo za izbiro ravnovesne atomske gostote sistema.

Dinamične enačbe za model PFC izpeljemo preko disipativne dinamike modela B [4, 26]

$$\frac{\partial\psi}{\partial t} = \Gamma\nabla^2 \left(\frac{\delta F}{\delta\psi} \right) + \eta = \Gamma\nabla^2 \left(B_L\psi - t\psi^2 + v\psi^3 + B_X(2\nabla^2 + \nabla^4)\psi \right) + \eta \tag{9.11}$$

kjer je Γ konstanta običajno enaka 1, in η stohastičen šum $\langle \eta(\boldsymbol{r}, t)\eta(\boldsymbol{r'}, t') \rangle = -\Gamma k_BT\nabla^2\delta(\boldsymbol{r} - \boldsymbol{r'})\delta(t - t')$, v tem delu nastavljen na 0 v simulacijah.

9.3 Amplitudni model faznega polja kristala

Amplitudni model faznega polja kristala (APFC) je izboljšava modela PFC s pomočjo razvoja funkcije atomske gostote v vsoto valov s kompleksnimi amplitudami, usmerjenimi v smereh izbranih vektorjev recipročne mreže kristalne faze. Slika 9.2 prikazuje razmerje med kompleksnimi amplitudami in atomsko gostoto. Model APFC je prvi

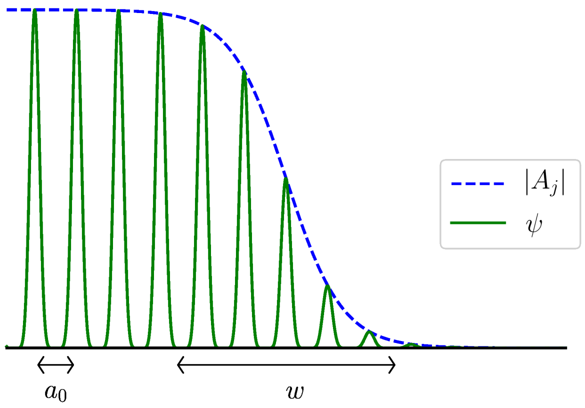

Slika 9.2: Kompleksne amplitude A_j predstavljajo amplitudo ovojnice funkcije gostote atomov ψ. Medtem ko se funkcija gostote ψ, na razdaljah manjših od valovne dolžine a_0, spreminja hitro, se kompleksne amplitude A_j znatno spremenijo šele na dolžinah, primerljivih z debelino meje w.

razvil Goldenfeld s sodelavci [7, 8] preko izpeljave s pomočjo teorije renormalizacijske grupe. Poglavitna prednost modela APFC je računanje s pomočjo amplitud, ki se spreminjajo veliko počasneje, kot se spreminja atomska gosta, in so zato primerne za uporabo v kombinaciji s tehnikami adaptivnega zgoščanja mreže računskih točk (AMR) [9]. Vsota kvadratov vseh kompleksnih amplitud predstavlja agregatno stanje materiala in tako model APFC povezuje model PFC s klasičnimi modeli faznega polja. Obstajajo različne izpeljave modela APFC, tu bomo na kratko predstavili izpeljavo s pomočjo volumskega povprečenja in ogrobljevanja [48, 58, 59].

Za izpeljavo APFC modela materiala, ki kristalizira s trikotno simetrijo, uporabimo nastavek

$$\begin{aligned}\psi &= \sum_{j=1}^{3} A_j e^{i\mathbf{k_j}\cdot\mathbf{x}} && + \sum_{j=1}^{3} A_j^* e^{-i\mathbf{k_j}\cdot\mathbf{x}} && +\overline{\psi} \\ &= \sum_{j=1}^{3} A_j e^{i\mathbf{k_j}\cdot\mathbf{x}} && +CC && +\overline{\psi} \qquad (9.12)\end{aligned}$$

kjer CC pomeni kompleksno konjugirano vrednost predhodnega izraza, $A_j = A_j(\mathbf{r})$ so kompleksne amplitude, $\mathbf{k}_j$ so osnovni vektorji recipročne mreže, podani v enačbi (9.13)

$$\mathbf{k}_1 = k_0(-\boldsymbol{i}\sqrt{3}/2 - \boldsymbol{j}/2), \qquad \mathbf{k}_2 = k_0\boldsymbol{j}, \qquad \mathbf{k}_3 = k_0(\boldsymbol{i}\sqrt{3}/2 - \boldsymbol{j}/2) \tag{9.13}$$

s $k_0 = 1$ in $\overline{\psi} = \overline{\psi}(\mathbf{r})$ je prostorsko odvisna povprečna gostota atomov. V izpeljavi s pomočjo povprečenja naredimo konvolucijo členov v izrazu za prosto energijo PFC z normirano izglajevalno funkcijo ξ [18, 48, 60]

$$\langle f(\mathbf{r})\rangle_V = \int_{-\infty}^{+\infty} d\mathbf{r} f(\mathbf{r}')\xi_V(\mathbf{r}-\mathbf{r}') \tag{9.14}$$

kjer je $f(\mathbf{r}')$ funkcija, ki jo izglajujemo, in $\langle f(\mathbf{r})\rangle$ izglajena funkcija. Najenostavnejši je izbor izglajevalne funkcije, ki je konstantna znotraj enotske celice kristala in nič zunaj nje. Da izpeljemo izglajen funkcional proste energije, izražen s kompleksnimi amplitudami A_j, vstavimo nastavek (9.12) v prosto energijo modela PFC (9.10) in zamenjamo vrstni red integracije ter upoštevamo, da se vsi členi, ki nihajo z neničelnim koeficientom, v eksponentni funkciji izničijo [48, 52]

$$\begin{aligned} F = \quad & \int d\mathbf{r}\left[\frac{\overline{\psi}^2}{2} - t\frac{\overline{\psi}^3}{6} + v\frac{\overline{\psi}^4}{12} + (1 - t\overline{\psi} + v\overline{\psi}^2)\left(\sum_{j=1}^{3}|A_j|^2\right)\right. \\ & -(t-2v\overline{\psi})[A_1A_2A_3 + A_1^*A_2^*A_3^*] + \frac{v}{2}\left[\sum_{j=1}^{3}|A_j|^4\right] \\ & \left. +2v\left[\sum_{j=1}^{3}\sum_{m>j}^{3}|A_j|^2|A_m|^2\right] + B_X\sum_{j=1}^{3}|(\nabla^2 + 2i\mathbf{k}_j\nabla)A_j|\right] \end{aligned} \tag{9.15}$$

ter izpeljemo dinamične enačbe modela APFC preko modela C [49]

$$\frac{\partial\overline{\psi}}{\partial t} = \nabla^2\frac{\delta F}{\delta\overline{\psi}} \tag{9.16}$$

$$\frac{\partial A_j}{\partial t} = -\frac{\delta F}{\delta A_j^*} \tag{9.17}$$

9.4 Numerične metode

Numerično reševanje matematičnih problemov je poznano že tisočletja. Numeričnega reševanja, ki lahko da le približen rezultat, se lotimo, ko ne poznamo analitičnih rešitev določenega problema. Pri fizikalnih problemih je pogosto res, da analitične rešitve diferencialnih enačb niso poznane. To drži tudi za diferencialne enačbe, izpeljane iz modelov PFC in APFC, zato v simulacijah operiramo z numeričnimi približki rešitev.

Za namene numeričnega reševanja diferencialnih enačb moramo čas in prostor diskretizirati. To lahko naredimo le, če je rešitev, ki jo iščemo, zvezna. Numerično odvod funkcije aproksimiramo preko razvoja funkcije rešitve f v Taylorjevo vrsto okrog točke x:

$$\begin{aligned} f(x+h) &= f(x) + f'(x)h + h^2(\dots) \\ &\Downarrow \text{(razvoj do } h^2\text{)} \\ f'(x) &= \frac{f(x+h)-f(x)}{h} \\ &\Downarrow \text{(diskretiziramo na regularni mreži, } x = nh, f(nh) = f_n\text{)} \\ f'_n &= \frac{f_{n+1}-f_n}{h} \end{aligned} \tag{9.18}$$

V tem delu smo zaradi enostavnosti implementacije vedno uporabljali le približke prvega reda, lahko pa obdržimo več členov v Taylorjevi vrsti in je približek bolj točen a za ceno dodatnega računanja.

Prostor običajno diskretiziramo z delitvijo na enakomerno mrežo točk. Bolj učinkovito je računanje na mreži, kjer se gostota računskih točk lahko prilagaja spreminjanju rešitve (AMR). Glavni namen tehnik adaptivnega zgoščevanja računskih točk je koncentracija računske moči na območja simulirane domene, kjer se rešitve spreminjajo hitreje, saj se tako poveča hitrost računanja brez znatne izgube natančnosti rešitev. Primer adaptivne mreže je prikazan na sliki 9.3. Med računskimi elementi ("Compute node"), v katerih rešujemo diferencialno enačbo z numerično shemo, so elementi mreže ("Ghost node"), v katerih vrednosti izračunamo s povprečenjem vrednosti v sosednjih računskih elementih. Število vmesnih elementov, ki jih potrebujemo, je odvisno od reda približka za numeričen izračun odvodov. V tem delu zato vedno uporabljamo le približke prvega reda.

9.5 Adaptivno zgoščevanje mreže v modelu APFC

V tem poglavju bomo predstavili izboljšave k metodi APFC, ki omogočajo aplikacijo algoritmov AMR v kombinaciji s kartezično reprezentacijo amplitudnih enačb. Predstavljena rešitev omogoči adaptivno zgoščevanje mreže računskih točk v vseh zrnih,

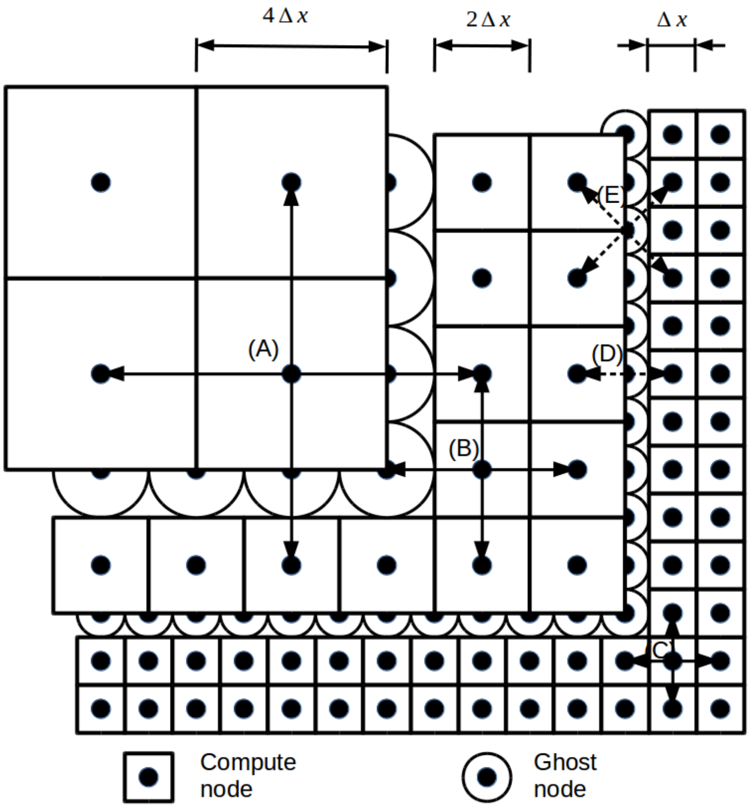

Slika 9.3: Adaptivna mreža računskih točk. Puščice povezujejo računske elemente mreže, potrebne za izračun odvodov s približkom prvega reda v centralni točki povezav. Med elementi mreže, v katerih rešitev enačb računamo z diferencialno enačbo ("Compute node"), so elementi mreže, v katerih se vrednosti izračunajo s povprečenjem sosednjih elementov mreže ("Ghost node"), ki omogočajo povezovanje numerične rešitve preko več nivojev gostote mrežnih točk.

kar pomembno pohitri simulacije. Rotacija zrn kristala je v modelu APFC izražena z utripanjem kompleksnih amplitud, ki onemogoči učinkovito uporabo algoritmov AMR. Obstoječe rešitve [9] so zato namesto s kartezično predstavitvijo kompleksnih amplitud operirale s fazo/amplitudo posebej, kar je zahtevalo dodatne približke, prineslo nove težave v model in zakompliciralo uporabo enačb. V praksi se je za reševanje enačb modela APFC še vedno uporabljala neadaptivna mreža točk. Slika 9.4 prikazuje pojav utripanja kompleksnih amplitud v rotiranih zrnih skupaj s prikazom osnovnih vektorjev kompleksnih amplitud A_j.

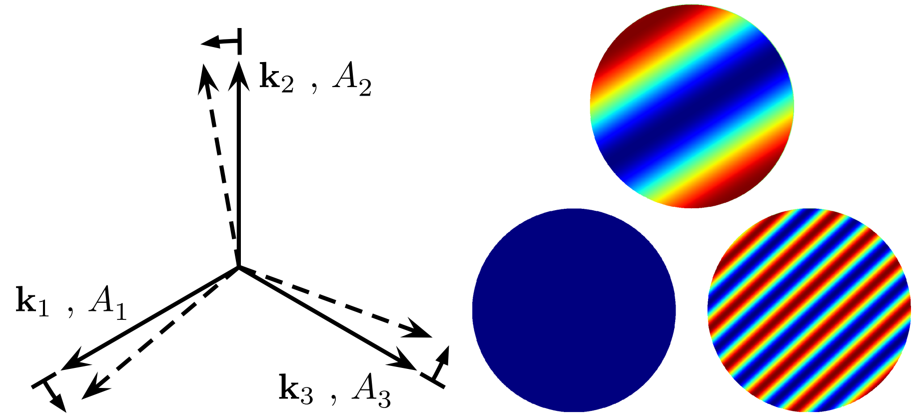

Slika 9.4: Osnovni vektorji za kompleksne amplitude A_j in njihova rotacija. V modelu APFC je rotacija zrn izražena z utripanjem kompleksnih amplitud, kar je prikazano na desni sliki. Slike prikazujejo $\Re(A_1)$ v zrnih, ki so rotirana za $\theta = 0°$, $5°$ in $25°$ (v smeri urinega kazalca od leve spodaj).

9.5.1 Lokalna rotacija kompleksnih amplitud

Naša izboljšava odstrani utripanje kompleksnih amplitud z uvedbo polja lokalne rotacije, ki omogoči lokalno odvisnost rotacije osnovnih vektorjev. Osnovne vektorje za kompleksne amplitude tako lahko v vseh točkah računa efektivno poravnamo z lokalnim zrnom, kar odstrani utripanje. Lokalno rotirane kompleksne amplitude uvedemo kot

$$A_j = A_j^{\vartheta} e^{i\delta\mathbf{k}_j(\vartheta)\cdot\mathbf{x}} \tag{9.19}$$

kjer so $\mathbf{k}_j(\vartheta) = \mathbf{k}_j + \delta\mathbf{k}_j(\vartheta)$ rotirani osnovni vektorji za amplitude. Ker so v popolnoma strjenem, rotiranem zrnu amplitude konstantne, velja, da je gradient kompleksnih amplitud nič.

$$\nabla A_j^{\vartheta} = (\nabla A_j)e^{-i\delta\mathbf{k}_j\cdot\mathbf{x}} + A_j(-i\delta\mathbf{k}_j)e^{-i\delta\mathbf{k}_j\cdot\mathbf{x}} = 0 \tag{9.20}$$

Iz (9.20) sledi, da mora za lokalno rotacijo, pri kateri utripanje izgine, veljati

$$\delta\mathbf{k}_j(\vartheta) = \frac{\nabla A_j}{iA_j} = \mathbf{k}_j(\vartheta) - \mathbf{k}_j \tag{9.21}$$

V simulacijah poznamo kompleksne amplitude in lahko iz enačbe (9.21) izračunamo idealno lokalno rotacijo.

Numerično rešujemo diferencialno enačbo za kompleksne amplitude

$$\frac{\partial A_j}{\partial t} = \tilde{\mathcal{L}}_j A_j - 3A_j|A_j|^2 - 6A_j \sum_{k:k\neq j} |A_k|^2 - 6\overline{\psi} \prod_{k:k\neq j} A_k^* \tag{9.22}$$

kjer so $k, j \in [1,3]$ osnovni vektorji in

$$\tilde{\mathcal{L}}_j = (1 - \nabla^2 - 2i\mathbf{k}_j \cdot \nabla)(-r - 3\overline{\psi}^2 - \{\nabla^2 + 2i\mathbf{k}_j \cdot \nabla\}^2) \tag{9.23}$$

rotacijsko kovarianten operator. Parametri $\overline{\psi}$ in r predstavljajo brezdimenzijsko povprečno gostoto atomov in brezdimenzijsko temperaturo, ki je sorazmerna z razliko temperature do kritične temperature T_c. Zaradi rotacijske kovariantnosti operatorja $\tilde{\mathcal{L}}_j$ se lahko vse orientacije zrn simulirajo v istem modelu (in rotacija se izrazi z utripanjem kompleksnih amplitud). Rotacijska kovariantnost operatorja $\tilde{\mathcal{L}}_j$ in osnovnega sestavnega dela tega operatorja $\square^\vartheta = (\nabla^2 + 2i\mathbf{k}_j(\vartheta) \cdot \nabla)$ pomeni, da lahko rotacijo in krajevne spremembe v rotaciji izrazimo neodvisno od glavnega izračuna, in sicer da velja

$$\square^\vartheta A_j^\vartheta = e^{-i\delta\mathbf{k}\cdot\mathbf{x}} \square A_j \tag{9.24}$$

kjer je $\square = \square^{\vartheta=0}$.

Numerično lahko operator $\tilde{\mathcal{O}}^\vartheta$ apliciramo na lokalno rotirano polje X

$$\tilde{\mathcal{O}}^{\vartheta(\mathbf{x})}\ X^{\vartheta(\mathbf{x})}(\mathbf{x}) = \sum_{\tilde{\mathbf{x}}} \Gamma_{\tilde{\mathbf{x}}} e^{-i(\mathbf{k}(\mathbf{x}) - \mathbf{k}(\tilde{\mathbf{x}}))\cdot\tilde{\mathbf{x}}} X^{\vartheta(\tilde{\mathbf{x}})}(\tilde{\mathbf{x}}) \tag{9.25}$$

kjer gre sumacija preko vseh sosedov, ki jih vključuje operatorjevo jedro. $\tilde{\mathcal{O}}$ je lahko katerikoli izmed rotacijsko kovariantnih operatorjev ($\tilde{\mathcal{O}} \in \{\tilde{\mathcal{L}}_j^\vartheta, \tilde{\mathcal{L}}_{1j}^\vartheta, \tilde{\mathcal{L}}_{2j}^\vartheta\}$), apliciran na katerokoli izmed izpeljanih polj ($X \in \{A_j^\vartheta, \tilde{\mathcal{L}}_{1j} A_j^\vartheta, \tilde{\mathcal{L}}_j A_j^\vartheta\}$). $\tilde{\mathbf{x}}$ je krajevni vektor soseda, ki se ujema z elementom jedra operatorja $\Gamma_{\tilde{\mathbf{x}}}$. Da lahko pretvorimo polja med izrazi z lokalnimi rotacijami pri $\mathbf{x}$ in $\tilde{\mathbf{x}}$, moramo množiti $X^{\vartheta(\tilde{\mathbf{x}})}(\tilde{\mathbf{x}})$ z rotacijskim faktorjem $e^{-i(\mathbf{k}(\mathbf{x}) - \mathbf{k}(\tilde{\mathbf{x}}))\cdot\tilde{\mathbf{x}}}$, ki ga shranimo v računske elemente skupaj z vrednostmi $X^{\vartheta(\mathbf{x})}(\mathbf{x})$.

9.5.2 Algoritem za izračune z lokalno rotacijo polj

Pri numeričnem reševanju diferencialne enačbe za kompleksne amplitude v sistemu, kjer je rotacija osnovnih vektorjev krajevno odvisna, moramo pri izračunu upoštevati te razlike v rotacijah. Ker so vsa polja, s katerimi operiramo, rotacijsko kovariantna, lahko rotacijo izoliramo iz računa.

Algoritem, opisan v 4 in 5, deluje na enak način, kot če bi vse sosednje računske elemente začasno pretvoril v sistem, ki je enako rotiran kot centralni računski element. Ko so vse rotacije enake, lahko apliciramo običajne evolucijske enačbe za kompleksne amplitude.

Algoritem 4 Algoritem za evolucijo kompleksnih amplitud.

```
loop
    if $step$ mod $adaptation = 0$ then
        Prilagodi računsko mrežo
        Izračunaj lokalno rotacijo
        Izračunaj faktorje za pretvorbo med lokalnimi rotacijami
    end if
    Izračunaj korak evolucijske enačbe kompleksnih amplitud
end loop
```

Slika 9.5 prikazuje računanje z uporabo algoritmov AMR s prejšnjimi metodami in našim, izboljšanim algoritmom. Naša rešitev omogoča zgostitev adaptivne mreže v vseh točkah računanja z uporabo kartezične reprezentacije amplitudnih enačb, ne glede na orientacijo zrn.

Efektivna uporaba mreže AMR omogoči rast števila računskih točk, sorazmerno z mejo med zrni, kjer se dogajajo pomembne spremembe, in ne več z volumnom simuliranega področja. Slika 9.6 prikazuje odvisnost števila računskih točk od časa v računu. Število najprej narašča, saj se z rastjo zrn povečuje velikost meje med zrni. Ko pa se večina simulacijskega volumna strdi, se število računskih točk ustali na mnogo manjši vrednosti, kot je število računskih točk na enakomerni mreži.

9.6 Popravek nefizikalne meje med zrni v modelu APFC

Poleg težav z uporabo algoritmov AMR ima model APFC težave tudi s pojavom nefizikalne meje med zrni, ki so medsebojno rotirana za simetrijsko rotacijo kristalne mreže [10]. Pojav izvira iz dvojne predstavitve rotiranosti zrn v modelu APFC. Po eni strani rotacijo izražajo smeri osnovnih vektorjev, po drugi pa lahko rotacijo izrazimo tudi preko utripanja kompleksnih amplitud. Kadar se rotacija, izražena na en način, preveč približa rotaciji, izraženi na drug način, pride do nefizikalnih pojavov v modelu. Če se na primer eno zrno zasuče za 60° v primerjavi s sosednjim zrnom, bi bilo smiselno v

Algoritem 5 Izračun lokalne rotacije. Parametri p, q, $A_{minamp.}$ and $\vartheta_{max.phase}$ so hevristično določeni.

```
for vsak računski element do
    Izračunaj optimalno rotacijo $\vartheta_{\mathrm{opt}}$:
    if $|A_j^{\vartheta}| > A_{\mathrm{min\ amp.}}$ then
        V trdnini: iz gradientov
        for all $j \in \{1, 2, 3\}$ do
            $\delta\mathbf{k}_j(\vartheta_{\mathrm{current}}) = \Re(\frac{\nabla A_j^{\vartheta_{\mathrm{current}}}}{iA_j^{\vartheta_{\mathrm{current}}}})$
            $\vartheta_{x,j} = 1 + \mathbf{k}_j(\vartheta_{\mathrm{current}}) \cdot \delta\mathbf{k}_j$
            $\vartheta_{y,j} = (\mathbf{k}_j(\vartheta_{\mathrm{current}}) \times \delta\mathbf{k}_j) \cdot \hat{\mathbf{e}}_z$
        end for
        $\vartheta_{\mathrm{opt}} = \vartheta_{\mathrm{current}} + atan2(\sum_j \vartheta_{y,j}/3, \sum_j \vartheta_{x,j}/3)$
    else
        V kapljevini: konvergiraj k nič
        $\vartheta_{\mathrm{opt}} = 0$
    end if
    Izgladi spremembe
    $\vartheta_{\mathrm{new}} = p \times \vartheta_{\mathrm{current}} + q \times \vartheta_{\mathrm{opt}}$
    Prepreči preskakovanje utripov
    $d\vartheta = \max_{\{\mathrm{vsi\ sosedje\ NN}\}} |\vartheta_{NN} - \vartheta_{\mathrm{new}}|$ modulo $2\pi$
    $k_{\vartheta} = dx\ d\vartheta/\vartheta_{\mathrm{max.\ phase}}$
    if $k_{\vartheta} > 1$ then
        $\vartheta_{\mathrm{new}} = \vartheta_{\mathrm{current}} + (\vartheta_{\mathrm{new}} - \vartheta_{\mathrm{current}})/k_{\vartheta}$
    end if
    $\vartheta_{\mathrm{current}} = \vartheta_{\mathrm{new}}$
end for
```

enačbah povezati kompleksni amplitudi, ki kažeta v fizikalno najbolj enaki smeri (npr. A_1 in A_3^*), kot to prikazuje slika 9.7. To možnost modelu APFC prinese uvedba lokalne rotacije, saj lahko s pomočjo lokalne rotacije najdemo najbolj ustrezajoče si pare kompleksnih amplitud in s tem odstranimo pojav nefizikalne meje med zrni iz modela.

Primer nefizikalne meje med zrni je prikazan na sliki 9.8, ki prikazuje mejo med sosednjima zrnoma pod kotom 50.1°. Naša izboljšava modela APFC je uspešno odstranila nefizikalni pojav in v izboljšanem modelu zraste meja z lastnostmi meje pod kotom 10°, kar je fizikalno pravilno v kristalu s simetrijsko rotacijo 60°.

Z izboljšanim modelom smo izračunali proste energije mej med zrni z različnimi razlikami v rotacijah in jih primerjali z objavljenimi rezultati. Naša izboljšava se dobro ujema s prejšnjimi rezultati, v območju, kjer prejšnji rezultati prikazujejo nefizikalne efekte, pa naša rešitev prikaže pravilno prosto energijo meje med zrni, kot je to prikazano

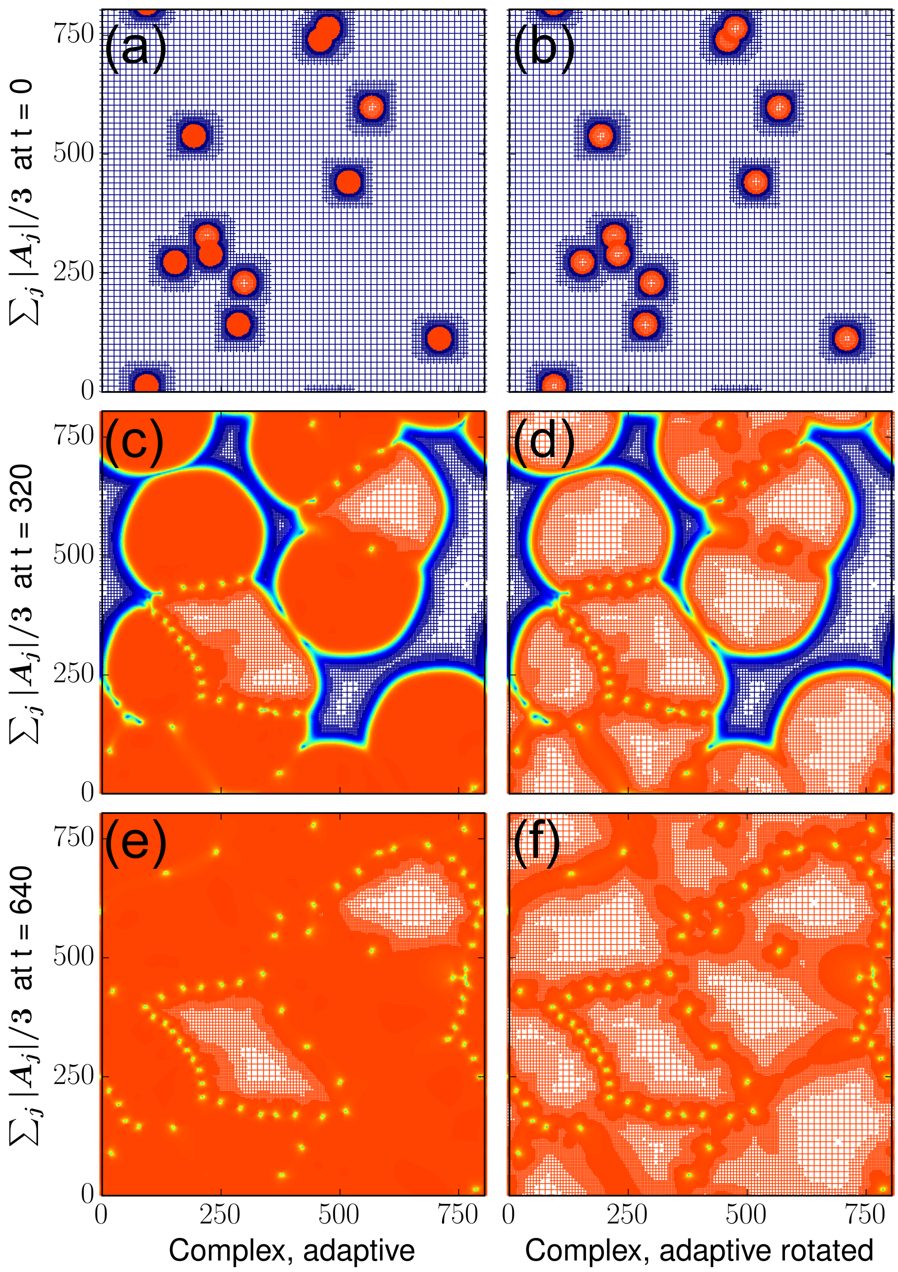

Slika 9.5: Razvoj mikrostrukture s časom. Primerjava modela AMR z ali brez lokalne rotacije. Ko uporabimo lokalno rotacijo se mreža zgosti v vseh zrnih, ne glede na njihovo rotacijo, in ostane gosta le na mejah zrn in v okolici dislokacij, kjer se amplitude hitro spreminjajo. Slike prikazujejo povprečno amplitudo ($\sum_j |A_j|/3$) ob različnih časih.

na sliki 9.9.

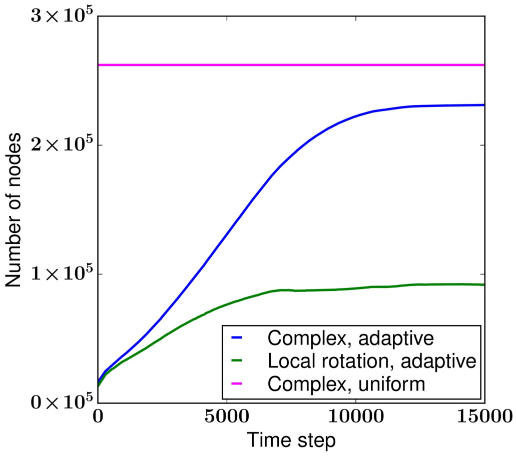

Slika 9.6: Število računskih točk v odvisnosti od časa za simulacijo na sliki 9.5. Po tem, ko kapljevina zamrzne, se število računskih točk neha povečevati. Izboljšan algoritem omogoča znatno manjše število računskih točk, kot bi jih potrebovali v primeru računanja na enakomerni mreži računskih točk.

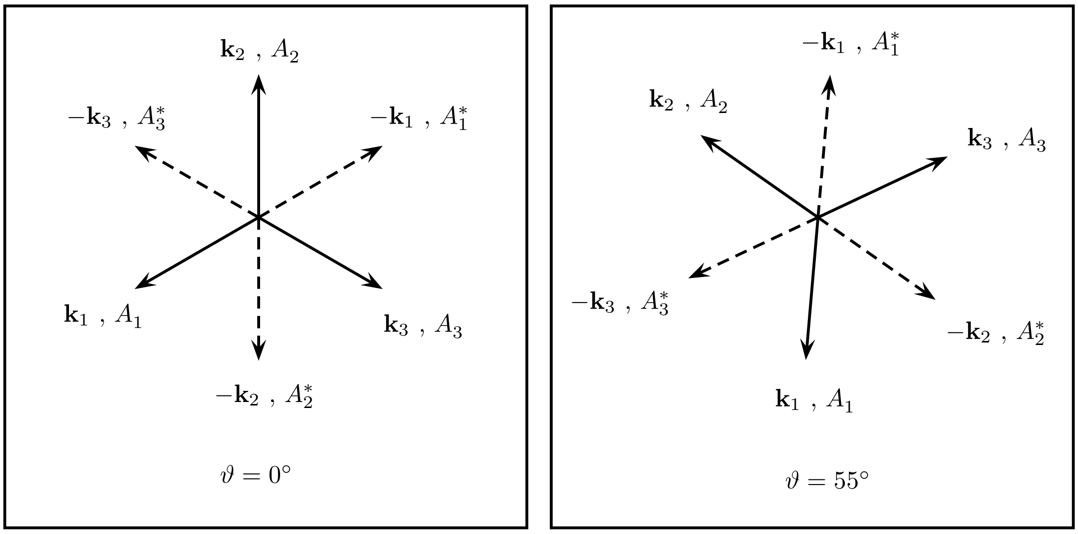

Slika 9.7: Valovni vektorji v sosednjih računskih elementih z različnimi lokalnimi rotacijami (levo: $\vartheta = 0°$, desno: $\vartheta = 55°$). Naš algoritem s pomočjo lokalne rotacije najde ustrezne pare amplitud in pri računanju v enem računskem elementu upošteva ustrezne sosednje kompleksne amplitude. A_2 v levem računskem elementu je tako uporabljena v kombinaciji z A_1^* iz desnega računskega elementa, saj je kot med ustreznima valovnima vektorjema le 5°.

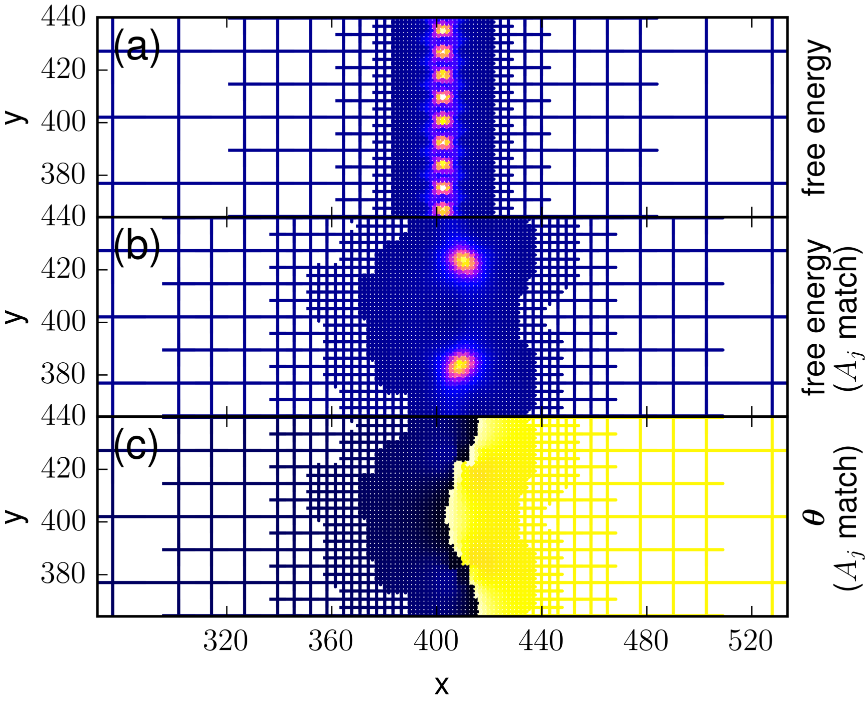

Slika 9.8: Prosta energija na meji med zrnoma pod kotom 50.1°. Prva vrstica (a) prikazuje nefizikalno mejo med zrni v modelu APFC [10]. Druga vrstica (b) prikazuje rezultat z izboljšanim modelom, v katerem zraste meja s karakteristikami 10° meje. Spodnja vrstica (c) prikazuje lokalno rotacijo v simulaciji z izboljšanim modelom.

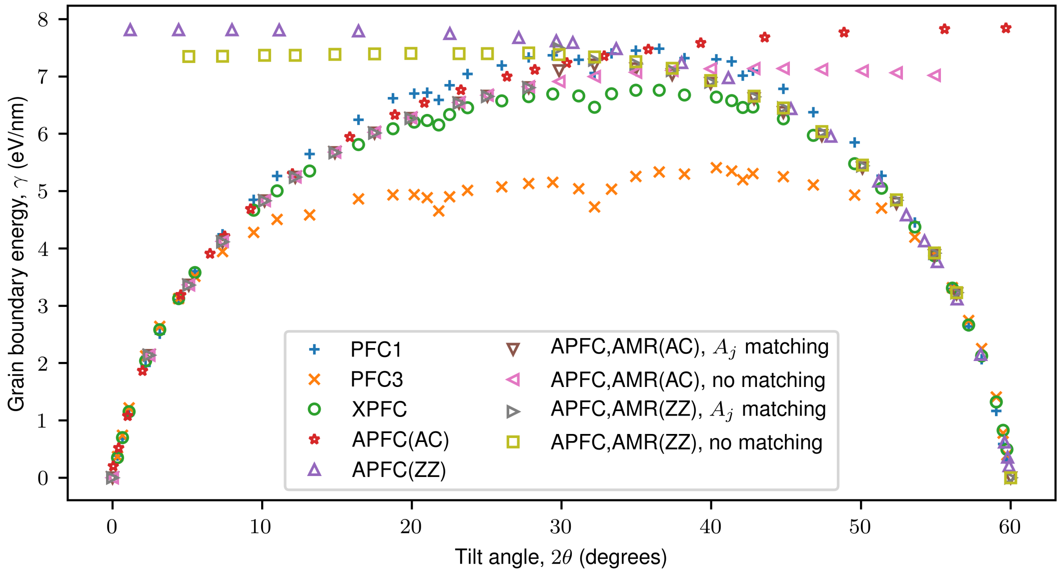

Slika 9.9: Prosta energija meje med zrni kot funkcija kota med zrni. Vrednosti za modele PFC1, PFC3, XPFC, APFC(AC) in APFC(ZZ) je objavil Hirvonen s sodelavci [51]. Naš model se dobro ujema s preteklimi rezultati in z algoritmom ujemanja amplitud uspešno odstrani nefizikalne efekte iz modela APFC.

9.7 Rotirajoče zrno v modelu APFC

Izboljšave, opisane v poglavjih 9.5 in 9.6, nadgradijo model APFC z možnostjo efektivne uporabe algoritmov AMR in odstranijo nefizikalno mejo med zrni, ki je doslej onemogočala simulacije zrn v polnem obsegu rotacij. Obe izboljšavi predstavljata pomembna koraka k možnosti modeliranja industrijsko pomembnih procesov, pri katerih pride do rotacije zrn z modelom APFC Da bi preverili delovanje naših izboljšav v primeru, pri katerem zares pride do dinamičnega spreminjanja rotacije zrn, smo simulirali razvoj mikrostrukture okrog enega okroglega zrna v sredini matrike, ki mu prisilno spreminjamo rotacijo z različnimi hitrostmi. Simulacije smo opravili z modeli APFC in PFC, in kvalitativno primerjali opažene pojave. Znotraj variacije, ki jo prinašajo razlike med modeli PFC in APFC, so opaženi pojavi primerljivi, zato menimo, da naše izboljšave prinašajo v model APFC tudi možnosti simulacije pojavov, pri katerih zrna dinamično rotirajo.

Najprej smo naredili simulacije statičnih rotiranih zrn. Rotirano zrno smo postavili v matriko, stopili manjše območje v matriki okrog zrna in simulirali razvoj mikrostrukture dokler se je ta znatno spreminjala. V obeh modelih med simulacijami notranjosti jedra

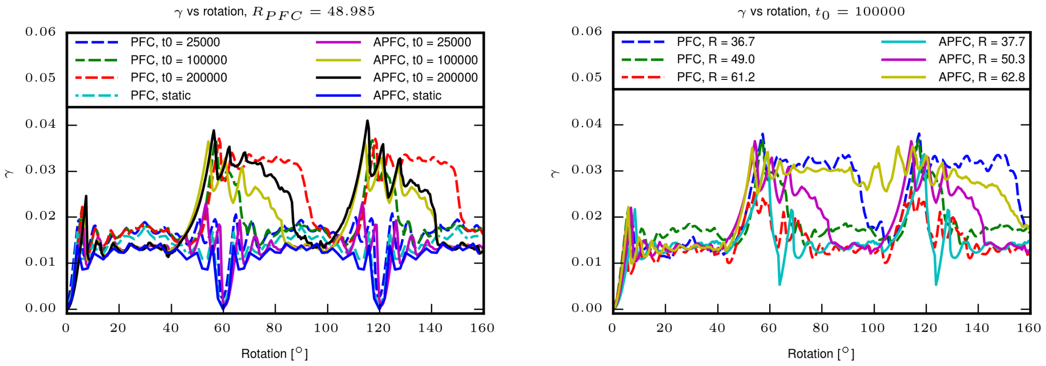

Slika 9.10: Prosta energija meje okrog rotirajočega, okroglega zrna. Spominski efekt v materialu poviša prosto energijo meje pri drugem obratu zrna ($[60°, 120°]$) v primerjavi z istim zrnom pri prvi rotaciji ($[0°, 60°]$). Efekt se poveča s povečevanjem rotacijskega časa zrn (t_0) v obeh modelih. Rezultati statičnih simulacij so periodično ponovljeni čez celotno območje rotacij.

nismo spreminjali, in rob jedra je tako efektivno predstavljal robni pogoj. V notranjosti jedra je bila v obeh modelih nastavljena rešitev v približku razvoja po valovih do prvega reda. Ker v modelu PFC pravilna rešitev odstopa od takšne rešitve, je to eden izmed virov razlik med modeloma, ki jih ne moremo odstraniti. V simulacijah dinamično rotiranih zrn smo nerotirana zrna postavili v matriko, počakali, da se rešitev ni več spreminjala, in šele potem začeli notranjost zrna rotirati v rednih korakih. Rotacija je potekala z nastavljanjem notranjosti območja zrna na rešitev numerične gostote atomov ali pa kompleksnih amplitud, ki je ustrezala rotiranemu zrnu.

9.8 Zaključki

V tem delu smo izboljšali model APFC z izboljšavami, ki omogočajo simulacije z zrni v celotnem območju rotacij in lahko med simulacijo rotacije tudi spreminjajo. Izboljšava omogoča izvajanje takšnih simulacij na adaptivni mreži. Naše izboljšave odstranijo problem utripanja kompleksnih amplitud v rotiranih zrnih, ki preprečuje efektivno uporabo tehnik AMR v modelih APFC in iz modelov APFC odstranijo pojav nefizikalne meje med zrni, ki so rotirana za simetrijsko rotacijo kristala v primerjavi z izbranimi osnovnimi vektorji za razvoj kompleksnih amplitud.

Izboljšave temeljijo na polju lokalne rotacije, ki ga izpeljemo iz kompleksnih amplitud. To polje v simulacijah uporabimo, da lokalno poravnamo osnovne vektorje za

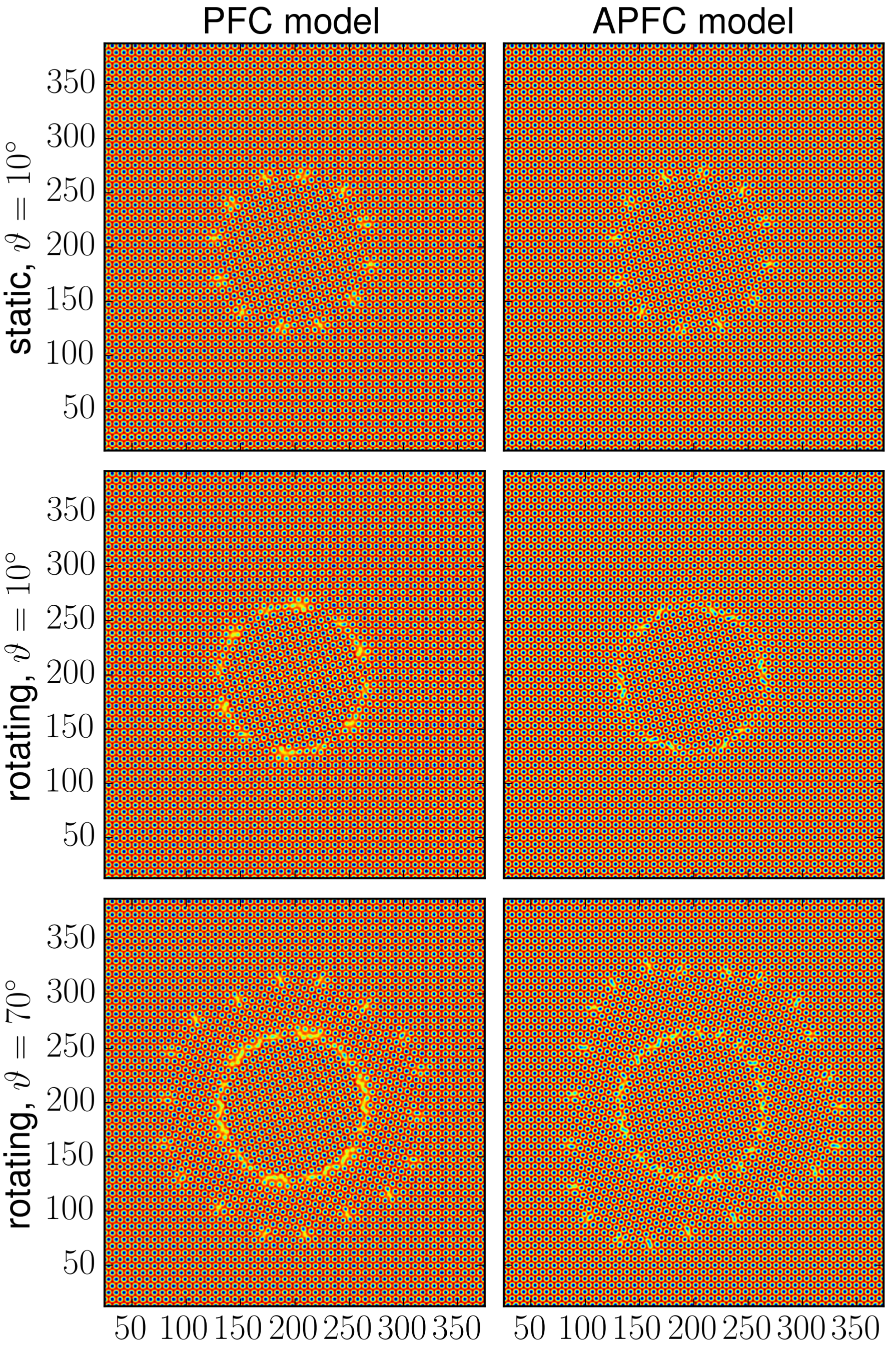

Slika 9.11: Slike prikazujejo mikrostrukturo v okolici rotiranega krožnega zrna v modelih PFC (levi stolpec) in APFC (desni stolpec). Prva vrstica prikazuje mikrostrukturo okrog statičnega zrna, rotiranega za 10°. Druga vrstica prikazuje mikrostrukturo iz simulacije z dinamično rotirajočim zrnom (perioda rotacije je $t_0 = 200000$) v trenutku ko je rotacija zrna 10°. Tretja vrstica prikazuje mikrostrukturo istih zrn v trenutku ko je rotacija zrna $70° = 10° + 60°$. Ker je razlika v rotacijah zrn na spodnjih dveh slikah ravno rotacijska simetrija kristala, je razlika med mikrostrukturami nastala zaradi spomina materiala.

razvoj kompleksnih amplitud z rotacijo lokalnega zrna. V kombinaciji z izkoriščanjem rotacijske kovariantnosti amplitudnih enačb lahko med samim računom pretvarjamo med kompleksnimi amplitudami pri različno rotiranih osnovnih vektorjih. Tako lahko eliminiramo utripanje kompleksnih amplitud v modelih in omogočimo zgoščevanje računske mreže (AMR) v vseh zrnih. Polje lokalne rotacije uporabimo tudi pri določanju kompleksnih amplitud, ki ustrezajo osnovnim vektorjem, ki fizikalno kažejo v najbolj podobnih smereh. Ko v različnih točkah računanja v enačbah povežemo pravilne kompleksne amplitude, eliminiramo tudi problem nefizikalne meje med zrni, ki so zarotirana za simetrijo kristala z ozirom na začetni izbor osnovnih vektorjev za razvoj kompleksnih amplitud.

S predstavljenimi izboljšavami omogočimo APFC simulacije industrijsko pomembnih procesov, pri katerih prihaja do rotacije zrn, z uporabo adaptivne mreže računskih točk (AMR), kar omogoča simulacije z atomsko resolucijo v dovolj velikih domenah, da lahko preučujemo interakcijo med zrni in mejami zrn, ki je pomemben dejavnik pri oblikovanju mikrostrukture materiala.